University of Pardubice

Faculty of Chemical Technology

Chalcogenide thin films

Tomáš Halenkovič

Thesis

2019

UNIVERSITE MATIERE BRETAGNE MOLECULES LOIRE ET MATERIAUX

UNIVERSITÉ DE RENNES 1

THESE DE DOCTORAT DE

L'UNIVERSITE DE RENNES 1
COMUE UNIVERSITE BRETAGNE LOIRE

ECOLE DOCTORALE N° 596
Matière Molécules et Matériaux
Spécialité: Sciences des Matériaux

Thèse présentée et soutenue à Pardubice, le 20. 2. 2019

Unité de recherche: **Department of Graphic Arts and Photophysics, Faculty of Chemical Technology, University of Pardubice, Pardubice, Czech Republic**

Institut des Sciences Chimiques de Rennes, UMR-CNRS 6226, Equipe Verre et Céramiques, Université de Rennes 1, Rennes, France

Rapporteurs avant soutenance:

Ladislav Tichý	University professor
Zdeňka Kolská	Associate professor
Václav Švorčík	University professor

Composition du Jury:

Libor Čapek	University professor – UPa / chairman of the jury
Petr Slepička	Associate professor – VŠCHT / jury member
Josef Havel	University professor – MU / jury member
Directeur de thèse	
Petr Němec	University professor
Co-directrice de thèse	
Virginie Nazabal	Director of research

To my parents

Statement

I declare that I prepared this thesis on my own. All the references are listed in the end of each chapter. I'm familiar with the fact that rights and obligations arising from the Act No. 121/2000 Coll., Copyright Act, apply to my thesis, especially with the fact that the University of Pardubice has the right to make a license agreement for the use of this thesis as a school work according § 60, Section 1 of the Copyright Act and the fact that in the case of using this work by me or another entity, the University of Pardubice is authorized to claim the reasonable expenses from me which were spent on the thesis. According the circumstances these expenses may be claimed up to its actual amount. I am aware that the thesis will be accessible by the public in the library of University of Pardubice and via the Digital Library of the University of Pardubice in agreement with the article 47b of the Act No. 111/1998 Coll., on Higher Education Institutions and on the Amendment and Supplement to some other Acts (the Higher Education Act), as subsequently amended and with the directive no. 9/2012 of University Pardubice.

Acknowledgment

I would like to express my gratitude to my supervisors Associate professor Virginie Nazabal and professor Petr Němec who have had a great impact on both my professional and personal development. I found their supportive and sometimes strict approach to be very valuable and inspirational. I'm also thankful to all the staff members of Department of Graphic Arts and Photophysics and the Group of glass and Ceramics. Also, I would like to express my thanks to many friends I made during my studies both in France and Czech Republic.

I'm grateful to my *Alma mater* University of Pardubice and Campus France for the financial support of student mobility during my PhD studies.

Last but not least I'm grateful to my beloved girlfriend Monika for being supportive and patient with me.

Annotation

This thesis is focused on study of amorphous thin films of ternary Ge-Sb-Se and Ga-Sb-Se systems fabricated by co-sputtering technique for their potential applications in the field of nonlinear optics. General quality by means of morphology and topography, linear and non-linear optical properties and local structure of fabricated films depending on the composition are discussed. The limitation of these materials may lie in their photosensitivity under the near-bandgap light irradiation. Therefore, this aspect of co-sputtered thin films was also studied. In the frame of the thesis, optical properties and structure of quaternary Ge-Sb-Se-Te thin films fabricated by RF sputtering as a potential alternative to ternary systems were also studied.

Key words: amorphous chalcogenides, sputtering, amorphous thin films, optical properties, structure

Anotace

Práce se zabývá studiem tenkých amorfních vrstev ternárních systémů Ge-Sb-Se a Ga-Sb-Se připravených technikou magnetronového naprašování za simultánního použití několika terčů, pro jejich potenciální aplikace v nelineární optice. Je diskutována obecná kvalita ve smyslu morfologie a topografie, lineární a nelineární optické vlastnosti a struktura připravených vrstev v závislosti na složení. Omezení těchto materiálů může spočívat v jejich citlivosti na světlo blízké energii jejich optické šířce zakázaného pásu energií. Byl proto studován i tento aspekt. V rámci práce byly také studovány optické vlastnosti a struktura kvaternárních tenkých vrstev Ge-Sb-Se-Te připravených magnetronovým naprašováním.

Klíčová slova: amorfní chalkogenidy, naprašování, amorfní tenké vrstvy, optické vlastnosti, struktura

Table of contents

Chapter I

Theoretical part

Introduction

Chalcogenide glasses and amorphous thin films are non-crystalline materials based on the elements of chalcogens (*i.e.* S, Se and Te) accompanied with other elements such as Ga, Ge, As, In, Sb *etc.* [1]. These materials have been widely studied since the 1950s [2].

In the form of bulks, they have often restricted use due to their limiting thermal and mechanical properties [3]. The limiting mechanical properties of chalcogenides relative to the rather strong oxide glasses came from the difference in the atomic bonding. Oxide glasses have strong covalent and ionic bonds forming the three-dimensional network, while chalcogenides have weak covalent bonds between two-fold coordinated chalcogen atoms forming a back-bone chain with cross-linking provided by 3- or 4-fold coordinated group 14 and group 15 atoms. The chains are interconnected by weak Van der Waals forces [3]. Therefore, in terms of atomic structure, chalcogenide glasses may be characterized as being between oxide glasses having the three-dimensional networks and organic polymers possessing one-dimensional chain structures [4, 5]. However, the good sharping ability of chalcogenide glasses enables its use in the form of fibres or thin films[6].

Chalcogenide glasses and amorphous thin films possess large number of unique properties, which make them incomparably interesting in many different fields.

First, due to the low phonon energies, they have the broad transmission window from visible to infrared (IR) [7]. The useful range of IR transmission of impurity-free chalcogenide glasses is ~0.6–11.5 μm for sulphides; ~1–15 μm for selenides and ~2–20 μm for tellurides [8]. Thus, chalcogenide glasses found their application in the field of optical sensors and IR fibre-optic devices [9, 10]. The example of transmission spectra of different glasses is shown in fig. 1-1.

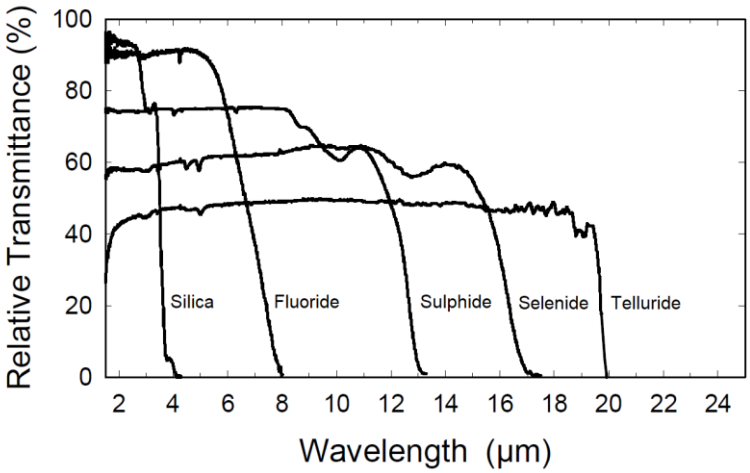

Fig. 1-1 Transmission spectra of different glasses (thickness of about 2-3 mm) – from Sanghera *et al.* [11].

Moreover, low phonon energy of chalcogenides makes them suitable hosts for rare earth (RE) elements due to the low probability of multiphoton relaxation between RE^{3+} energy levels. The typical RE dopants are Pr^{3+}, Dy^{3+} or Tm^{3+} in near-infrared spectral range and Pr^{3+}, Dy^{3+}, Er^{3+}, Ho^{3+} or Tm^{3+} in the middle IR domain [12]. Potential applications of RE doped chalcogenide glasses include fabrication of fibre amplifiers for telecommunication and fibre lasers [13]. Linear optical properties are discussed in *Subchapter 1*.

Furthermore, the advances in the signal processing such as all-optical switching operating typically on the picosecond time scales, requires materials with the high optical nonlinearities [14]. Non-crystalline chalcogenides exhibit third order nonlinearities ($\chi^{(3)}$) between two to three orders of magnitude greater than that of silica [15]. Various types of optical nonlinearities are

discussed in the *Subchapter 2*. Despite being true for chalcogenide glasses and amorphous thin films, subchapters aimed on optical properties (both linear and nonlinear) are valid for most of the amorphous materials.

Perhaps the most striking property of non-crystalline chalcogenides is their photosensitivity, which includes numerous phenomena caused by the electromagnetic radiation [16]. *Subchapter 4* of this section is dedicated to these phenomena.

Aim of thesis

The aim of this thesis is to prepare selenium based amorphous thin films from ternary Ge-Sb-Se and Ga-Sb-Se systems using radio-frequency (RF) magnetron co-sputtering technique. General quality of co-sputtered films is assessed by means of atomic force microscopy and scanning electron microscopy.

Furthermore, optical properties determined from variable angle spectroscopic ellipsometry and spectrophotometry depending on the composition of fabricated films measured by energy-dispersive X-ray spectroscopy is studied. Local structure of thin films is investigated by Raman spectroscopy.

Influence of near-bandgap light irradiation on the optical properties represented by optical bandgap energy and refractive index is also discussed.

Moreover, optical properties and structure is studied also in quaternary Ge-Sb-Se-Te thin films fabricated by RF sputtering.

1. Linear optical properties of amorphous chalcogenides

1.1. Optical absorption and absorption edge

In crystalline intrinsic semiconductors $E_g^{opt} = E_g^e$, where E_g^{opt} and E_g^e are optically and electrically determined (from optical absorption edge and from temperature dependence of the electrical conductivity) bandgap energies. Pioneering studies on amorphous semiconductors have revealed that $E_g^{opt} < E_g^e$ for these materials. As seen on fig. 1-2, the density of states (DOS) smoothly reduces around the band edges and exponentially decay into the energy 'gap' [17, 18].

On the other hand, the mobility edge is assumed to steeply drop to zero. Mobility edge represents the boundary between localized states and extended states (*i.e.* energy separating localized and non-localized states in the conduction or valence bands). The broadening of the mobility edge is considered to be generated by inelastic collisions between electrons and phonons. However, it is sharp at zero temperature[19].

As already indicated, states at band edges are called tail states or gap states [20, 21]. It seems logical, that E_g^{opt} is governed by DOS and the E_g^e is equal to the gap between the mobility edges, thus $E_g^e \approx E_\mu$, where E_μ stands for mobility gap, representing the lowest transition energy between extended valence- and conduction-band states [17, 21].

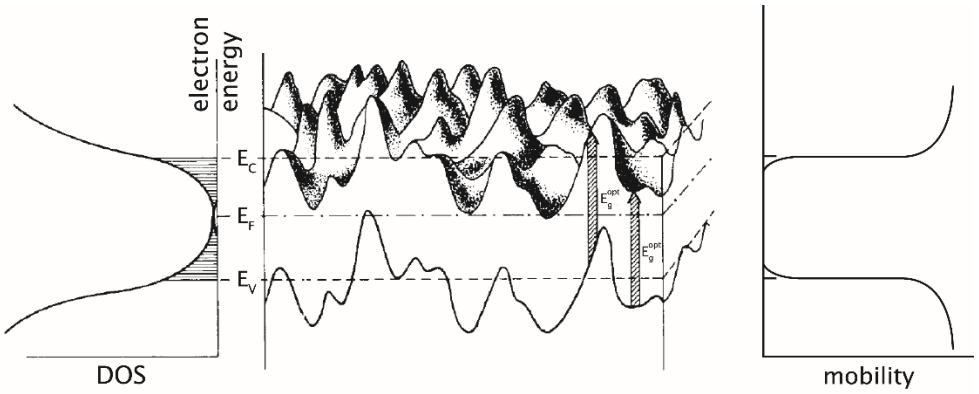

Fig. 1-2 Spatial fluctuations of the band edges (center), DOS (left) and the mobility as a function of electron energy in amorphous semiconductor –from references [17, 22].

Although the number of states in the tails is much smaller than that of extended states, band tails play a very important role in transport and recombination of non-equilibrium charge carriers [20]. Measuring the absorption spectrum is perhaps one of the most direct and simplest methods for probing the band structure of semiconductors. In the absorption process, a photon of a known energy excites an electron from a lower- to a higher-energy state. One can discover all the possible transitions an electron can make and explore much about the distribution of the states, by studying the changes in the transmitted radiation [23].

Absorption is expressed by coefficient α ($\hbar\omega$) which is defined as the relative rate of decrease in light intensity L ($\hbar\omega$) along its path of propagation [23]:

$$\alpha = \frac{1}{\mathrm{L}(\hbar\omega)} \frac{d\,[L(\hbar\omega)]}{dx}$$

Eq. 1-1

In crystalline semiconductors, electronic transitions between the valence and conduction band start at the absorption edge which corresponds to the minimum energy difference E_g between the lowest minimum of the conduction band and the highest maximum of the valence band [23]. The presence of sharp band edges in crystals results in a sharp increase in the absorption coefficient when the energy of photons exceeds the optical bandgap (E_g^{opt}). In amorphous materials, the presence of energy band tails results in significant absorption even at photon energies below the optical gap. Absorption below the edge is described by so-called Urbach rule:

$$\alpha = \alpha_0 \exp\left[\frac{-\gamma\,(E_g - \hbar\omega)}{kT}\right]$$

Eq. 1-2

where α_0 is the absorption coefficient at the bandgap energy E_g and γ is a material constant (slope of the Urbach edge). T is absolute temperature down to a critical value T_0 and equals T_0 for lower temperatures [20].

Absorption edge is usually illustrated as the energy dependence of absorption coefficient. In many amorphous semiconductors the absorption edge has the shape shown in fig. 1-3. One can distinguish the high absorption region A ($\alpha \gtrsim 10^4$), exponential part B (Urbach edge) and the weak absorption tail C [24].

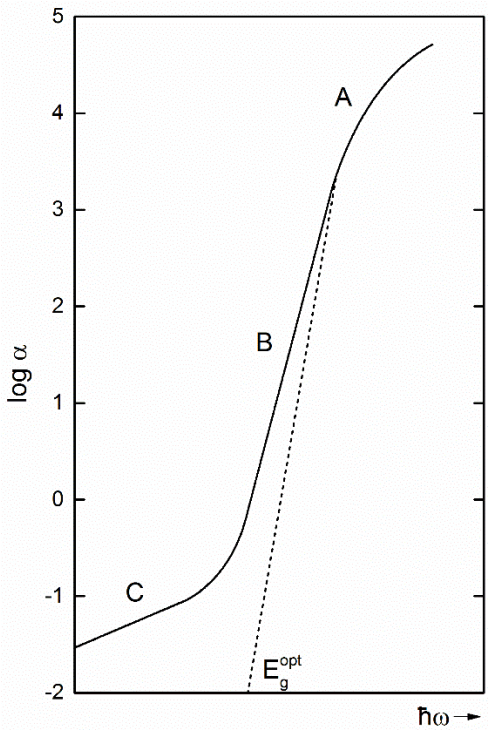

Fig. 1-3 Absorption edge spectra and its A, B, C parts – redraw from Tauc [24].

Plotting the square root of $\alpha\hbar\omega$ against photon energy should result in a straight line (fig. 1-4). On this plot the exponential absorption edge in the range $1 < \alpha < 10^4$ cm^{-1} appears only as a small tail at lower photon energies. The extrapolation of the linear portion intersects the abscissa at the energy E_g^{opt} which refers to optical bandgap [22].

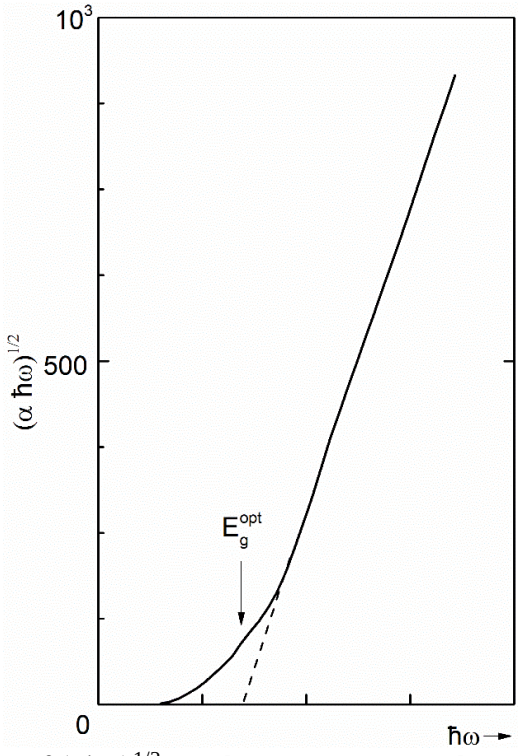

Fig. 1-4 Dependence of $(\alpha\hbar\omega)^{1/2}$ on photon energy – redraw from Fritzsche [22].

In a glass or amorphous film various kinds of disorder produce a tail of localized states extending from valence band and from the conduction band into the energy gap between these two bands [16]. It is convincing that the short-range normal-bonding structure governs the optical bandgap. Weak absorption tail (WAT), which substantially limits optical transparency, appears reflecting photoelectronic transitions from the valence band to un-occupied localized states below the conduction band. The states are produced by anti-bonding (σ*) levels of homo polar bonds such as As—As in As-based chalcogenides, which exist with concentrations of a few percent in covalent glasses. The σ* state makes electrons practically immobile by trapping [21]. The states in the Urbach edge are usually considered as localized. It has been believed that this region reflects some kinds of disorders such as thermal, compositional, heterogeneous and defective which tend to increase Urbach energy (E_U), [25]. However, there seems to exist a minimal value, $E_U \geq 50$ meV ($E_U = \gamma$ in Eq. (1-2), [20]). This value can be ascribed to intrinsic density fluctuation, with spatial scales of medium-range order, ~1 nm, which may provide thermally-activated percolative hole conduction [21]. Urbach energy is estimated from Eq. (1-3) where α_0 and E_0 fix an Urbach focus [25].

$$\alpha = \alpha_0 \exp\left[\frac{(\hbar\omega - E_0)}{E_U}\right]$$

Eq. 1-3

According 1-3, E_U is expressed as the inverse of the Urbach slope† of ln α against photon energy [26, 27].

Street and Mott [28] proposed the idea of defect model of three charged states – D^+, D^- and D^0 (the superscripts are denoting the total charge of such centre). Negatively charged defect D^- refers to dangling bond associated with under-coordinated atom, such as chalcogenide bonded

† Note that Eq. 1-3 is a transcript of Eq. 1-2 neglecting the temperature dependence. However, thermally induced structural disorder cause the increase in E_U.

to one other atom or pnictogen (*e.g.* As or Sb), bonded to two other atoms. Such dangling bond is occupied by two electrons [28, 29]. Removing the electron from dangling bond forms D^0. It is assumed that such atom will be attracted towards a fully coordinated neighbouring chalcogen atom. One of the lone-pair electrons of the fully coordinated atom will be used to form the bonding orbital, the other an antibonding orbital. This bond is not considered to be as strong as when a second electron is removed. In later case both lone-pair electrons from the neighbouring chains are used in bonding and the former single-coordinated chalcogen becomes three-fold coordinated D^+ centre [29]. The formation of D^+, D^- and D^0 centres is depicted in fig. 1-5.

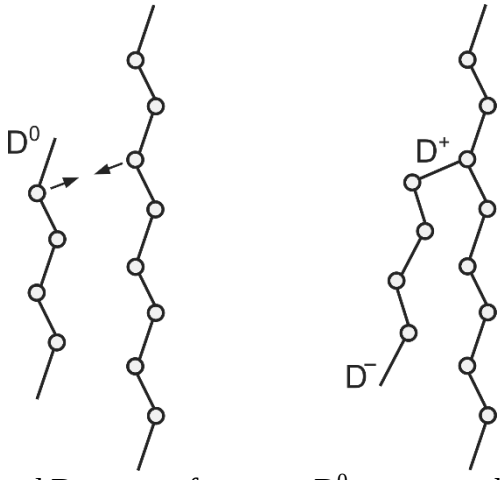

Fig. 1-5 Formation of D^+ and D^- centres from two D^0 centres at the end of selenium chain – redraw from Mott and Davis [29].

The changes in the electron occupation of the dangling bond causes the local lattice distortion [28]:

$$2D^0 \rightarrow D^+ + D^-$$

Eq. 1-4

Reaction is considered to be exothermic. Total energy associated with D^+ and D^- pair (both without spin) is lower than that of $2D^0$ (both D^0 with spin), [29].

Another insight on charged defects in lone-pair electrons was proposed by Kastner *et al.* [30]. The so called 'valence-alternation model' is based on the chemical-bond approach [31]. In contrast to Street and Mott model, they consider the neutral centre to be three-fold coordinated noted as C_3^0. This neutral centre has the antibonding electron residing symmetrically at the defect. Furthermore, in their notation, D^+ and D^- are denoted by C_3^+ and C_1^-, where C stands for chalcogenide and subscript indicates the coordination [29]. Dangling bond C_1^0 interacts with the lone-pair of a neighbouring chalcogen according [31]:

$$C_1^0 + C_2^0 \rightarrow C_2^0 + C_3^0$$

Eq. 1-5

During the reaction (Eq. 1-5), one of three electrons in lone pair orbitals at C_1^0 is transferred to a lower lying bonding orbital and one of the two lone-pair electrons at C_2^0 is transferred to a bonding orbital and the other to the antibonding orbital. Two C_3^0 then convert to C_3^+ and C_3^- by transferring two electrons from antibonding orbitals and the other two from bonding orbitals into lone pair orbitals [29]. Due to the strong phonon coupling, electrons at point defects (D) are considered to have effective negative correlation energy. The energy of formation E_D of a distant D^+D^- pair is calculated to be much less than E_g. According the Street model [32], the low

formation energy E_D of D^+D^- pair is considered to be of crucial importance, because it is much less than the exciton energy ($E_x \approx E_g$) in undisturbed lattice. The exciton (electron-hole pair bounded by Coulomb interaction) will therefore interact with the lattice to form a D^+D^- pair provided that the electron and hole are localized within a few lattice spacings of each other according:

$$exciton \rightarrow D^+ + D^-$$

Eq. 1-6

Considered configuration-coordinate diagram of nonradiative recombination in chalcogenide glasses is depicted in figure 1-6.

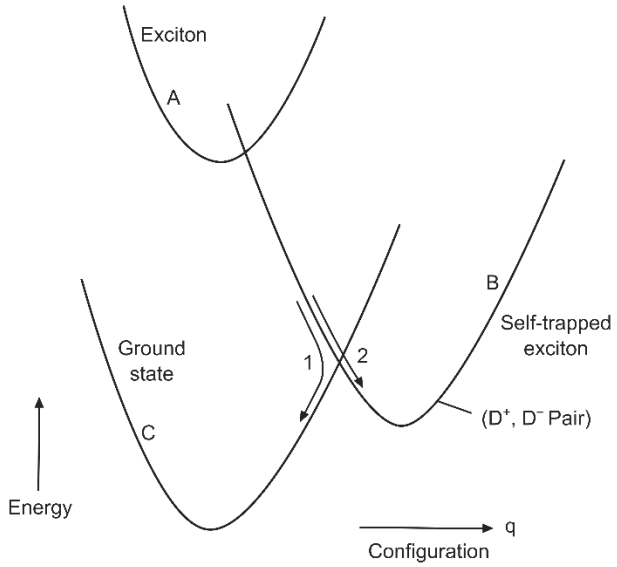

Fig. 1-6 Configuration-coordinate diagram of non-radiative recombination in chalcogenide glasses; Path 1 refers to recombination to the ground state through the self-trapped exciton, path 2 creates the metastable self-trapped exciton with return to the ground state by thermal excitation – Redraw from Street [32].

Street [32] has also proposed, that the creation of exciton in selenium chains and As-based chalcogenides may lead to the bond-switching process (fig. 1-7) possibly causing the photodarkening in amorphous chalcogenides [29].

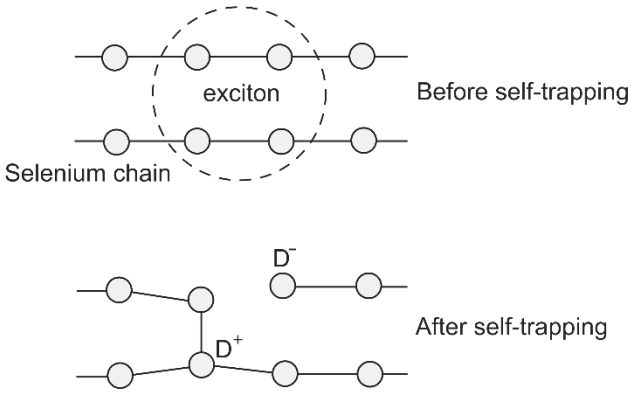

Fig. 1-7 Transformation of exciton in selenium chains into D^+D^- pair accompanied with atomic distortion – redraw from Street [32].

However, the charged defects (valence-alternation pairs) created during the illumination are not sufficient explanation for photostructural changes in amorphous chalcogenides [26]. Thus, other possible explanations must be considered. These are given in *Subchapter 3*. Moreover, the time-scale of such phenomena is probably very small. Recently, Specht [33] studied the self-trapped exciton formation in co-sputtered Ge-Sb-Se chalcogenide thin films using pump-probe spectroscopy at the picosecond time scale.

Absorption coefficient might be obtained from transmission measurements. Transmission coefficient is defined as a ratio of transmitted to incident power, I / I_0. Considering the film thickness as x, an absorption coefficient α and a reflectivity R, the radiation traversing the first interface is $(1 - R)I_0$, the radiation reaching the second interface is $(1 - R)I_0 \exp(-\alpha x)$ and only a fraction $(1 - R)\ (1 - R)I_0 \exp(-\alpha x)$ emerges. The portion internally reflected eventually comes out, but considerably attenuated. End result giving an overall transmission is than given by [23]:

$$T = \frac{(1 - \mathrm{R})^2 \exp(-\alpha x)}{1 - \mathrm{R}^2 \exp(-2\alpha x)}$$

Eq. 1-7

When the product αx is large, the denominator in Eq. (1-7) can be neglected; thus:

$$T \approx (1 - \mathrm{R})^2 \exp(-\alpha x)$$

Eq. 1-8

If R and x are known, the relation in Eq. (1-7) can be solved for α by means of:

$$\alpha = \frac{1}{x}\ ln\left[\frac{(1 - \mathrm{R})^2 + \sqrt{(1 - \mathrm{R})^4 + 4R^2T^2}}{2T}\right]$$

Eq. 1-9

Respectively according the Eq. (1-8) as [23]:

$$\alpha \approx \frac{1}{x}\ln\left[\frac{(1 - R)^2}{T}\right]$$

Eq. 1-10

If the reflectivity is not known, the absorption coefficient α may be calculated from the transmission by the Swanepoel method developed for amorphous silicon [34]. The transmission of homogeneous thin films on the transparent substrate is a complex function T = T(λ, s, n, d, α), where s stands for the refractive index of the substrate and d is the thickness of the film. In the terms of absorbance x it can be written as x(λ) = exp(-αd).

$$T = \frac{A'x}{B' - C'x + D'x^2}$$

Eq. 1-11

where the complex functions A', B', C' and D' are

$A' = 16s(n^2 + k^2)$

$B' = [(n + 1)^2 + k^2][(n + 1)(n + s^2) + k^2]$

$C' = [(n^2 - 1 + k^2)(n^2 - s^2 + k^2) - 2k^2(s^2 + 1)]\ 2cos\varphi$
$\quad - k[2(n^2 - s^2 + k^2) + (s^2 + 1)(n^2 - 1 + k^2]\ 2sin\varphi$

$D' = [(n - 1)^2 + k^2]\ [(n - 1)(n - s^2) + k^2]$

$\varphi = 4\pi nd/\lambda$

$x = \exp(-\alpha d)$

$\alpha = 4\pi k/\lambda$

In the transparent region where $\alpha \approx 0$ so $x \approx 1$, the Eq. 1-11 can be solved as [35]:

$$T = \frac{A}{B - C\ cos\varphi + D}$$

Eq. 1-12

where

$A = 16n^2s$

$B = (n + 1)^3 + (n + s^2)$

$C = 2\ (n^2 - 1)\ (n^2 - s^2)$

$D = (n - 1)^3\ (n - s^2)$

$\varphi = 4\pi nd/\lambda$

Refractive index dispersion is obtained from experimentally observed peaks and valleys of transmission interference fringes. Experimental values of transmission at the minimum (T_m) and maximum (T_M) points of a particular interference fringes are used. In the transparent region refractive index is calculated as [34]:

$$n = \left[M + (M^2 - s^2)^{1/2}\right]^{1/2}$$

Eq. 1-13

where

$$M = \frac{2s}{T_m}\frac{s^2 + 1}{2}$$

Eq. 1-14

respectively in the region of weak and medium absorption ($\alpha \neq 1$ so $x < 1$):

$$M = 2s\frac{T_M - T_m}{T_M T_m} + \frac{s^2 + 1}{2}$$

Eq. 1-15

Values of T_M and T_m should correspond to the same λ so the particular fringe valley T_m has a counterpart T_M' and fringe peak T_M has a counterpart T_m'. Values of T_M' and T_m' are obtained by enveloping of the peaks and valleys as shown in the figure 1-8 [35].

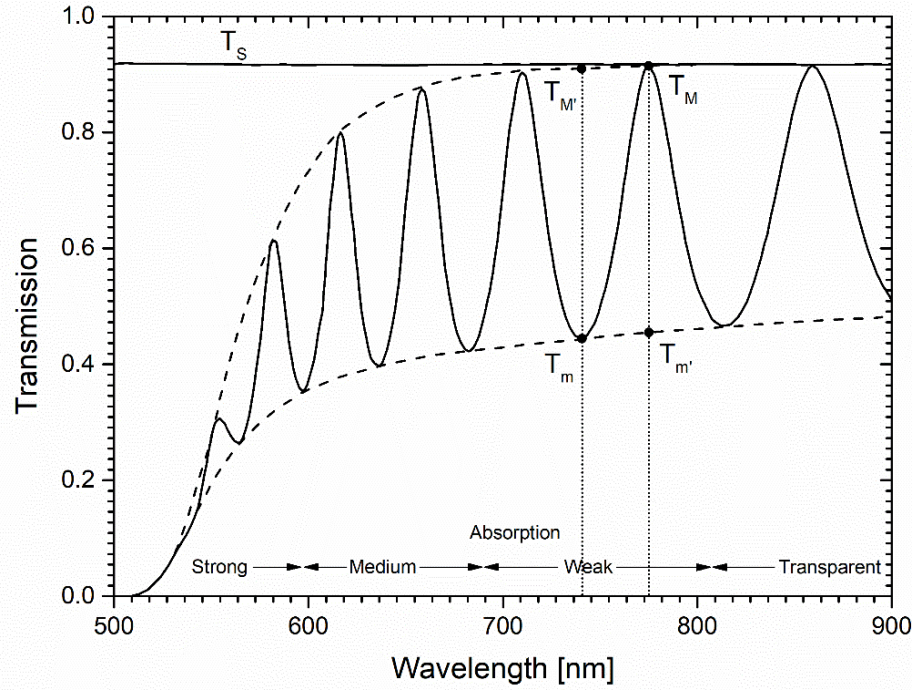

Fig 1-8 Simulated transmission (full curve) of a 1 μm film of amorphous hydrogenated silicon (α-Si:H) on a flint glass substrate – adapted from Swanepoel [34].

Finally, the absorption coefficient for an absorbing film on transparent substrate is given by:

$$\alpha = \frac{1}{d}\ln\frac{(1 - R_1)(1 - R_2)(1 - R_3)}{T}$$

Eq. 1-16

where R_1, R_2 and R_3 are reflection coefficients between air-thin films, thin film-substrate and substrate-air. It is assumed that the other reflections from interfaces are neglected. For the case when the square of n is significantly higher than k, the reflection coefficients can be estimated using Fresnel's formula for normal incident of light [35]:

$$R_1 = \left(\frac{n - 1}{n + 1}\right)^2$$

Eq. 1-17

$$R_{12} = \left(\frac{n - s}{n + s}\right)^2$$

Eq. 1-18

$$R_1 = \left(\frac{s-1}{s+1}\right)^2$$

Eq. 1-19

1.2. Index of refraction

The refraction of light occurs when light advances into optically different media. The refraction of light is determined from the index of refraction *n*:

$$n = \frac{c}{v}$$

Eq. 1-20

where *v* is the speed of light propagating through the media [36]. In the media with the strong absorption, such as semiconducting material, the refractive index becomes complex function of the light wave frequency [37]. Complex refractive index, n_c, having the real part *n* and the imaginary part *k* is related to the complex relative permittivity (dielectric constant), [38]:

$$n_c = n - ik = \sqrt{\varepsilon_c} = \sqrt{\varepsilon_1 - i\varepsilon_2}$$

Eq. 1-21

The real part and the imaginary part of relative permittivity are expressed as $\varepsilon_1 = n^2 - k^2$ and $\varepsilon_2 = 2nk$ [38].

In materials having normal dispersion (normal because it occurs in most of the optically homogeneous materials), the linear refractive index in the optical transparent region may be expressed by the Cauchy dispersion formula:

$$n(\lambda) = \mathrm{A} + \frac{B}{\lambda^2} + \frac{C}{\lambda^4}$$

Eq. 1-22

or Sellmeier dispersion formula:

$$n^2(\lambda) = \mathrm{A} + \frac{B\lambda^2}{\lambda^2 - C} + \frac{D\lambda^2}{\lambda^2 - E}$$

Eq. 1-23

The number of terms in Eq. 1-22 and 1-23 may vary.

Wemple and Di-Domenico [39] developed the single-oscillator model for the linear dispersion in various materials including amorphous semiconductors and glasses based on the Kramers-Kronig relations [40]:

$$n_0^2(\omega) - 1 = \frac{E_0 E_d}{(E_0^2 - (\hbar\omega)^2)}$$

Eq. 1-24

where E_0 is the energy of the effective dispersion oscillator. The value of E_0 is typically near the main peak of imaginary part of dielectric function ε_2. E_d is the dispersion energy and is almost independent of E_0. Furthermore, E_d strength does not depend on the scale of ε_2 spectrum nor on the volume density of valence electrons. Dispersion energy E_d and the single oscillator energy E_0 are obtained from the slope and the intercept of linear fit of $(n^2-1)^{-1}$ against $(\hbar\omega)^2$. Linear refractive index in eq. 1-24 is defined for a specified direction of the light polarization [39].

2. Nonlinear optical properties of amorphous chalcogenides

Introduction

The invention of laser in the 1960s, the light source with the intensity of several orders of magnitude higher than the previous known light sources, allowed the exploration of the brand new field of optics – nonlinear optics. It was find out that at such high intensities, the optical response of the material occurs in the nonlinear manner on the strength of the applied optical field [41]. Nonlinearities have found its application for all-optical switches, power stabilizers, soliton fibres, supercontinuum generators, *etc*. Furthermore, nonlinear phenomena of second-harmonic generation under proper experimental conditions can lead to the conversion of incident beam frequency (ω) to radiation at a second-harmonic frequency (2ω). One common use of such phenomena is found in the output conversion of a fixed-frequency laser to a different spectral region. For example, Nd:YAG laser operating in near infrared spectral region at 1 064 nm is routinely converted to its second-harmonic frequency (*i.e.* 532 nm) *via* Q-switching in the middle of the visible spectrum [41]. Chalcogenide glasses exhibit of about two orders of magnitude higher nonlinear refractive index when compared with oxide glasses [42]. Moreover, second-harmonic generation in optically isotropic chalcogenide glasses may occur [43]. When the optical pulse travels through the medium with high nonlinear refractive index, it becomes distorted in phase (self-phase modulation) and in envelope shape (self-steepening) [44]. The former is responsible for supercontinuum (SC) generation in various materials. SC generation in chalcogenide fibres and waveguides in Mid-IR region seems to have a great potential [45, 46].

Finally, high "Kerr-like" nonlinearities in combination with proper dispersion may lead to solitary wave formation and propagation in chalcogenide glasses [47].

Thus, amorphous chalcogenides are of interest in the wide spectrum of possible applications such as high-speed optoelectronic devices and photonic switching [48]. Such devices, operating typically on ps time scales, requires materials with high nonlinear refractive index n_2 or nonlinear absorption β at telecommunication wavelengths (*i.e.* 1.55 μm), [14]. Usually, they are investigated in the form of optical fibres or waveguides. Some examples of different types of geometry of channel waveguides and planar (slab) waveguide are shown in figure 2-1.

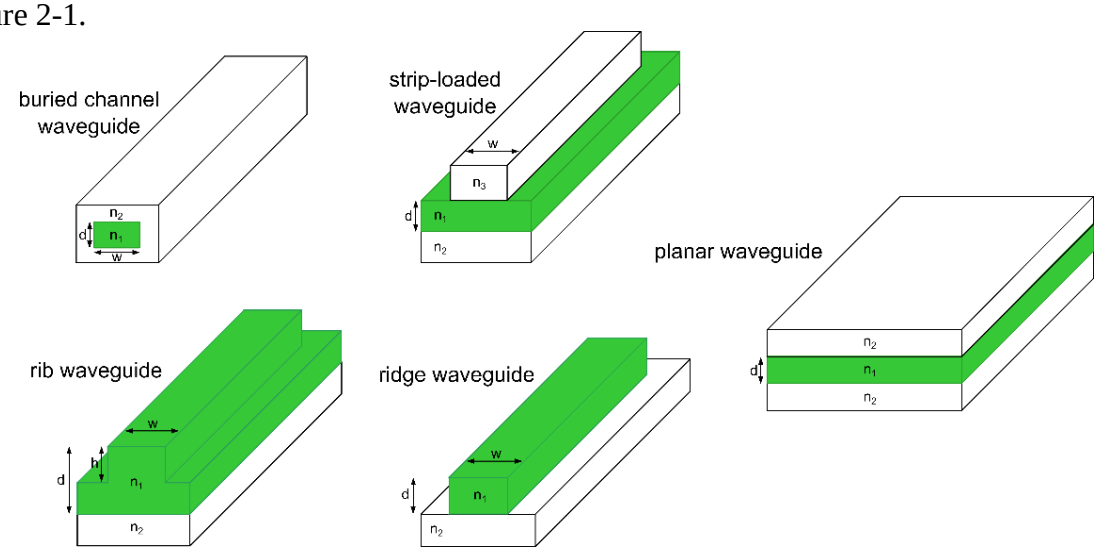

Fig. 2-1 Waveguides with different types of geometry; n_i – refractive index, $n_1 > n_2$, $n_1 > n_3$, w – waveguide width, d – waveguide height, h – height of waveguide segment.

2.1. Nonlinear index of refraction

Nonlinear response of refractive index is very important phenomena, which involves several diverse physical effects such as optical Kerr effect, saturation or cascading effects. Among these, the former is directly related to the third order nonlinear polarization [49]. Material response to internal electric fields is manifest in an electronic susceptibility. The relation between the linear susceptibility and linear refractive index is expressed as $\chi^{(1)} = n_0^2 - 1$. The interaction of transparent material with an intense light can cause that susceptibility becomes nonlinear. This may be expressed by means of a Taylor expansion in the electric field in the scalar form [38, 50]:

$$\chi(E) = \chi^{(1)} + \chi^{(2)}E + \chi^{(3)}E^2 + \chi^{(4)}E^3 \ldots$$

Eq. 2-1

The nonlinear response of the material to the presence of intense light is represent by all orders higher than $\chi^{(1)}$. It should be noted, that electrical susceptibility is tensor so the vector component of the electric fields has to be taken into account. The nonlinear optical susceptibility $\chi^{(3)}$ in esu units is related to the linear optical susceptibility $\chi^{(1)}$ by the semi-empirical Miller's rule [51]:

$$\chi^{(3)} = \frac{n_2 n_0^2}{0.0395} = \alpha \left[\frac{(n_0^2 - 1)}{4\pi}\right]^4$$

Eq. 2-2

where n_2 is a nonlinear refractive index and α is Miller's coefficient having the value of 2.7×10^{-10} for chalcogenide glasses. The light wave propagating in the medium is affected by susceptibility by means of nonlinear polarizability [49]. Nonlinear electronic polarizability (P_{NL}) in the simplified form can be expressed as [52]:

$$P_{NL} = \chi^{(2)}E^2 + \chi^{(3)}E^3 + \ldots$$

Eq. 2-3

The nonlinear refractive index (a third order nonlinearity) is often expressed in terms of intensity (I) as [38, 49, 50]:

$$n = n_0 + n_2 I$$

Eq. 2-4

respectively in terms of the field strength as [53]:

$$n = n_0 + n_2 E^2 + \ldots$$

Eq. 2-5

In the same manner, two-photon absorption (2PA) coefficient β, sometimes referred as nonlinear absorption coefficient [7] may be expressed as:

$$\alpha = \alpha_0 + \beta I$$

Eq. 2-6

2PA, which is just the simplest example of multi-photon absorption, suggests that despite the fact that the material is transparent at low intensities, as the intensity grows, the absorption increases.

Quantities n_2 and β are connected through nonlinear Kramers-Kronig relations. Figure 2-2 shows spectral dependencies of α, n_0, β, n_2 for an ideal semiconductor having energy gap E_g. As seen, β and n_2 give broad peaks at $\hbar\omega \approx 0.7E_g$ and $\hbar\omega \approx E_g/2$ respectively. Furthermore, $\beta = 0$ and n_2 is great at these energies.

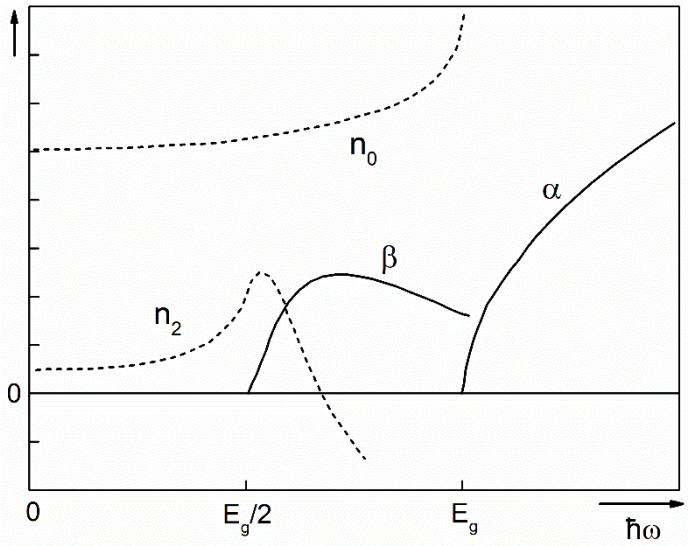

Fig. 2-2 Spectral dependence of linear absorption coefficient α, linear refractive index n_0, 2PA coefficient β and nonlinear refractive index n_2 for an ideal amorphous semiconductor. The scales of *Y* axis are arbitrary – adapted from Tanaka [14].

The value of n_2 is quite small in comparison with n_0, so it can be negligible in low beam intensity (*i.e.* linear regime). Furthermore, n_2 rises with n_0 with the proportionality factor of *I*. In the fast response systems, the main contribution to n_2 is nonlinear polarizability or resonant-type effects. Thermal effect and electrostriction are very slow so they do not contribute to the n_2. In other words, nonlinear polarizability is significant for the third-order nonlinearity of glasses. For optically isotropic materials, only the third-order electronic susceptibility $\chi^{(3)}$ contributes to the nonlinear optical response [52].

It is well known that in chalcogenide glasses the values of $\chi^{(3)}$ and therefore n_2 are about two to three orders of magnitude higher than that of silica [54]. Z-Scan technique, developed by Sheik-Bahae *et al*. [55], is a sensitive single-beam technique for measuring nonlinear refractive index and nonlinear absorption coefficient based on focusing a laser beam through a thin sample (fig. 2-3). Self-focusing of an intense Gaussian beam in the nonlinear medium results in beam distortion, which enables extraction of n_2 value. The light transmitted by a small aperture in the far field is then detected. The far-field aperture transmittance is measured for a constant laser input as the sample is scanned along the z-direction through the focus of the lens [7].

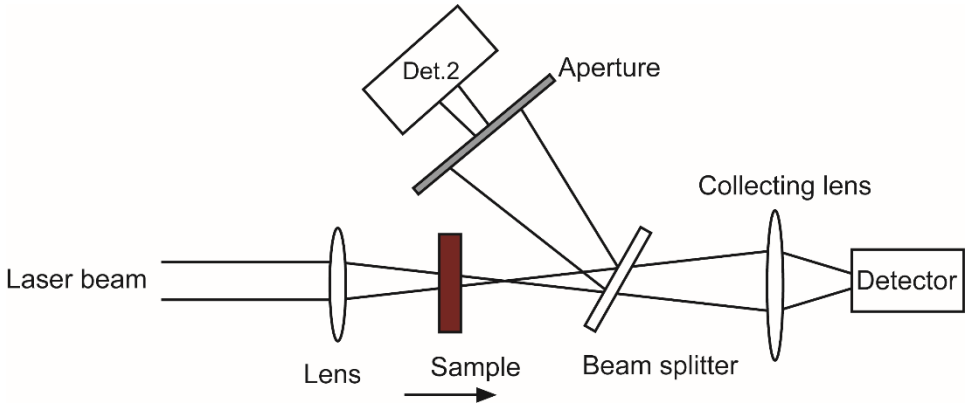

Fig. 2-3 Schematic illustration of a simultaneous closed-aperture and open aperture Z-scan measurement. The transmitted beam is split after the sample; the first detector measures the open-aperture transmittance and the detector marked Det.2 measures the closed-aperture transmittance as a function of the sample position. – redraw from Samoc *et al*. [56].

2.2. Estimation of nonlinear optical properties

Introduction

Empirical and semi-empirical calculations of nonlinear optical properties by means of nonlinear refractive index n_2 and two-photon absorption coefficient β, are a very useful tool to estimate the behaviour of the material for the nonlinear optics applications. Many attempts have been made in order to (semi)empirically estimate the values of n_2 and/or β of various materials including non-crystalline chalcogenides [57-65]. These are summarized in the table 2-1.

Table 2-1 Models for the estimation of nonlinear refractive index and/or 2PA coefficient β.

Reference	Materials	Quantity	Year
Fournier and Snitzer, [59]	optical glasses	n_2	1974
Boling *et al.*, [57]	optical glasses	n_2	1974 (1978)
Lines, [63]	optical crystals	n_2	1990
Sheik-Bahae *et al.*, [64]	direct-gap semiconductors	n_2, β	1990
Lenz *et al.*, [62]	Se-based glasses	n_2	2000
Tichá and Tichý, [65]	chalcogenide glasses	n_2	2002
Dinu, [58]	Indirect-gap semiconductors	n_2, β	2003
Garcia and Avanaki, [60]	germanium	β	2012

It should be noted, that so far, no model has been designed for chalcogenide thin films. Clearly the wide variability in the behaviour of thin films of various composition, structure and photosensitivity makes such design very difficult (if not impossible). Most of the models were developed for ionic crystals having a relatively large gap between the valence and conduction bands when compared to chalcogenides. Moreover, in such materials, the exciton formation and various defect states do not affect the band edges as much as in disordered solids [23, 66]. Other difficulties may rise from the photosensitivity of chalcogenide glasses and thin films. Having the lone-pair states at the top of the valence band, photostructural changes in amorphous chalcogenides cause the shift of the fundamental absorption edge accompanied with the change

in the refractive index. The photosensitivity of amorphous chalcogenides which may rise even at the energies of irradiation below the energy band gap [67] may act as a limiting factor when it comes to the application of these materials in the field of nonlinear optics.

2.2.2. Semi-empirical calculations of n_2 and/or β

Most of the following models have its origins in the various forms of so-called Miller rule [68, 69]. Fournier and Snitzer [59] developed the three-level quantum mechanical model consisting of a ground state coupled to the lower of two excited states by a bandgap much larger than the splitting of the two excited states [57]. For silicate glasses, much of the oscillator strength is associated rather with transitions between localized states. The nonlinear refractive index in esu units ($cm^3 \cdot erg^{-1}$) can be obtained from:

$$n_2 = \frac{(n^2+2)^2(n^2-1)}{48\pi N n_0}\frac{E_d}{E_0^2}$$

Eq. 2-7

where N is the density of ions, n_0 refers to linear refractive index, E_d and E_0 are dispersion energy and average oscillator energy obtained from the dispersion relation defined by Wemple-DiDomenico.

The empirical model proposed by Boling *et al.* [57], sometimes called BGO model [70] (by the initials of the authors – Boling, Glass and Owyoung), for n_2 (10^{-13} esu) is written as:

$$n_2 = \frac{68(n_d-1)(n_d^2+2)^2}{v_d\left[1.517+\frac{(n_d^2+2)(n_d+1)}{6n_d}v_d\right]^{1/2}}$$

Eq. 2-8

where v_d stands for Abbe number defined as $v_d = (n_d-1)/(n_f-n_c)$, n_d being the linear refractive index at λ = 587.5 nm, n_f at λ = 486.1 nm and n_c at λ = 656.2 nm.

Furthermore, Lines [63], proposed the simple proportionality (in esu units):

$$n_2 \sim \frac{(n_0^2-1)d^2}{(n_0 E_0^2)}$$

Eq. 2-9

where d is the bond length in Ångströms.

The concept of Sheik-Bahae [55] developed for crystalline direct-gap semiconductors may serve as a rough approximation for non-crystalline solids [14]. Following equations lean on the basic assumptions for quantum-mechanical formulations, Kramers-Kronig relations and simple two parabolic band model [14, 71]. According to this model, the contributions of two-photon absorption, electronic Raman and optical Stark effects in the nonlinear response of the material may take part [72]. The process responsible for 2PA also gives a dominant contribution to n_2. Nonlinear refractive index in $m^2 \cdot W^{-1}$ is expressed as[†]:

[†] In the original paper of Sheik-Bahae, the quantity on the left side of Eq. 2-10 is marked as γ instead of n_2 called Kerr coefficient. The relationship between n_2 (in esu units) and γ in $m^2 \cdot W^{-1}$ is $n_2[\text{esu}] = (cn_0/40\pi) \cdot \gamma$ [SI].

$$n_2 = K\frac{\hbar c\sqrt{E_p}}{2{n_0}^2 {E_g^{opt}}^4} G_2(\hbar\omega/E_g^{opt})$$

Eq. 2-10

where K = 3100 cm·GW^{-1}eV$^{5/2}$, E_p = 21 eV (Kane energy) which is essentially the material independent for the most semiconductors [73]. G_2 is a normalized dispersion function given by:

$$G_2(x) = \frac{-2 + 6x - 3x^2 - x^3 - \frac{3}{4}x^4 - \frac{3}{4}x^5 + 2(1-2x)^{\frac{3}{2}}\Theta(1-2x)}{64x^6}$$

Eq. 2-11

where Θ is Heaviside step function and equals to zero when $x < 0.5$. Similarly, 2PA coefficient β may be expressed as:

$$\beta = K\frac{\sqrt{E_p}}{{n_0}^2 {E_g^{opt}}^3} F_2(2\hbar\omega/E_g^{opt})$$

Eq. 2-12

where the dispersion function is

$$F_2(2x) = \frac{(2x-1)^{\frac{3}{2}}}{2x^5}$$

Eq. 2-13

The dispersion function F_2 equals to zero for $2x < 1$. The shape of the dispersion functions for direct-gap semiconductors, G_2 and F_2, is depicted in the figure 2-4.

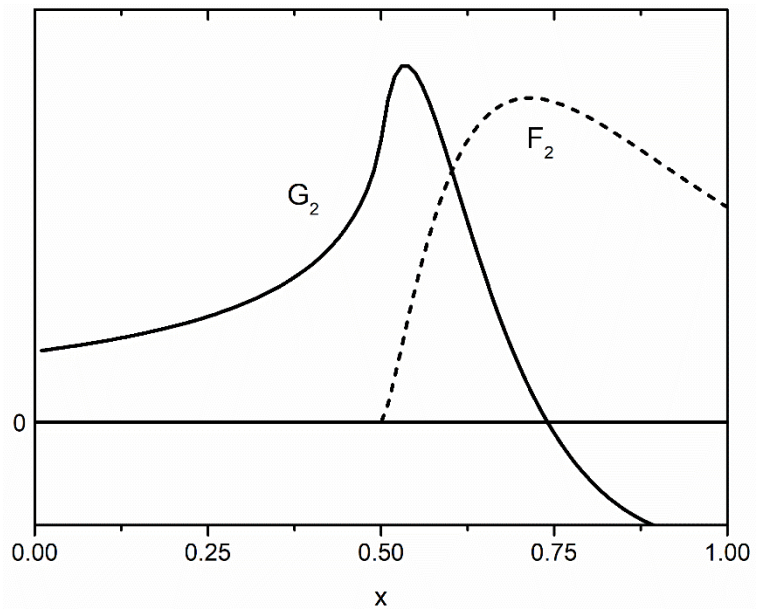

Fig. 2-4 Functions G_2 (solid line) and F_2 (dashed line) as defined for direct-gap semiconductors.

As seen, dispersion functions G_2 and F_2 give broad peaks at around 0.5 and 0.7 respectively. Thus, peaks of n_2 and β are found at the energies of around $E_g/2$ and $0.7E_g$ respectively [14].

Lenz [62] model developed for bulk Se-based glasses and which uses some assumptions developed for ionic crystals [57, 70, 74] in combination with Sheik-Bahae's dispersion function, defines the nonlinear refractive index in $cm^2 \cdot W^{-1}$ as:

$$n_2 = 1.7 \times 10^{-14}(n_0^2 + 2)^3(n_0^2 - 1) \times (d/n_0 E_0)^2 G_2(\hbar\omega/E_g^{opt})$$

Eq. 2-14

where d (in nanometers) is the mean cation-anion bond length.

The model proposed by Tichá and Tichý [65] is based on the Wemple-DiDomenico single oscillator formula and the generalized Miller's rule, $\chi^{(3)} = A(\chi^{(1)})^4$, [75].

For chalcogenide glasses, the linear optical susceptibility in the first approximation is given by relation:

$$\chi^{(1)} = \frac{(n_0^2 - 1)}{4\pi}$$

Eq. 2-15

combining equations 1-24 and 2-15, one can obtain:

$$\chi^{(1)} = \frac{E_0 E_d}{4\pi(E_0^2 - (\hbar\omega)^2)}$$

Eq. 2-16

which in the limit of $\hbar\omega \to 0$ gives:

$$\chi^{(1)} = \frac{E_0 E_d}{4\pi}$$

Eq. 2-17

$\chi^{(3)}$ is then obtained employing the generalized Miller's rule as:

$$\chi^{(3)} = \frac{A}{(4\pi)^4 (E_d/E_0)^4} = \frac{A}{(4\pi)^4 (n_0^2 - 1)^4}$$

Eq. 2-18

where A value is 1.7×10^{-10} for $\chi^{(1)}$ in esu units. Finally, n_2 can be calculated as:

$$n_2 = \frac{12\pi\chi^{(3)}}{n_0}$$

Eq. 2-19

Recently, Střižík *et al.* used the similar approach for obtaining the nonlinear refractive index in erbium doped Ge-Ga-Sb-S thin films [76]. However, in their work the Sellmeier dispersion was used for describing the n_0 (λ) instead of WD one.

Dinu [58] defined F_2 function for indirect-gap semiconductors as:

$$F_2(2x) = \frac{(2x-1)^4}{2x^7}$$

Eq. 2-20

In this model third-order nonlinear processes in indirect semiconductors are considered to be mediated by phonon-assisted transitions. Therefore, the resulting shape of the absorption edge is considered to be smooth for indirect-gap semiconductors. Comparison of the shape of F_2 function defined by Sheik-Bahae for direct-gap semiconductors and F_2 for indirect-gap semiconductors defined by Dinu is depicted in the figure 2-5.

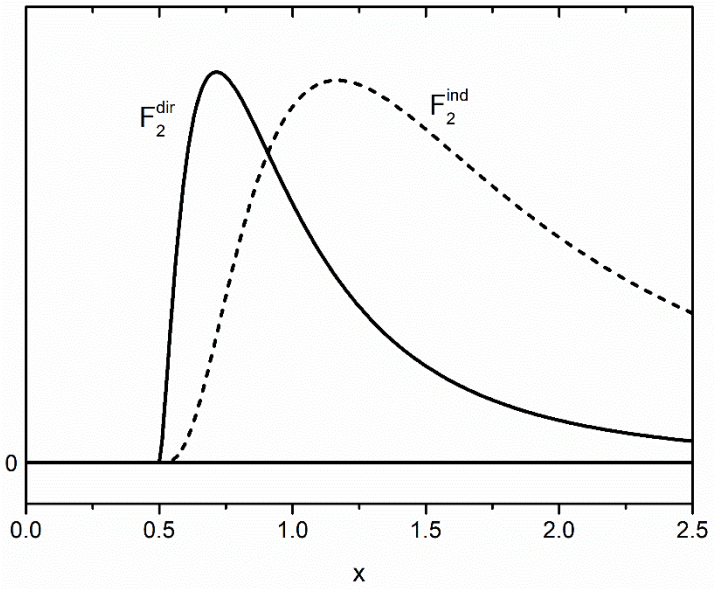

Fig. 2-5 Functions F_2 for direct-gap (solid line) and indirect-gap (dashed line) semiconductors.

As seen, the maximum of the function F_2 for indirect bandgap is at ~7/6, so the maximum of β peak is found at around $\hbar\omega \approx (7/6)E_g$, [58]. The β is defined as:

$$\beta = C_2 \cdot F_2(2\hbar\omega/E_g^{opt})$$

Eq. 2-21

where E_g^{opt} is indirect gap and C_2 is a constant defined as:

$$C_2 = \frac{Z_A^2 E_{ph}(2N_{Kx} + 1 \pm 1)}{8\rho c_s^2 {E_g^{opt}}^3} \cdot \left(\frac{m_c^2}{m_v}\right)^{\frac{1}{2}} \cdot \left\{ \frac{128e^4}{\pi^2 \hbar^3 (\varepsilon_0 n_0 c)^2} \cdot \int_0^1 (1-x)^{\frac{1}{2}} \cdot x^{\frac{1}{2}} dx \cdot \left[(1-x)^{\frac{1}{2}} + x^{\frac{1}{2}} \cdot \left(\frac{m_c^2}{m_v}\right)^{\frac{1}{2}} \right]^4 \right\}$$

Eq. 2-22

with Z_A being an acoustic deformation potential, E_{ph} phonon energy (in electron volts), N_{Kx} is a phonon occupation number ($N_{Kx}=\exp(E_{ph}/k_BT)^{-1}$), ρ density (in kg·m^{-3}), c_s is speed of sound in the material (in m·s^{-1}), m_c effective mass of conduction band (in kg), m_v effective mass of valence band (kg), e elementary charge (in C) and ε_0 vacuum permittivity (in F·m^{-1}). The ± sign takes into account the phonon absorption/emission.

Two expressions are then summed. Nonlinear refractive index n_2 is then derived from β by Kramers-Kronig relation:

$$n_2 = C_2 \cdot \frac{c\hbar}{\pi E_g^{opt}} \cdot G_2(2\hbar\omega / E_g^{opt})$$

Eq. 2-23

2.2.3. Figure of merit

One should consider the trade-off between the high nonlinearities and optical losses due to the 2PA. The effective operation of a nonlinear device is usually expressed by means of figure-of-merit:

$$FOM = \frac{2\beta\lambda}{n_2} < 1$$

Eq. 2-24

The above criterion for the given operation wavelength (λ) should be meet in order to enhance the performance of the device [77]. Figure of merit can be also expressed as [62]:

$$FOM = \frac{n_2}{\lambda\beta}$$

Eq. 2-25

2.3. Self-focusing effect

When the intense light beam is focused into a material with a third order nonlinearity, the phase velocity decreases with increasing intensity near the center of a beam [50]. As shown on the figure 2-6, the refractive index gradient is induced in the medium as the nonlinear index follows the shape of the beam. When the nonlinearity is positive, greater index and hence larger phase retardation is induced on-axis where the beam is more intense while leaving it unchanged

in the beam's tails [49, 50, 78]. Thus the value of n_2 has to be positive for self-focusing (lens focus) to occur [78].

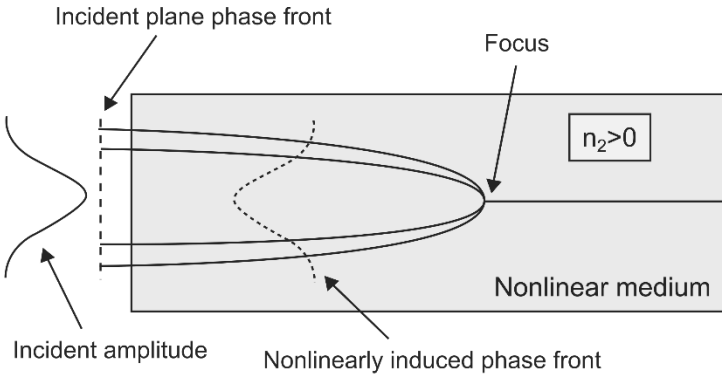

Fig. 2-6 Self-focusing effect in a nonlinear medium - redraw from Sutherland [49].

2.4. Propagation of Kerr spatial soliton in amorphous chalcogenides

Optical beam propagating in the medium without affecting its properties undergo natural diffraction and broadens with the distance (fig. 2-7 b), [78]. The circular beam with the diameter D is expected to diffract with an angular divergence of $\theta_d \approx 1.22\lambda/n_0 D$, [53]. For the beam with a sufficient intensity, the nonlinearity of the medium can cause a large dielectric discontinuity at the edge of the beam. In such regime, the critical angle for total internal reflection θ_c is larger than θ_d so the beam cannot diffract. For beams with larger diameter angles θ_c and θ_d becomes smaller and *vice versa*. Thus, there is a particular value of power, independent of the beam diameter, at which the beam self-trapping occurs. This value is $P_{cr} = 1.22^2\pi\lambda^2/32n_2{n_0}^2$, [50]. According this approximation, a beam of a certain power may be trapped at any arbitrary diameter without spreading and its power level decreases with λ^2.

Self-trapped optical beam that propagates in a nonlinear medium without diffraction is called optical spatial soliton [79]. As shown in the figure 2-7 it represents an exact balance between diffraction and self-focusing effect [47, 50, 79].

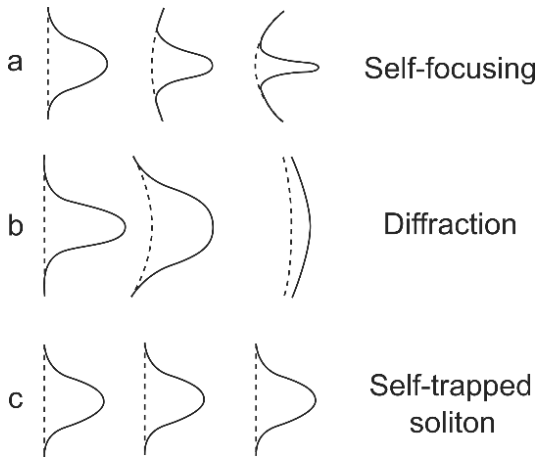

Fig. 2-7 Spatial beam profiles (solid lines) and phase fronts (dashed lines) of (a) self-focusing, (b) diffraction and (c) soliton propagation - redraw from Stegeman and Segev [78].

The propagation distance of spatial solitons is limited to only a few centimeters when compared with their temporal counterparts occurring in the optical fibers. This limitation is due to the fabrication technology or material losses [80]. Another limitation comes with the high intensity requirements for soliton to occur. For fused silica having $n_2 \cong 3\times10^{-16}$ $cm^2 \cdot W^{-1}$ the intensities of about few $TW \cdot cm^{-2}$ are required for the soliton formation at $\lambda = 1$ μm with beam width a ≅ 10 μm [81].

2.5. Plasmon-soliton coupling

Surface plasmon polaritons (surface plasmons – SPs) are coherent surface oscillations of conduction electrons and the electromagnetic field localized on the surface of conductor (usually metal) [82, 83]. In the field of photonics, the enhancement of nonlinear processes such as second harmonic generation was reported by Quail and Simon in 1984, [84]. Furthermore, in 1985 Aiyatsu *et al.* discussed the nonlinear waves guided by a metal film bounded by media with intensity-dependent refractive index (*i.e.* material with Kerr nonlinearity) [85]. Walasik *et al.* proposed several stationary nonlinear solutions in one-dimensional nonlinear metal-dielectric structures [86]. Among them, the four-layer configuration consisting of nonlinear dielectric, linear dielectric, metal and air [87], allows to find plasmon-solitons for high index contrast configurations at low peak intensities [86]. Such solution is depicted in fig. 2-8.

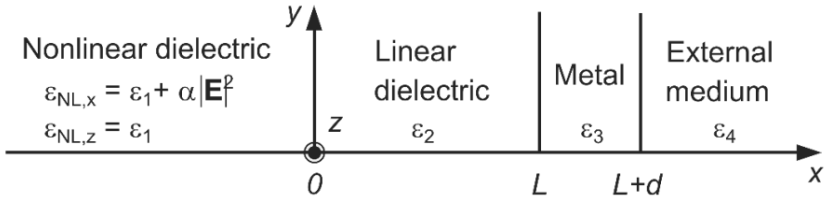

Fig. 2-8 4-layer nonlinear model scheme. E_j stands for linear permittivity of *j*-th layer ($j \in \{1, 2, 3, 4\}$) – adapted from Walasik *et al.*, [88].

Plasmon-soliton coupling in planar waveguides based on this model was recently demonstrated experimentally by Kuriakose *et al.* [89]. In their experiment, the metal-dielectric structure consists of medium with Kerr nonlinearity placed on lower refractive index medium with a thin dielectric layer and metallic film deposited on top. Specifically, the medium with Kerr nonlinearity is amorphous chalcogenide film ($Ge_{28.1}Sb_{6.3}Se_{65.6}$) of thickness of 3 μm deposited by RF sputtering technique on thermally oxidized silicon substrate. Dielectric layer deposited on the top of the chalcogenide waveguide is silicon oxide with the thickness of 10 nm. Finally, the metallic film is 30 nm thick gold layer [89].

3. Structure of amorphous chalcogenides

The amorphous structure in the atomic scale can be classified in two categories [17]. First, the normal bonding structure which characterizes the vast majority of atoms in an amorphous solid [90]. This include short-range and medium-order. The former describes the way in which an atom is bonded to its nearest neighbours by coordination number, bond-length and the bond angle. The later reflects dihedral angle, ring, intermolecular and dimensional structure. Second category of the atomic structure are various defects, such as dangling-bonds and wrong bonds (also called homopolar bonds) [17, 20].

3.1. Chemically ordered network model

Coordination of constituents plays a significant role in the local structure of amorphous solids. Usually, germanium has the coordination number $Z = 4$ (according the $8 - N$ rule, where N is the number of valence electrons). This leads to the presence of [$GeSe_{4/2}$] tetrahedron as the main structural unit cross-linked either at corners (CS - corner-sharing [$GeSe_{4/2}$] tetrahedra – fig. 3-1a) or at edges (ES - edge-sharing [$GeSe_{4/2}$] tetrahedra – fig. 3-1b) [20] in stoichiometric GeS(e) binary glasses. With the change in the cation from germanium to arsenic (or antimony), Z decreases from 4 to 3 In As(Sb)S(Se, Te) binaries. The main structural unit in such binary chalcogenides is [As(Sb)$Se_{3/2}$] pyramidal unit (fig. 3-1d). Although the stoichiometry in mentioned systems would normally allow the creation of energetically more favourable heteropolar bonds only, the deviations from stoichiometry during the glass processing give rise to presence of homopolar bonds (fig. 3-1c) [20]. Despite the fact that the coordination of gallium still remains a bit controversial, it is generally accepted that when incorporated in glasses, it adopts a 4-fold coordination possibly forming [$GaSe_{4/2}$] tetrahedral units [91, 92]. Finally, chalcogen elements, having 6 valence electrons have $Z = 2$. Therefore, in pure chalcogens S(Se, Te), the structure is molecular as rings or short chains are formed [17]. Some of the predominant structural units identified in Ge-Sb-Se thin films are depicted in the figure 3-1.

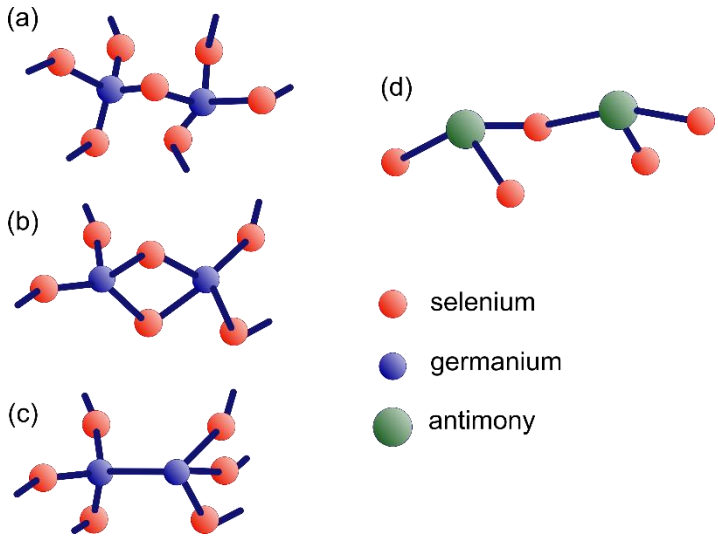

Fig. 3-1 Some of the typical structural units in Ge-Sb-Se amorphous network: **(a)** corner-sharing (CS) [$GeSe_{4/2}$] tetrahedra, **(b)** edge-sharing (ES) [$GeSe_{4/2}$] tetrahedra, **(c)** Ge–Ge homopolar bonds in [$Ge_2Se_{6/2}$] entities and **(d)** [$SbSe_{3/2}$] pyramidal units – edited from Micoulaut *et al.*[93].

In multicomponent glasses Ge_x-P_y-Ch_z, Tichý and Tichá [94] defined the quantity *R* by:

$$R = \frac{z \cdot Z_{Ch}}{x \cdot Z_{Ge} + y \cdot Z_P}$$

Eq. 3-1

where *x*, *y* and *z* are the atomic fractions of germanium, pnictogen and chalcogen. Z_i is coordination number of these constituents (*i.e.* 2, 4 and 3 for Z_{Ch}, Z_{Ge} and Z_P). The chemical threshold when only heteropolar bonds exists, $R = 1$. For R > the system is chalcogen rich and for R < 1 the system is chalcogen poor [94].

3.2. Topological approach

Phillips [95] used the concept of the a mean coordination number *Z* in constraint-counting arguments to explain the glass-forming tendency of certain alloys. The number of constrains for glasses is defined as [96]:

$$N_{con} = \frac{Z}{2} + (2Z - 3)$$

Eq. 3-2

where the first term is arising from bond-stretching and the second term from bond-bending constrains [96]. According this theory, the ideal glass-forming condition occurs when the number of constrains per atom (N_{con}) equals the number of degrees of freedom per atom (N_d), [97]. Furthermore, the glass is rigid (overconstrained) when $N_{con} > N_d$. On the other hand, when $N_{con} < N_d$, the glass is considered to be floppy (underconstrained) [98].

4. Photoinduced effects in amorphous chalcogenides

Photoinduced phenomena in amorphous chalcogenides include a large number of changes initiated or enhanced by light exposure. The exposure to light or other electromagnetic radiation excites electron-hole pairs, which gives rise to the production of structural changes. As a consequence of these light-induced changes in the short-range order and atomic configurations a large variety of physical and chemical properties are altered. These include density, hardness, elastic constants, optical properties, electric transport properties, phase, chemical solubility and reactivity [16, 99-102]. Photostructural transformations are apparently possible due to the existence of both covalent and Van der Waals bonds which make the glass network in chalcogenides flexible and easily rearrangeable with several quasi-stable states [101].

Two basic groups of photoinduced effects are considered, whether the light-induced temperature is determinative or not, *i.e. thermal* or *photon* (*athermal*) effects. At the present, the most well-known thermal effect in chalcogenides is the optical phase change in tellurium-based films firstly described by Ovshinsky's group around 1970 [17, 103]. The essential requirements for a PCM include good thermal stability of amorphous state, rapid phase changes, large optical/electrical changes and a large number of cycles between amorphous and crystalline states [104].

As a breakthrough discovery in phase-change memory (PCM) materials, the pseudo-binary compositions at GeTe–Sb_2Te_3 tie-line also known as GSTs are considered.

Phase-change transition time for GeTe–Sb_2Te_3 pseudo-binary decreases when moving towards Sb_2Te_3 (in the direction from $Ge_2Sb_2Te_5$ to $GeSb_2Te_4$ and further to $GeSb_4Te_7$) approximately from 100 to 30 ns. However, material becomes less stable and the re-crystallization may also occur at room temperature after a certain period of time. Based on a set of properties that were taken into account (including the phase transition time, optical contrast between the amorphous and crystalline state, and melting temperature), the composition $Ge_2Sb_2Te_5$ found its commercial use as an optical phase-change disk, in the three generations of PCM [105-107]; compact disk (CD), digital versatile disk (DVD) and Blu-ray disk (BD). Recently, the reflectivity contrast as high as ~0.21 between amorphous and crystalline state accompanied by large sheet resistance decrease was reported by Bouška *et al.* for pulsed laser deposited GST thin films [108]. Other advances in PCM comes with various technological approaches including three-layered BD with the capacity as high as 100 GB [104] and other solutions combining PCM with polar crystals, metal nanostructures (metamaterials), dielectrics *etc.* [109].

One should distinguish between optical phase change and photo-enhanced crystallization which occurs at the significantly lower temperatures. PHC in amorphous selenium has been studied by several authors since the end of 1960s and was extended to studies on evaporated selenium films in the beginning of 1970s, [110, 111]. Sakai *et al.* proposed that in the photo-enhanced effect, the lone-pair electrons of Se atoms in amorphous $GeSe_2$ be excited by incident photons bearing the energies above the bandgap. The bond switching or atomic rearrangements occurs when the electron relax through an electron-phonon interaction. Therefore, it is considered that the crystallization from amorphous state to crystalline $GeSe_2$ is accelerated due to the light irradiation [112].

Optically and thermally induced diffusion and dissolution (OIDD) of various metals such as Ag (Cu, Zn) into amorphous As–S, As–Se, Ge–Se and Ge–S chalcogenide films is another well-known phenomena. The amount of dissolved Ag ions can exceed even 40 at. % for some systems [113]. The basic principle of optically induced dissolution of Ag in evaporated $As_{33}S_{67}$ is shown in figure 4-1.

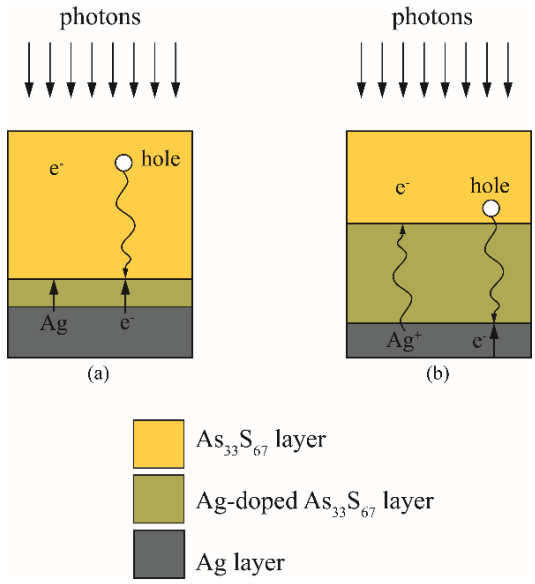

Fig. 4-1 Formation of Ag^+ ions during silver photo-dissolution process. Photo-excited hole and electron motions govern Ag^+ migration – redraw from Wágner *et al.* [114].

According photocalorimetry measurements using high pressure mercury lamp with light intensities between 20 and 500 $mW \cdot cm^{-2}$ at the sample and IR cut-off filters, OIDD includes Ag^+ ion formation, as a part of the chemical reaction $2\ Ag + S \rightarrow Ag_2S$. Ag—S bonds are also created as a part of the solid state reaction $Ag + AsS_2 \rightarrow AgAsS_2$ when the stoichiometric compound or a solid solution with composition of stoichiometric compound is formed [114, 115].

In the early 1970s De Neufville *et al.* reported shift in the optical absorption edge of evaporated As_2Se_3 and As_2S_3 amorphous films (fig. 4-2). As-deposited films undergo irreversible photodarkening when exposed to the bandgap illumination with beam intensity of 100 $mW \cdot cm^{-2}$ in the vacuum (photostructural transformation) or when annealed at $\sim T_g$ in the dry nitrogen flow (thermostructural transformation). The optical effects in these films were accounted for in terms of defect creation and polymerization, respectively. They also reported reversible photodarkening of exposed annealed films which can be considerably restored by consequent annealing process [116].

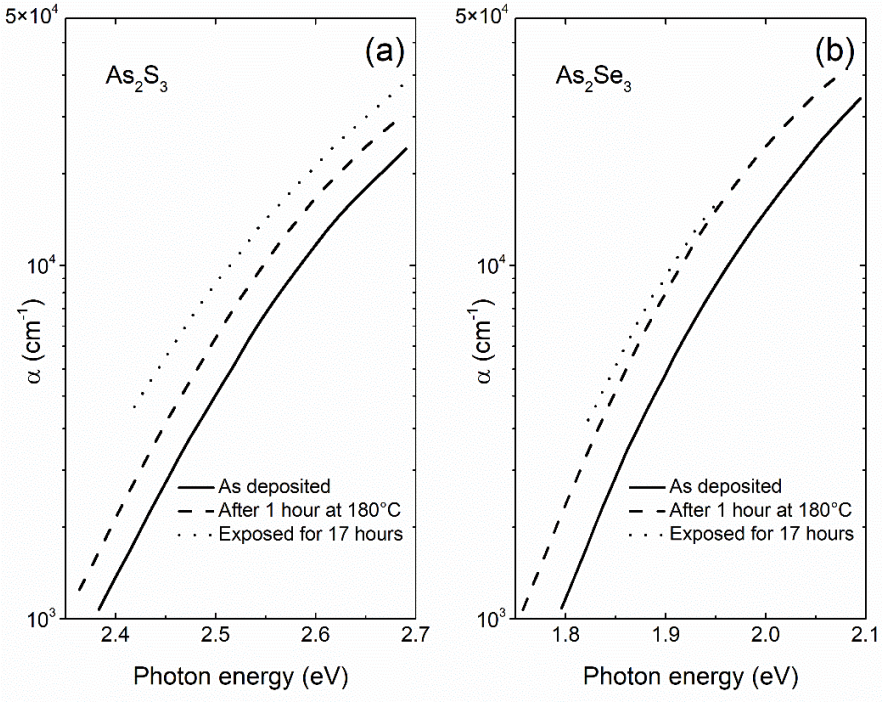

Fig. 4-2 Influence of exposure and annealing on evaporated **(a)** As_2S_3 and **(b)** As_2Se_3 films – digitized data from De Neufville *et al.* [116].

Such restoration process is never complete indicating that two components take place – reversible component – which can be restored by annealing near T_g, and the irreversible one [43]. The irreversible component is believed to be caused by thermal or photopolymerization of as-evaporated film which is formed from numerous vapour species present during evaporation process leading to different spatial structure (irreversible structural changes). For example, in stoichiometric As_2Se_3 films, where the chemical ordering would normally allow the formation of heteropolar As—S bonds only, the presence of homopolar bods (As—As and S—S) is inevitable due to the deviations from the stoichiometry [20]. Moreover, the competition of different bond energies, *e.g.* Ge—Se and Sb—Se in Ge-Sb-Se ternary alloys, makes this problem even more critical [17].

During annealing or illumination homopolar bonds are cleaved and energetically more favorable heteropolar bonds are formed instead. Cleaving of homopolar bonds ("wrong bonds") followed by the formation of heteropolar bonds is believed to be responsible for the photodarkening (PD) of As-based and photobleaching (PB) of Ge-based chalcogenide glasses [26]. Illumination of evaporated $GeSe_2$ under vacuum leads to the PB ascribed to intrinsic structural changes following Ge—Ge + Se—Se $\xrightarrow{\hbar\omega}$ Ge—Se, [117, 118].

Tichý *et al.* have studied the reversible process induced by band-gap illumination in $GeSe_2$ evaporated thin films at the liquid nitrogen temperature. At such low temperatures the atomic mobility is suppressed. At the same time, however, excited states similar to self-trapped excitons (STE) are formed. Low temperature suppresses the photo-excited carrier separation (thermal diffusion is suppressed) making both the density and stability of STE-like centers higher. If illumination at around room temperature is carried out, the separation of photo-excited carriers can be possible and the system can partly relax back to the ground state. Simultaneously, a part of STE-like defects can be converted to more stable random pairs by bond switching. Such processes are responsible for darkening of $GeSe_2$ evaporated films at a liquid nitrogen temperature [119]. Regarding the different behaviour observed between

annealed and as-deposited films whatever the selected PVD method, it can be assumed that a large number of stabilization mechanisms occur during the irradiation of as-deposited films. These include photopolymerization (accompanied by void collapsing), homo-to-heteropolar bond interchange and photoenhanced vaporization on air [17, 43].

Furthermore, PD in amorphous chalcogenides is also usually accompanied by photoinduced volume expansion (photoexpansion or PVE), [20]. Shimakawa *et al.* proposed the model to explain the PD in arsenic-based layered chalcogenides and amorphous selenium [120]. In proposed model, depicted in figure 4-3, photogenerated holes diffuse away to the irradiated region. This causes the repulsive interlayer Coulombic interaction producing an increase in the interlayer distance (volume expansion). Furthermore, a slip motion along the layers is expected to occur. This motion is known to increase the lone-pair interaction between interlayers resulting in PD. Another contribution to PD may be coming from photoinduced defect creation, specifically bond breaking between As and Se [121].

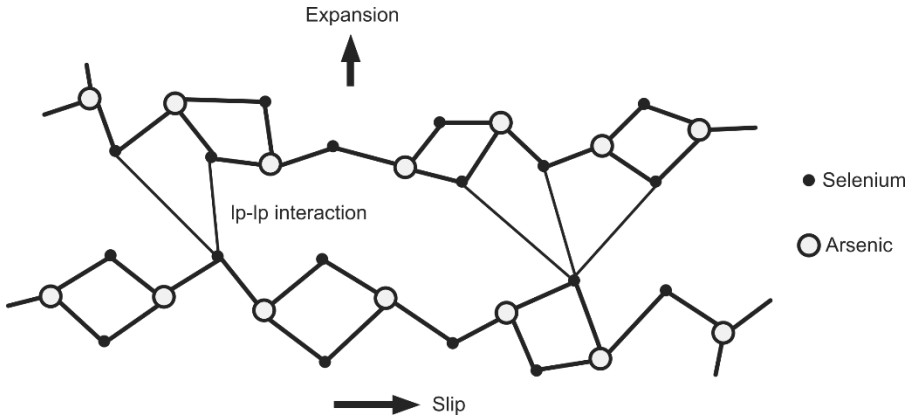

Fig. 4-3 Schematic of interlayer slipping and expansion during the exposure of arsenic-based layered chalcogenide – redraw from Kugler and Shimakawa [121].

For the long time it was believed that PD and PVE in evaporated As_2S_3 films, firstly reported by Hamanaka *et al.*, [122], were two aspects of the same phenomenon. However, this supposition was later refuted by Tanaka [123], who demonstrated that the time constants of these two phenomena are different. It was observed that the evolution of PVE saturates earlier than that of PD, suggesting that these two phenomena are not directly related to each other [121]. The reverse photoinduced volume change (*i.e.* photocontraction) was reported in ternary Ge-As-Se system of various compositions. Calvez *et al.* suggested that both large photocontraction and photoexpansion are result of optically tuning the local structural enthalpy; effectively altering the local glass density in the non-crystalline Ge-As-Se_{13}, [124]. However, general explanation of the microscopic origin of photoinduced volume changes is still speculative and remains open at the present time [125]. Moreover, contribution to PD observed in Se-rich Ge-deficient evaporated Ge_xSe_{100-x} thin films may be originating from photocrystallization of α-selenium in these films [126].

Presence of oxygen and water vapour during the illumination on air or in poor vacuum can lead to light-induced oxidation (photo-oxidation), [116]. Berkes *et al.* referred the growth of small cubic As_2O_3 crystals on the surface of As_2Se_3 and As_2S_3 evaporated films leading to an increase in optical density [127]. Photo-oxidation in germanium based chalcogenides was also studied by many authors [107, 128, 129]. Depending on material, light induced surface oxidation can result in both bleaching or darkening [107]. Infrared absorption spectroscopy is a

suitable method for observing As—O and Ge—O stretching vibrations in arsenic- and germanium-based chalcogenide films, respectively [129, 130].

References

1. Zakery A., Elliott S.R. Optical properties and applications of chalcogenide glasses: a review. *Journal of Non-Crystalline Solids.* 2003;*330:*1-12.
2. Tanaka K., Shimakawa K. Chalcogenide glasses in Japan: A review on photoinduced phenomena. *physica status solidi (b).* 2009;*246:*1744-1757.
3. Sreeram A.N., Varshneya A.K., Swiler D.R. Microhardness and indentation toughness versus average coordination number in isostructural chalcogenide glass systems. *Journal of Non-Crystalline Solids.* 1991;*130:*225-235.
4. Tanaka K. Photoinduced processes in chalcogenide glasses. *Current Opinion in Solid State and Materials Science.* 1996;*1:*567-571.
5. Zallen R., The Physics of Amorphous Solids, Wiley, 2008,
6. Baudet E., Cardinaud C., Girard A., Rinnert E., Michel K., Bureau B., Nazabal V. Structural analysis of RF sputtered Ge-Sb-Se thin films by Raman and X-ray photoelectron spectroscopies. *Journal of Non-Crystalline Solids.* 2016;*444:*64-72.
7. Zakery A., Elliott S.R., Optical nonlinearities in chalcogenide glasses and their applications, Berlin ; New York Springer, 2007,
8. Savage J.A., Nielsen S. Chalcogenide glasses transmitting in the infrared between 1 and 20 μ — a state of the art review. *Infrared Physics.* 1965;*5:*195-204.
9. Baudet E., Sergent M., Němec P., Cardinaud C., Rinnert E., Michel K., Jouany L., Bureau B., Nazabal V. Experimental design approach for deposition optimization of RF sputtered chalcogenide thin films devoted to environmental optical sensors. *Scientific Reports.* 2017;*7:*3500.
10. Xu H., He Y., Wang X., Nie Q., Zhang P., Xu T., Dai S., Zhang X., Tao G. Preparation of Low-loss Ge15Ga10Te75 chalcogenide glass for far-IR optics applications. *Infrared Physics & Technology.* 2014;*65:*77-82.
11. Sanghera J.S., Aggarwal I.D., Shaw L.B., Busse L.E., Thielen P., Nguyen V., Pureza P., Bayya S., Kung F. Applications of Chalcogenide glass optical fibers at NRL. *Journal of Optoelectronics and Advanced materials.* 2001;*3:*627-640.
12. Nazabal V., Jurdyc A.M., Němec P., Brandily-Anne M.L., Petit L., Richardson K., Vinatier P., Bousquet C., Cardinal T., Pechev S., Adam J.L. Amorphous Tm3+ doped sulfide thin films fabricated by sputtering. *Optical Materials.* 2010;*33:*220-226.
13. Schweizer T., Samson B.N., Moore R.C., Hewak D.W., Payne D.N. Rare-earth doped chalcogenide glass fibre laser. *Electronics Letters* (Vol. 33): Institution of Engineering and Technology, 1997, 414-416.
14. Tanaka K. Nonlinear optics in glasses: How can we analyze? *Journal of Physics and Chemistry of Solids.* 2007;*68:*896-900.
15. Ta'eed V.G., Shokooh-Saremi M., Fu L., Littler I.C.M., Moss D.J., Rochette M., Eggleton B.J., Yinlan R., Luther-Davies B. Self-phase modulation-based integrated optical regeneration in chalcogenide waveguides. *IEEE Journal of Selected Topics in Quantum Electronics.* 2006;*12:*360-370.
16. Fritzsche H. The origin of reversible and irreversible photostructural changes in chalcogenide glasses. *Philosophical Magazine Part B.* 1993;*68:*561-572.
17. Tanaka K., Shimakawa K., Amorphous chalcogenide semiconductors and related materials, New York Springer Science+Business Media, 2011,
18. Taylor P.C. The localization of electrons in amorphous semiconductors: A twenty-first century perspective. *Journal of Non-Crystalline Solids.* 2006;*352:*839-850.
19. Mott N. The mobility edge since 1967. *Journal of Physics C: Solid State Physics.* 1987;*20:*3075.

20. Kolobov A.V., Tominaga J., Chalcogenides : metastability and phase change phenomena, Berlin ; New York Springer, 2012,
21. Tanaka K. Have we understood the optical absorption edge in chalcogenide glasses? *Journal of Non-Crystalline Solids.* 2016;*431:*21-24.
22. Fritzsche H. Optical and electrical energy gaps in amorphous semiconductors. *Journal of Non-Crystalline Solids.* 1971;*6:*49-71.
23. Pankove J.I., Optical processes in semiconductors, Englewood Cliffs, N.J., Prentice-Hall, 1971,
24. Tauc J., Amorphous and liquid semiconductors, London, New York, Plenum, 1974,
25. Tanaka K. Minimal Urbach energy in non-crystalline materials. *Journal of Non-Crystalline Solids.* 2014;*389:*35-37.
26. Shimakawa K., Kolobov A., Elliott S.R. Photoinduced effects and metastability in amorphous semiconductors and insulators. *Advances in Physics.* 1995;*44:*475-588.
27. Tichý L., Tichá H., Nagels P., Sleeckx E., Callaerts R. Optical gap and Urbach edge slope in a-Se. *Materials Letters.* 1996;*26:*279-283.
28. Street R.A., Mott N.F. States in the Gap in Glassy Semiconductors. *Physical Review Letters.* 1975;*35:*1293-1296.
29. Mott N.F., Davis E.A., Electronic Processes in Non-Crystalline Materials, OUP Oxford, 2012,
30. Kastner M., Adler D., Fritzsche H. Valence-Alternation Model for Localized Gap States in Lone-Pair Semiconductors. *Physical Review Letters.* 1976;*37:*1504-1507.
31. Kastner M., Fritzsche H. Defect chemistry of lone-pair semiconductors. *Philosophical Magazine B.* 1978;*37:*199-215.
32. Street R.A. Non-radiative recombination in chalcogenide glasses. *Solid State Communications.* 1977;*24:*363-365.
33. Specht M.: Comportement mécanique de films minces de chalcogénures sous irradiation de photons. 2017
34. Swanepoel R. Determination of the thickness and optical constants of amorphous silicon. *Journal of Physics E: Scientific Instruments.* 1983;*16:*1214.
35. Ganjoo A., Golovchak R. Computer program PARAV for calculating optical constants of thin films and bulk materials: Case study of amorphous semiconductors. *Journal of Optoelectronics and Advanced materials.* 2008;*10:*1328-1332.
36. Fujiwara H., Spectroscopic ellipsometry : principles and applications, Chichester, England; Hoboken, NJ John Wiley & Sons, 2007,
37. Singh J., Optical properties of condensed matter and applications, Chichester, England ; Hoboken, NJ John Wiley, 2006,
38. Kasap S.O., Capper P., Springer handbook of electronic and photonic materials, New York Springer, 2006,
39. Wemple S.H., DiDomenico M. Behavior of the Electronic Dielectric Constant in Covalent and Ionic Materials. *Physical Review B.* 1971;*3:*1338-1351.
40. Wemple S.H. Refractive-Index Behavior of Amorphous Semiconductors and Glasses. *Physical Review B.* 1973;*7:*3767-3777.
41. Boyd R.W., Nonlinear optics, Amsterdam ; Boston Academic Press, 2008,
42. Eggleton B.J., Luther-Davies B., Richardson K. Chalcogenide photonics. *Nat Photon.* 2011;*5:*141-148.
43. Adam J.L., Zhang X., Chalcogenide Glasses: Preparation, Properties and Applications, Elsevier Science, 2014,
44. Alfano R.R., Shapiro S.L. Observation of Self-Phase Modulation and Small-Scale Filaments in Crystals and Glasses. *Physical Review Letters.* 1970;*24:*592-594.

45. Dai S., Wang Y., Peng X., Zhang P., Wang X., Xu Y. A Review of Mid-Infrared Supercontinuum Generation in Chalcogenide Glass Fibers. *Applied Sciences.* 2018;*8:*707.
46. Yu Y., Gai X., Ma P., Vu K., Yang Z., Wang R., Choi D.-Y., Madden S., Luther-Davies B. Experimental demonstration of linearly polarized 2 – 10 μm supercontinuum generation in a chalcogenide rib waveguide. *Optics Letters.* 2016;*41:*958-961.
47. Chauvet M., Fanjoux G., Huy K.P., Nazabal V., Charpentier F., Billeton T., Boudebs G., Cathelinaud M., Gorza S.-P. Kerr spatial solitons in chalcogenide waveguides. *Optics Letters.* 2009;*34:*1804-1806.
48. Andriesh A.M., Bertolotti M., Physics and applications of non-crystalline semiconductors in optoelectronics, Dordrecht ; Boston : Kluwer Academic, 1997,
49. Sutherland R.L., Handbook of Nonlinear Optics, Taylor & Francis, 2003,
50. Garmire E. Overview of Nonlinear Optics. In N. Kamanina (ed), *Nonlinear Optics*: InTech, 2003.
51. Wang T., Gai X., Wei W., Wang R., Yang Z., Shen X., Madden S., Luther-Davies B. Systematic z-scan measurements of the third order nonlinearity of chalcogenide glasses. *Optical Materials Express.* 2014;*4:*1011-1022.
52. Nasu H., Ibara Y., Kubodera K.i. Optical third-harmonic generation from some high-index glasses. *Journal of Non-Crystalline Solids.* 1989;*110:*229-234.
53. Chiao R.Y., Garmire E., Townes C.H. Self-Trapping of Optical Beams. *Physical Review Letters.* 1964;*13:*479-482.
54. Sanghera J.S., Shaw L.B., Florea C.M., Pureza P., Nguyen V.Q., Kung F., Gibson D., Aggarwall I.D. Nonlinear Properties of Chalcogenide Glass Fibers. In B. Pal (ed), *Guided Wave Optics and Optoelectronics*: InTech, 2010.
55. Sheik-Bahae M., Said A.A., Wei T.H., Hagan D.J., Stryland E.W.V. Sensitive measurement of optical nonlinearities using a single beam. *IEEE Journal of Quantum Electronics.* 1990;*26:*760-769.
56. Samoc M., Samoc A., Luther-Davies B., Bao Z., Yu L., Hsieh B., Scherf U. Femtosecond Z-scan and degenerate four-wave mixing measurements of real and imaginary parts of the third-order nonlinearity of soluble conjugated polymers. *Journal of the Optical Society of America B.* 1998;*15:*817-825.
57. Boling N., Glass A., Owyoung A. Empirical relationships for predicting nonlinear refractive index changes in optical solids. *IEEE Journal of Quantum Electronics.* 1978;*14:*601-608.
58. Dinu M. Dispersion of phonon-assisted nonresonant third-order nonlinearities. *IEEE Journal of Quantum Electronics.* 2003;*39:*1498-1503.
59. Fournier J., Snitzer E. The nonlinear refractive index of glass. *IEEE Journal of Quantum Electronics.* 1974;*10:*473-475.
60. Garcia H., Avanaki K.N. Direct and indirect two-photon absorption in Ge within the effective mass approximation. *Applied Physics Letters.* 2012;*100:*131105.
61. Garcia H., Kalynamaran R. Phonon-assisted two-photon absorption in the presence of a DC-field: The nonlinear franz-keldysh effect in indirect gap semiconductors. *2006 Conference on Lasers and Electro-Optics and 2006 Quantum Electronics and Laser Science Conference*: 2006.
62. Lenz G., Zimmermann J., Katsufuji T., Lines M.E., Hwang H.Y., Spälter S., Slusher R.E., Cheong S.W., Sanghera J.S., Aggarwal I.D. Large Kerr effect in bulk Se-based chalcogenide glasses. *Optics Letters.* 2000;*25:*254-256.
63. Lines M.E. Bond-orbital theory of linear and nonlinear electronic response in ionic crystals. II. Nonlinear response. *Physical Review B.* 1990;*41:*3383-3390.

64. Sheik-Bahae M., Hagan D.J., Van Stryland E.W. Dispersion and band-gap scaling of the electronic Kerr effect in solids associated with two-photon absorption. *Physical Review Letters.* 1990;*65:*96-99.
65. Tichá H., Tichý L. Semiempirical relation between Non-linear susceptibility (refractive index), Linear refractive index and Optical gap and its Application to Amorphous chalcogenides. *Journal of Optoelectronics and Advanced materials.* 2002;*4:*381-386.
66. Chopra K.L., Bahl S.K. Exponential tail of the optical absorption edge of amorphous semiconductors. *Thin Solid Films.* 1972;*11:*377-388.
67. Hô N., Laniel J.M., Vallée R., Villeneuve A. Photosensitivity of As2S3 chalcogenide thin films at 1.5μm. *Optics Letters.* 2003;*28:*965-967.
68. Miller R.C. Optical second harmonic generation in piezoelectric crystals. *Applied Physics Letters.* 1964;*5:*17-19.
69. Wang C.C. Empirical Relation between the Linear and the Third-Order Nonlinear Optical Susceptibilities. *Physical Review B.* 1970;*2:*2045-2048.
70. Adair R., Chase L.L., Payne S.A. Nonlinear refractive index of optical crystals. *Physical Review B.* 1989;*39:*3337-3350.
71. Sheik-Bahae M., Van Stryland E.W. Chapter 4 - Optical Nonlinearities in the Transparency Region of Bulk Semiconductors. In E. Garmire and A. Kost (eds), *Semiconductors and Semimetals* (Vol. 58): Elsevier, 1998, 257-318.
72. Sheik-Bahae M., Van Stryland E.W. Ultrafast nonlinearities in semiconductor laser amplifiers. *Physical Review B.* 1994;*50:*14171-14178.
73. Sheik-Bahae M. Nonlinear Optics of Bound Electrons in Solids. In J. V. Moloney (ed), *Nonlinear Optical Materials*. New York, NY: Springer New York, 1998, 205-224.
74. Lines M.E. Oxide glasses for fast photonic switching: A comparative study. *Journal of Applied Physics.* 1991;*69:*6876-6884.
75. Wynne J.J. Optical Third-Order Mixing in GaAs, Ge, Si, and InAs. *Physical Review.* 1969;*178:*1295-1303.
76. Strizik L., Yannopoulos S.N., Benekou V., Oswald J., Pavlista M., Prokop V., Wagner T., Orava J. Photoluminescence in pulsed-laser deposited GeGaSbS:Er films. *Optical Materials.* 2018;*85:*246-253.
77. Todorov R., Tasseva J., Babeva T. Thin Chalcogenide Films for Photonic Applications. In A. Massaro (ed), *Photonic Crystals*: IntechOpen, 2012.
78. Stegeman G.I., Segev M. Optical Spatial Solitons and Their Interactions: Universality and Diversity. *Science.* 1999;*286:*1518-1523.
79. Chen Z., Segev M., N. Christodoulides D. Optical spatial solitons: historical overview and recent advances. *Reports on Progress in Physics.* 2012;*75:*086401.
80. Luther-Davies B., Stegeman G.I. Materials for Spatial Solitons. In S. Trillo and W. Torruellas (eds), *Spatial Solitons*. Berlin, Heidelberg: Springer Berlin Heidelberg, 2001, 19-35.
81. Hachiya K. Density functional electronic structures calculations of GeSe2. *Journal of Non-Crystalline Solids.* 2001;*291:*160-166.
82. Barnes W.L., Dereux A., Ebbesen T.W. Surface plasmon subwavelength optics. *Nature.* 2003;*424:*824-830.
83. Shynkarenko O., Kravchenko S. Surface Plasmon Resonance Sensors: Methods of Surface Functionalization and Sensitivity Enhancement. *Theoretical & Experimental Chemistry.* 2015;*51:*273-292.
84. Quail J.C., Simon H.J. Second-harmonic generation with phase-matched long-range and short-range surface plasmons. *Journal of Applied Physics.* 1984;*56:*2589-2591.
85. Ariyasu J., Seaton C.T., Stegeman G.I. Nonlinear surface polaritons guided by metal films. *Journal of Applied Physics.* 1985;*58:*2460-2466.

86. Walasik W., Renversez G., Kartashov Y.V. Stationary plasmon-soliton waves in metal-dielectric nonlinear planar structures: Modeling and properties. *Physical Review A.* 2014;*89:*023816.
87. Walasik W., Kartashov Y., Nicolet A., Gilles R. 1D model for low power soliton hybridized with a plasmon in realistic nonlinear planar structures. *AIP Conference Proceedings.* 2012;*1475:*179-181.
88. Walasik W., Nazabal V., Chauvet M., Kartashov Y., Renversez G. Low-power plasmon-soliton in realistic nonlinear planar structures. *Optics Letters.* 2012;*37:*4579-4581.
89. Kuriakose T., Halenkovic T., Elsawy M.M.R., Nemec P., Nazabal V., Renversez G., Chauvet M. Experimental demonstration of soliton-plasmon coupling in planar waveguides (Conference Presentation). *SPIE Photonics Europe*: 2018.
90. Ovshinsky S.R., Adler D. Local structure, bonding, and electronic properties of covalent amorphous semiconductors. *Contemporary Physics.* 1978;*19:*109-126.
91. Lecomte A., Nazabal V., Le Coq D., Calvez L. Ge-free chalcogenide glasses based on Ga-Sb-Se and their stabilization by iodine incorporation. *Journal of Non-Crystalline Solids.* 2018;*481:*543-547.
92. Mao A.W., Aitken B.G., Youngman R.E., Kaseman D.C., Sen S. Structure of Glasses in the Pseudobinary System Ga2Se3–GeSe2: Violation of Chemical Order and 8-N Coordination Rule. *The Journal of Physical Chemistry B.* 2013;*117:*16594-16601.
93. Micoulaut M., Kachmar A., Bauchy M., Roux S., Massobrio C., Boero M., Structure, topology, rings, and vibrational and electronic properties of GexSe1-x glasses across the rigidity transition: A numerical study, 2013,
94. Tichý L., Tichá H. On the chemical threshold in chalcogenide glasses. *Materials Letters.* 1994;*21:*313-319.
95. Phillips J.C. Topology of covalent non-crystalline solids I: Short-range order in chalcogenide alloys. *Journal of Non-Crystalline Solids.* 1979;*34:*153-181.
96. Farid A.M., Fouad S.S., Ammar A.H. The structural properties of GexSb40−x Se60 system. *Journal of Materials Science: Materials in Electronics.* 2005;*16:*97-101.
97. Phillips J.C. Topology of covalent non-crystalline solids II: Medium-range order in chalcogenide alloys and A-Si(Ge). *Journal of Non-Crystalline Solids.* 1981;*43:*37-77.
98. Phillips J.C., Thorpe M.F. Constraint theory, vector percolation and glass formation. *Solid State Communications.* 1985;*53:*699-702.
99. Fritzsche H. Photo-induced fluidity of chalcogenide glasses. *Solid State Communications.* 1996;*99:*153-155.
100. Keneman S.A. Surface relief holograms in evaporated arsenic trisulfide films. *Thin Solid Films.* 1974;*21:*281-285.
101. Kolomiets B.T., Lyubin V.M. Reversible photoinduced changes in the properties of chalcogenide vitreous semiconductors. *Materials Research Bulletin.* 1978;*13:*1343-1350.
102. Tanaka K. Reversible photostructural change: Mechanisms, properties and applications. *Journal of Non-Crystalline Solids.* 1980;*35:*1023-1034.
103. Popescu M., Non-crystalline chalcogenides, Dordrecht ; Boston Kluwer Academic Publishers, 2000,
104. Yamada N. Origin, secret, and application of the ideal phase-change material GeSbTe. *physica status solidi (b).* 2012;*249:*1837-1842.
105. Kozyukhin S.A., Sherchenkov A.A., Novotortsev V.M., Timoshenkov S.P. Phase-change-memory materials based on system chalcogenides and their application in phase-change random-access memory. *Nanotechnologies in Russia.* 2011;*6:*227-236.
106. Meinders E.R., Optical data storage : phase-change media and recording, Dordrecht Springer, 2006,

107. Spence C.A., Elliott S.R. Light-induced oxidation and band-edge shifts in thermally evaporated films of germanium chalcogenide glasses. *Physical Review B.* 1989;*39:*5452-5463.
108. Bouška M., Pechev S., Simon Q., Boidin R., Nazabal V., Gutwirth J., Baudet E., Němec P. Pulsed laser deposited GeTe-rich GeTe-Sb2Te3 thin films. *Scientific Reports.* 2016;*6:*26552.
109. Wuttig M., Bhaskaran H., Taubner T. Phase-change materials for non-volatile photonic applications. *Nature Photonics.* 2017;*11:*465.
110. Clement R., Carballes J.C., de Cremoux B. The photo-crystallization of amorphous selenium thin films. *Journal of Non-Crystalline Solids.* 1974;*15:*505-516.
111. Dresner J., Stringfellow G.B. Electronic processes in the photo-crystallization of vitreous selenium. *Journal of Physics and Chemistry of Solids.* 1968;*29:*303-311.
112. Sakai K., Maeda K., Yokoyama H., Ikari T. Photo-enhanced crystallization by laser irradiation and thermal annealing in amorphous GeSe2. *Journal of Non-Crystalline Solids.* 2003;*320:*223-230.
113. Frumar M., Wagner T. Ag doped chalcogenide glasses and their applications. *Current Opinion in Solid State and Materials Science.* 2003;*7:*117-126.
114. Wágner T., Munzar M., Krbal M., Kasap S.O. Photocalorimetric measurement of the heat flow during optically and thermally induced solid state reaction between Ag and As33S67 thin films. *Thermochimica Acta.* 2005;*432:*241-245.
115. Wágner T., Macková A., Peřina V., Rauhala E., Seppälä A., Kasap S.O., Frumar M., Vlček M., Vlček M. The study of photo- and thermally-induced diffusion and dissolution of Ag in As30S70 amorphous films and its reaction products. *Journal of Non-Crystalline Solids.* 2002;*299–302, Part 2:*1028-1032.
116. De Neufville J.P., Moss S.C., Ovshinsky S.R. Photostructural transformations in amorphous As2Se3 and As2S3 films. *Journal of Non-Crystalline Solids.* 1974;*13:*191-223.
117. Lyubin V., Klebanov M., Bruner A., Shitrit N., Sfez B. Transient photodarkening and photobleaching in glassy GeSe2 films. *Optical Materials.* 2011;*33:*949-952.
118. Yan Q., Jain H., Ren J., Zhao D., Chen G. Effect of Photo-Oxidation on Photobleaching of GeSe2 and Ge2Se3 Films. *The Journal of Physical Chemistry C.* 2011;*115:*21390-21395.
119. Tichý L., Sleeckx E., Nagels P., Tichá H. The influence of temperature on the optical absorption edge shift induced by band-gap illumination in thin amorphous GeSe2 films. *Philosophical Magazine Part B.* 1996;*73:*213-221.
120. Shimakawa K., Yoshida N., Ganjoo A., Kuzukawa Y., Singh J. A model for the photostructural changes in amorphous chalcogenides. *Philosophical Magazine Letters.* 1998;*77:*153-158.
121. Kugler S., Shimakawa K., Amorphous semiconductors, 2015,
122. Hamanaka H., Tanaka K., Matsuda A., Iizima S. Reversible photo-induced volume changes in evaporated As2S3 and As4Se5Ge1 films. *Solid State Communications.* 1976;*19:*499-501.
123. Tanaka K. Photoexpansion in As2S3 glass. *Physical Review B.* 1998;*57:*5163-5167.
124. Calvez L., Yang Z., Lucas P. Reversible giant photocontraction in chalcogenide glass. *Optics Express.* 2009;*17:*18581-18589.
125. Němec P., Nazabal V., Frumar M. Photoinduced phenomena in amorphous As4Se3 pulsed laser deposited thin films studied by spectroscopic ellipsometry. *Journal of Applied Physics.* 2009;*106:*023509.
126. Kumar R.R., Barik A.R., Vinod E.M., Bapna M., Sangunni K.S., Adarsh K.V. Crossover from photodarkening to photobleaching in a-GexSe100-x thin films. *Optics Letters.* 2013;*38:*1682-1684.
127. Berkes J.S., Ing S.W., Hillegas W.J. Photodecomposition of Amorphous As2Se3 and As2S3. *Journal of Applied Physics.* 1971;*42:*4908-4916.

128. Tanaka K., Kasanuki Y., Odajima A. Physical properties and photoinduced changes of amorphous Ge-S films. *Thin Solid Films.* 1984;*117:*251-260.
129. Tichý L., Tichá H., Handlíř K., Jurek K. Photoinduced bleaching of Ge35S65 amorphous film. *Journal of Non-Crystalline Solids.* 1988;*101:*223-226.
130. Tichý L., Tichá H., Handlír K. Photoinduced changes of optical properties of amorphous chalcogenide films at ambient air pressure. *Journal of Non-Crystalline Solids.* 1987;*97–98, Part 2:*1227-1230.

Chapter II

Experimental procedures

1. Synthesis of selenide glasses by melt-quenching technique

All the silica tubes used for the purification and the synthesis of chalcogenide glasses are first cleaned (etched) using the hydrofluoric acid. After the etching they are rinsed by tap water and deionized water. The tube is then dried under the vacuum when installed to the experimental set-up. All the elements of high purity (5-6 N) are weighted, typically in the glovebox and introduced into the dried silica tube.

1.1. Purification of selenium

Purification of selenium is performed in order to minimize the impurity content in the synthesized glass (Se–H and Se–O coming from SeO_2). Commercial selenium of initial purity about 5 N is introduced into the silica tube (fig. 1-1) under dynamic vacuum. The set-up is about 20 hours under vacuum provided by turbomolecular pump (~10^{-5} mbar). After this, the selenium is heated to 300 °C for 6 hours to eliminate the majority of impurities.

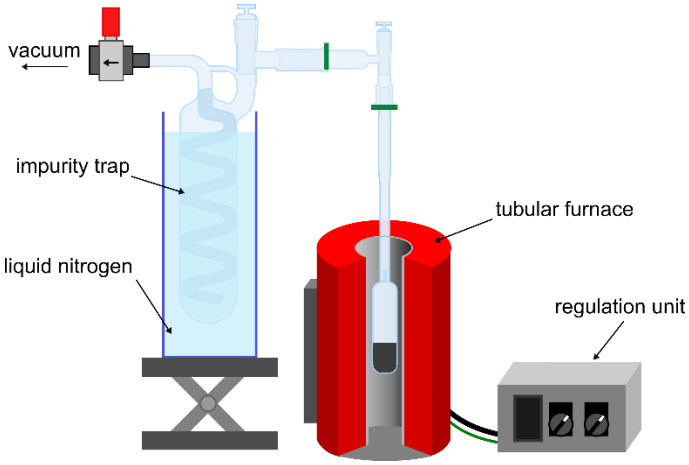

Fig. 1-1 Selenium purification set-up.

Purification of tellurium is performed in double batch assembly silica tube. Tellurium, placed in the first batch, is heated to 530 °C and distilled into the second batch.

1.2. Synthesis of selenide glasses

The synthesis of Ge-Sb-Se chalcogenide glasses is performed in evacuated silica tube in order to prevent the oxidation of used chemical elements. Such experimental set-up is shown in the figure 1-2. Here, the selenium is introduced in the part with the filter while the other elements (antimony and germanium) in the bottom part of silica tube. The set-up is evacuated down to ~10^{-5} mbar of pressure during the night (~15 hours). After this time is elapsed, the silica tube is sealed and prepared for the static distillation of selenium (fig. 1-3). In the case of Ge-Sb-Se-Te system, tellurium is introduced in the part with the filter together with selenium.

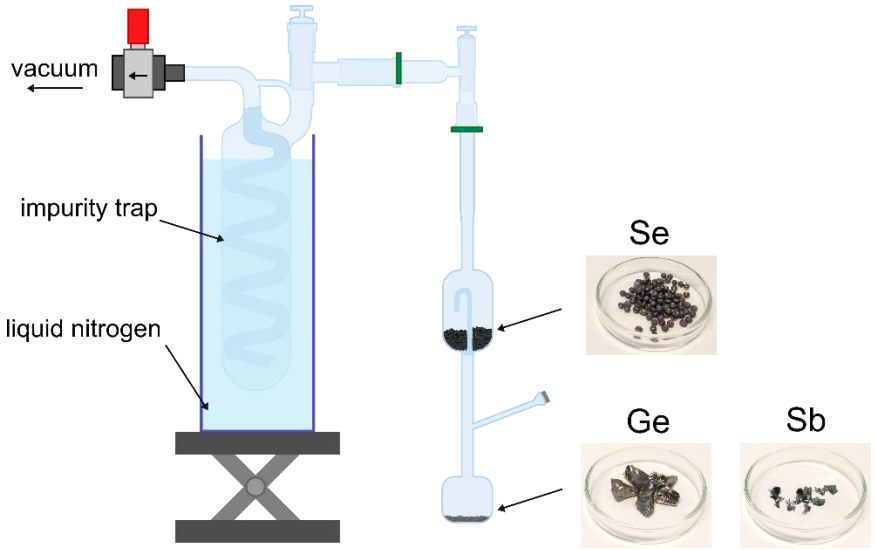

Fig. 1-2 Set-up for synthesis of Ge-Sb-Se target.

In the process of static distillation of selenium, the selenium vapours condensate from the hot part of the silica tube, which is heated up to 750 °C for two hours in the cold part of silica tube containing the other elements.

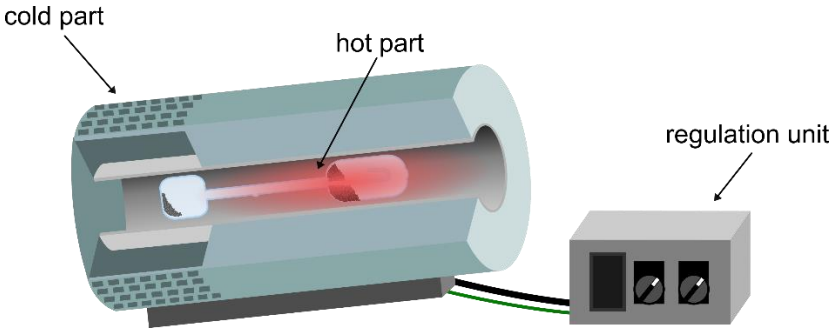

Fig. 1-3 Distillation furnace.

After the static distillation the bottom of the silica tube is sealed and prepared for the synthesis of chalcogenide glass by conventional melt-quenching technique. The elements are melted and homogenized in the rocking furnace at the temperature of 850 °C. Thereafter, the glass is annealed for 6 hours at the temperature just below the glass transition temperature (Tg − 10 °C) for its relaxation. The glass is then cut by diamond wire saw (fig. 1-4a) and polished by multistage polishing onto targets with the thickness of 3.5 mm until the fine ‘mirror-like’ surface is achieved (fig. 1-4b).

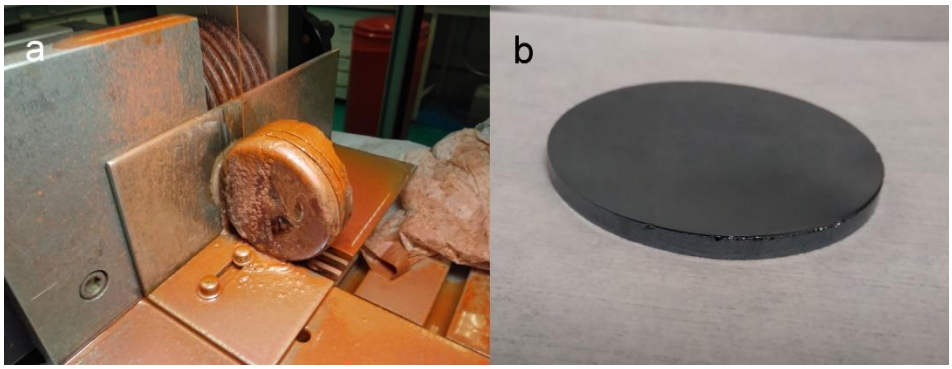

Fig. 1-4 (a) Cutting process by diamond wire saw. **(b)** Fine polished Ge-Sb-Se sputtering target of 50 mm diameter.

2. Fabrication of thin films

Various physical vapour deposition (PVD) techniques were showed to be suitable for the fabrication of chalcogenide amorphous thin films. Thermal evaporation is usually considered as the most accessible PVD technique. In this technique, the bulk material, which is usually prepared by conventional melt-quenching technique (if glass), is placed into the boat or crucible and heated (resistive heating) in the vacuum. This technique is suitable for chalcogenide glasses, because of their low melting points. Produced melts are evaporated and vapour is collected on a substrate, forming the thin film. However, the glasses containing the constituents with much different melting temperatures and/or vapour pressures, may result in film having the composition different from that of bulk source varying throughout its thickness. This problem can be solved using modified method called flash evaporation. In this method, a fine powder of the starting material is dropped in small quantities onto very hot filament. Pieces of the powder "burst" and the material is transferred onto the substrate whereby the composition of the starting material is well preserved [1].

Pulsed laser deposition (PLD) uses relatively high energy fluency laser beam to eject (ablate) particles from the surface of an absorbing target. Typical lasers for the fabrication of thin films by PLD are KrF excimer laser (λ=248 nm) and Nd:YAG laser (λ=532 nm). PLD enables stoichiometric transfer of target material towards the substrate. It is also relatively easy-control [2]. Disadvantage of the PLD is difficulty in preparing thin films of larger areas with homogenous thickness [3]. This may be particularly solved by off-axis geometry.

Another deposition techniques can be used for the fabrication of amorphous thin films, such as spin-coating [4] or chemical vapour deposition (CVD), radio-frequency (RF) magnetron sputtering and co-sputtering, *etc.* Both RF magnetron sputtering and co-sputtering are discussed in following section.

2.1. RF sputtering

In the sputtering deposition, atoms are ejected from the surface of a target made of the appropriate material by collisions with energetic ions and the substrate exposed to the ejected material. This results in deposition of a film with the composition of the target material. Most sputtering is done by noble gas ions because of their non-reactivity (typically argon, because of its intermediate mass), however the reactive gas such as oxygen can be used (reactive sputtering). The most common method is to ignite plasma of the sputtering gas and electrostatically accelerate positive ions from the plasma onto the target by biasing the target at a negative potential. In the sputtering process, a positive Ar ion hits the target, normally removing electrons from it and reflecting as a neutral atom. It can also generate secondary electrons that leave the surface and move into the plasma. However, this is true only if the target has a high enough conductivity, so the electrons can move to the surface to replace those that are removed by sputtering. Insulating materials, such as chalcogenides, do not satisfy this requirement. Thus, sputtering from insulators can be achieved by using an oscillatory target voltage. In this way, a burst of atoms or molecules is sputtered each time the voltage goes negative and the resulting surface charge is neutralized in the subsequent positive swing. Since only 100 ns burst is obtained for each cycle of the target voltage, a high frequency is needed to obtain sufficient rates, typically RF of 13.56 MHz as it is frequency set aside by international agreement for use in industrial process that take place without completely shielding against RF emissions [5]. A typical RF sputtering system is shown in the figure 2-1 (a).

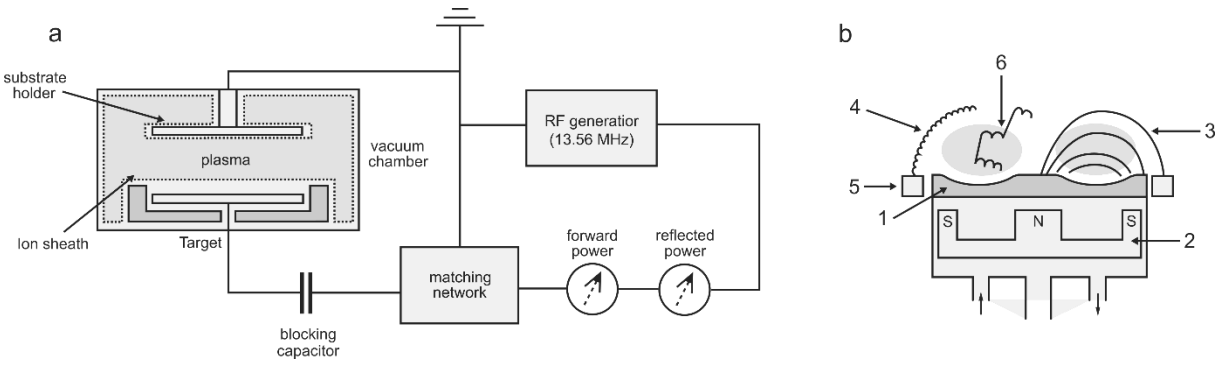

Fig. 2-1 (a) RF sputtering system. The power circuit and matching network deliver electrical power to the target. Forward and reflected power meters monitor the phase matching of the RF generator to the load. – Redraw from Keavney and Falco [5]. **(b)** Planar magnetron target assembly. (1) Eroded target due to the intense plasma, (2) magnets providing (3) magnetic field lines, (4) low energy electrons reaching the anode (5) along magnetic field lines. High energy electrons cross field lines by collision with gas atoms (6). – redraw from Westwood [6].

To deliver the RF power to the target, an impedance matching network must be used. Otherwise, the load may be out of phase with the power supply reducing the efficiency of power transfer to the target. This matching network is usually variable, to allow the compensation for different target materials that might introduce different phase shifts and for fine tuning the power transmitted to the load [5]. The sputtering rate is usually increased by enhanced ionization of gas atoms in the plasma. If the electrons in the plasma are made to move in a spiral path rather than a straight line, the probability of collision of electrons and the gas atoms increases. Such motion of electrons and entrapment of secondary electrons close to the target can be achieved by controlling the magnetic field just above the target. **E×B** drift (where *E* is the electric field perpendicular to the magnetic field *B*) makes electrons move in a direction perpendicular to these fields. In the case of circular planar magnetron (fig. 2-1b), the E×B drift path takes the shape of a closed ring, which is the path of the motion of secondary electrons. After a substantial degree of sputtering, the cross-product leaves a concentric erosion groove on the sputtered face of the target [7].

2.1.1. Co-sputtering

Sputtering employing multiple cathodes (co-sputtering) brings the advantage of adjustable electrical power ratio applied on individual cathodes which enables to obtain thin films with various compositions. This makes co-sputtering cost-effective for compositional dependencies' studies of materials' properties. The schematic representation of three cathode geometry co-sputtering is shown in the figure 2-2.

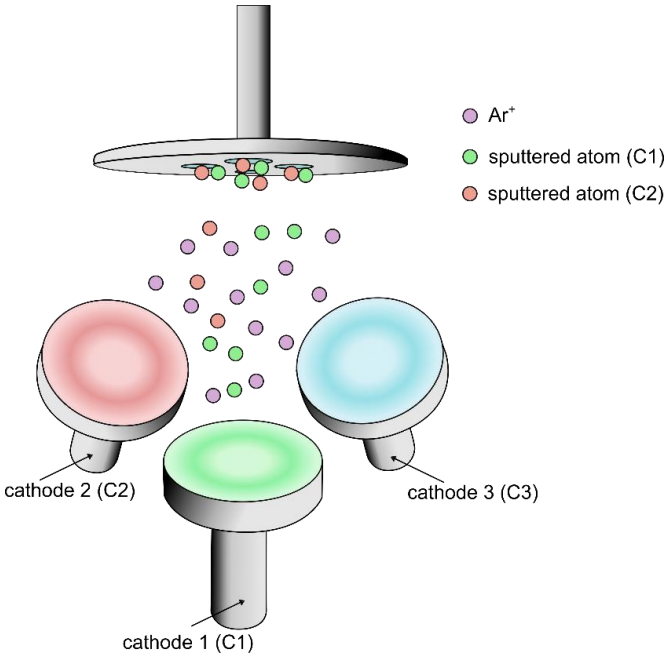

Fig. 2-2 Schematic representation of three-cathode geometry of co-sputtering technique with electrical power applied on two cathodes (C1 + C2).

In spite of obvious advantages of co-sputtering, this is not commonly used technique for amorphous chalcogenide thin films fabrication. Recently, RF magnetron co-sputtering technique was used for the compositional dependencies studies of various properties of chalcogenide amorphous thin films. Lin *et al.* studied photo-induced structural changes in co-sputtered Ge-Sb-Se films using $GeSe_2$ and Sb sputtering targets [8]. Photo-induced effects in the same system (however with higher selenium content) were studied by Halenkovič *et al*. In their work, they used targets with compositions $GeSe_2$, Sb_2Se_3 and $Ge_{28}Sb_{12}Se_{60}$ [9]. Compositional dependence of crystallization and structural stability in Se-poor co-sputtered Ge-Sb-Se films from $Ge_{20}Sb_{15}Se_{65}$ (or $Ge_{28}Sb_{12}Se_{60}$) and Sb(Ge) targets were studied by Wang *et al.* [10]. Optical properties of In-Ge-Se thin films co-sputtered from $GeSe_2$ and In targets were studied by Chen *et al.* [11].

Co-sputtering was also used for the studies of phase-change kinetics of amorphous $Ge_2Sb_2Te_5$ (GST). Cho *et al.* used co-sputtering technique for "doping" of GSTs by bismuth and aluminium using GST and $Ge_2Bi_2Te_5$ (or Al) targets [12]. Phase-change transition characteristics of bismuth and tin "doped" GST thin films for phase-change random access memory were studied by Park *et al.* [13]. In their work GST, Bi and Sn targets were employed.

2.1.2. Thin film morphology

Thin film morphology depending on process variables is often described by Structure Zone Model (SZM) depicted in the figure 2-3 [14]. Here the deposition process variables are the reduced temperature T/T_M (where T is the substrate temperature and T_M is the melting point of the bulk material) and the argon pressure in the PVD chamber which is directly related to the ion bombardment energy. In more recent version of SZM proposed by Messier [15], five zones corresponding to different film morphology depending on deposition process variables are found. Zone 1, which corresponds to porous morphology, is characterized by tapered columns separated by voids. Zone T, also called transition morphology, has no long-range structure beyond the nanometer length-scale. The "matchstick" morphology, depicted as zone M, has

parallel columns with domed tops. Zone 2 corresponds to columnar crystalline grain structure and the zone 3 to recrystallized crystalline grain structure respectively [15].

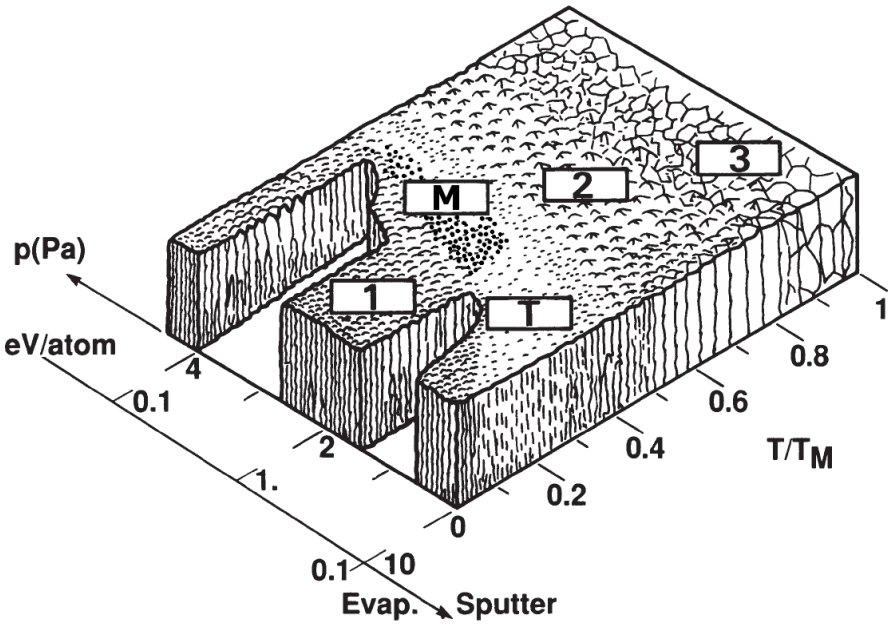

Fig. 2-3 Structure Zone Model for columnar thin films – redraw according adapted version of Thornton [14] in Messier [15].

3. Characterization of chalcogenide glasses and thin films

3.1. Density measurement

Buoyancy method is a simple technique for determination of density of non-porous solids based on the Archimedes' principle. The solid is first weighed in air (m_A) and then again (m_B) in reference liquid (*e.g.* ethanol). The density of solid ρ is then obtained according:

$$\rho = \frac{m_A}{m_A - m_B} \times \rho_0$$

Eq. 3-1

where the ρ_0 stands for the density of the reference liquid. During the experiment, the temperature of the reference liquid must be taken into account.

3.2. Differential scanning calorimetry (DSC)

In DSC, the sample of interest in an aluminium pan is heated together with an empty reference pan at a certain heating rate (typically dT/dt = 10 °C min^{-1}). The heat flow to a sample (dHt/dt) compared to that of the empty reference pan is recorded. The total heat flow rate is given by:

$$\frac{dH_t}{dt} = C_p^{kin} \frac{dT}{dt}$$

Eq. 3-2

where C_p^{kin} represents the kinetic specific heat of the sample [16]. The typical DSC curve of a chalcogenide glass is shown in figure 3-1.

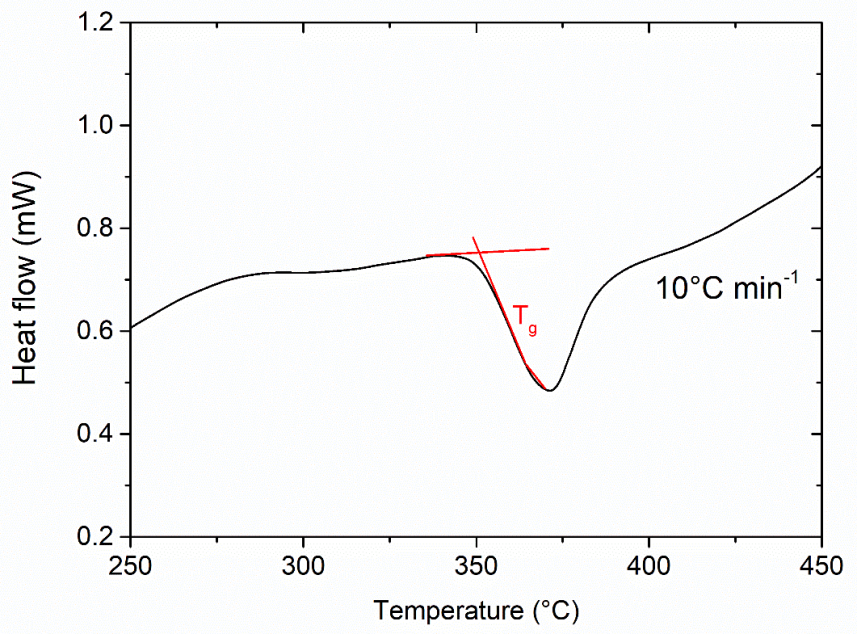

Fig. 3-1 The DSC curve of $Ge_{30.7}Sb_{3.2}Se_{66.1}$ chalcogenide glass at the heating rate of 10°C min^{-1} with indication of T_g determination.

3.3. Scanning electron microscopy

In the SEM, the beam of electrons produced by electron gun is focused (in vacuum) in a form of fine probe, that is rastered over the surface of the specimen [17]. The primary electrons leaving the electron gun are accelerated by voltage between 1 – 30 kV and demagnified by a set of two condense lenses. Subsequently a set of scanning coils forces the electron beam to rapidly scan over an area of the specimen while the magnetic lenses focus the beam on the sample [18]. As the electrons penetrate the surface, several phenomena may occur including the emission of electrons or photons from (or through) the surface [19].

The images produced in the SEM are of three types: secondary electron (SE) images, backscattered electron (BSE) images and elemental X-ray maps. SE and BSE are conventionally separated according their energies. When the high-energy primary electron interacts with an atom, it undergoes either inelastic scattering with atomic electrons or elastic scattering with its nucleus. In an inelastic collision, some amount of the energy is transferred to the other electron. If this energy exceeds the work function of the electron, the emitted electron can exit the solid (the energy of emitted electron is less than 50 eV). Most of the emitted SE are produced within the surface and subsurface of the material (down to 30 nm) [17, 18]. BSE are high energy electrons that have been scattered by the atomic nucleus without loss of their kinetic energy (*i.e.* elastically scattered). They are considered having energy greater than 50 eV. The higher the atomic number of a material, the more likely it is that backscattering occur. Thus, the signal due to the backscattering increases as the Z increases [17].

3.3.1. Energy-dispersive X-ray Spectroscopy (EDS)

When the high-energy radiation of the electron beam interacts with the material, it removes the inner shell electron (ionization). To return the ionized atom to its ground state, an electron from the outer shell (higher energy electron) fills the vacant inner shell, releasing the potential energy difference between the two shells. This excess energy is unique for every atomic transition and may be emitted in the form of X-ray photons or self-absorbed and emitted as an Auger electron (fig. 3-2a). An example can be given, considering the ionized electron from the K shell which is replaced by an electron from the L shell. The excess energy is emitted as the characteristic X-ray labelled as $K\alpha_1$. The hole created in the L shell will be filled by an electron from a higher shell (M shell), if one exists. This M–L transition may result in the emission of another X-ray labelled according to one of the many M–L transitions possible. Such cascade of transitions will continue until the last shell is reached (fig. 3-2b), [20].

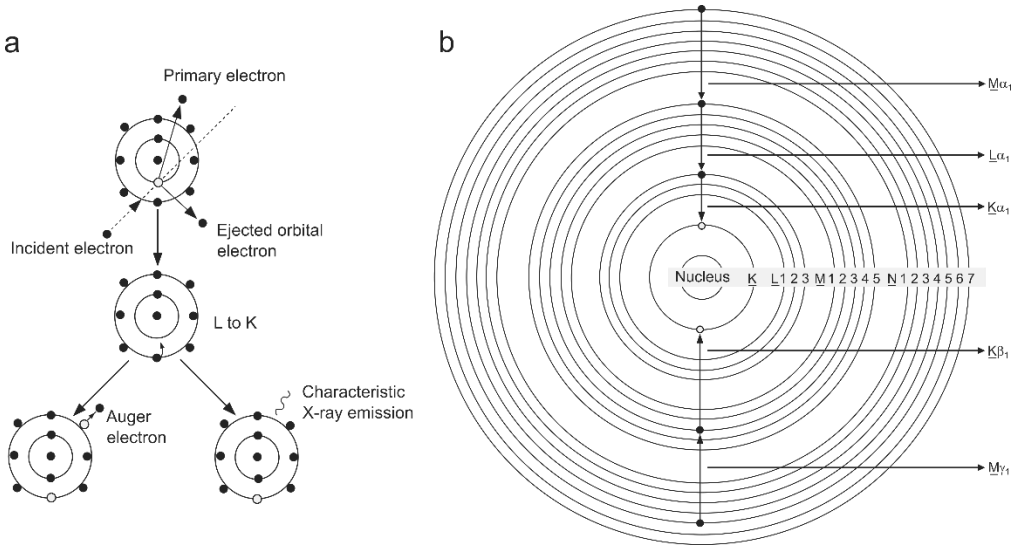

Fig. 3-2 (a) Inner shell electron ionization in an atom and subsequent de-excitation by electron transitions. The excess of energy from an electron transition is expressed either as the ejection of an energetic electron with characteristic energy (Auger process) or by the emission of a characteristic X-ray photon – redraw from Goldstein *et al.*, [21] **(b)** Typical series of electron transitions that may follow the *K*-shell vacancy – redraw from Bertin [22].

3.4. X-ray diffraction (XRD) analysis

XRD analysis is a technique used for the detection and identification of crystalline phases in the material.

When the electromagnetic radiation with the wavelength (λ) comparable with the atomic spacing of the crystal, i.e. $\lambda \sim 0.1$ nm, interacts with the material, it undergoes the diffraction of the incident wave. Therefore, X-rays will be diffracted by the crystalline solids (fig. 3-3). Mathematically, the diffraction can be expressed by means of Bragg's law of diffraction:

$$2d\ sin\theta = n\lambda$$

Eq. 3-3

where d is the interplanar spacing of a particular set of planes, θ is the angle between the incident (or diffracted) ray and the relevant crystal planes and n is an integer, referred to as the order of diffraction (often unity) [18].

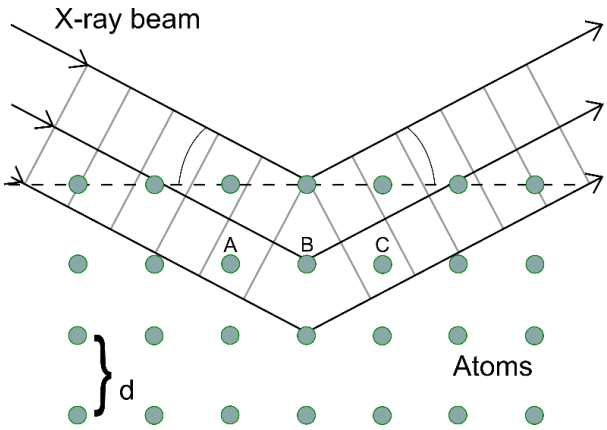

Fig. 3-3 Schematic diagram showing the Bragg's law concept – redraw from Ashby *et al.*, [18].

In the typical XRD experiment, the diffracted intensity is measured as a function of 2θ and the orientation of the specimen, which yields the diffraction pattern [23].

3.5. Ellipsometry

3.5.1. Polarization of light

Polarization of light describes the shape of electric field propagating through the space and time by means of superposition of two orthogonal plane waves. These are one parallel, the other perpendicular to the plane of incidence. Both waves are characterized by their amplitude and the phase. There are three types of polarization of light. First is linearly polarized light, when the phase difference of the waves with arbitrary amplitude is 0° or 180°. Circularly polarized light comprises of two waves with the equal amplitudes and the phase difference of ±90°. Finally, the superposition of two orthogonal plane waves with both arbitrary phase and amplitude results in elliptically polarized light.

3.5.2. Spectroscopic ellipsometry

As shown in figure 3-4 ellipsometry is based on the measurement of the change of the polarization of the light as it interacts with the sample. Electric field is being described by its two components E_p (parallel to the plane of incidence) and E_s (perpendicular to the plane of incidence).

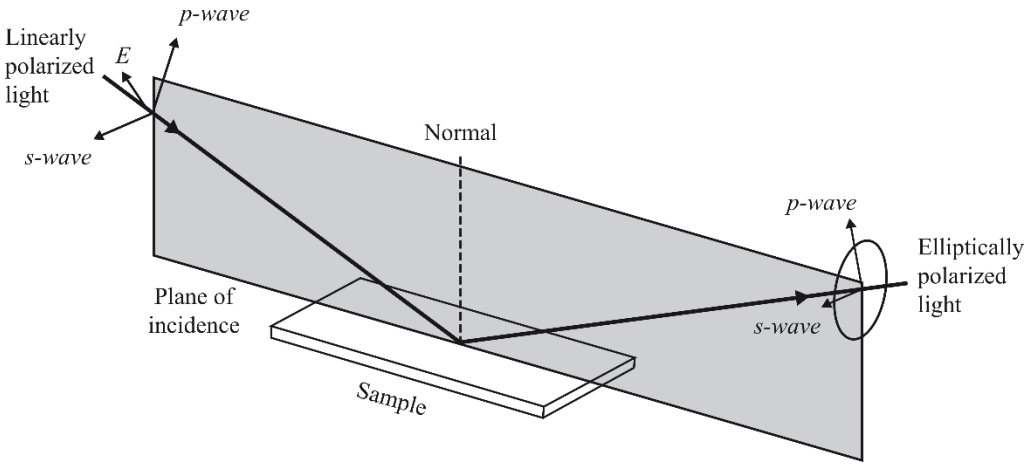

Fig. 3-4 Reflection of linearly polarized light – redraw from Zheng *et al.*, [24].

Ellipsometry determines the complex ratio of output/input electric fields:

$$\rho = \tan(\psi)e^{i\Delta} = \frac{E_p^{out}/E_p^{in}}{E_s^{out}/E_s^{in}} = \frac{|r_p|}{|r_s|}e^{i(\delta_p - \delta_s)}$$

Eq. 3-4

where r_p and r_s are Fresnel reflection coefficients while angles ψ and Δ are so called ellipsometric parameters. The ratio of the modulus of the amplitude reflection coefficients is given by tan ψ. The phase difference between p- and s-polarized reflected light is given by Δ. Two ellipsometric parameters, ψ and Δ, are directly obtained from ellipsometry measurement [24]. Spectroscopic ellipsometry is a very sensitive technique which is routinely used to measure thickness and optical constants of dielectric, semiconductor and metal thin films. It enables the evaluation of the complex dielectric function, $\varepsilon = \varepsilon_1 + i\,\varepsilon_2$, which is related to the refractive index, n, and extinction coefficient, k, $\varepsilon = (n+ik)^2$, through ψ and Δ. The determination of complex dielectric function enables the investigation of the electronic structure of material, which is related to the joint density of states for interband absorption [25].

3.5.3. Modelling and data fitting

Ellipsometry is a non-direct technique which uses fitting of the proper model applied on the measured data. However, its sensitivity is very high since one obtains two simultaneously measured parameters (ψ and Δ). Furthermore, spectroscopic ellipsometry at higher energies (UV-Vis) is very sensitive to surface roughness. The transparent region of amorphous thin films and glasses is often described by normal dispersion (the light with higher wavelengths travels faster through the medium and *vice versa*). Two models for normal dispersion might be used for fitting the refractive index in this region, namely Cauchy dispersion formula and Sellmeier dispersion formula, described in *chapter I, subchapter 1-2*. The imaginary part of the dielectric function, $\varepsilon_2\,(E) = 2nk$, calculated as the product of variable band edge function *(G)* and Lorentz oscillator function *(L)*, in the whole region of measured spectra is then fitted using *e.g.* Cody-Lorentz (CL) model:

$$\varepsilon_{2CL}(E) = \begin{cases} \dfrac{E_1}{E} exp\left\{\dfrac{E - E_t}{E_u}\right\}; & 0 < E \leq E_t, \\ G(E)L(E) = \dfrac{\left(E - E_g^{opt}\right)^2}{(E - E_g^{opt})^2 + E_p^2} \dfrac{AE_0\Gamma E}{[(E^2 - E_0^2)^2 + \Gamma^2 E^2]}; & E > E_t, \end{cases}$$

Eq. 3-5

In CL model, *G (E)* function is given by empirical expression $G(E) \propto \left[\left(E - E_g^{opt}\right)^2 / \left(E - E_g^{opt}\right)^2 + E_p^2\right]$ derived on the assumption of parabolic bands and a constant dipole matrix; *L (E)* is simple Lorentz oscillator. E_t stands for demarcation energy between the Urbach tail transitions and the band-to-band transitions. For energies lower than E_t *(0 < E ≤ Et)*, Eq. 3-5 leads to the Urbach formula of absorption coefficient, *α(E) ∝ exp(E/Eu)*; where E_u represents Urbach energy [26]. Minimal value of Urbach energy for non-crystalline solids and liquids with optical gap of 1–9 eV is of ~50 meV. This value is connected with intrinsic density fluctuation in glassy structures. Another disorder such as compositional, heterogeneous and defective tend to increase value of this parameter [27]. Furthermore, E_1 is defined to hold the continuity of ε_2 at $E = E_t$: $E_1 = E_t L(E_t) G(E_t)$. For $E > E_t$, ε_{2CL} is given by the product of *G(E)* and *L(E)* functions. E_g^{opt} represents the optical bandgap energy. E_p stands for transition energy, given by the sum of $E_p + E_g^{opt}$. This transition energy separates the absorption onset at the $E < (E_p + E_g^{opt})$ from the Lorentz oscillator behaviour at $E > (E_p + E_g^{opt})$. Lorentz oscillator is described by its resonance energy (E_0), amplitude (A) and broadening (Γ), respectively.

The real part of dielectric function $\varepsilon_1(E) = n^2 - k^2$ is obtained by Kramers-Kronig relation of imaginary counterpart of the dielectric function $\varepsilon_2(E)$, [28].

The process of fitting the ellipsometry data is finalized by calculating the theoretical values of ψ and Δ using the selected model and comparing them with the measured values. The function of mean square error is usually employed for the comparison [24]:

$$\mathrm{MSE} = \sqrt{\frac{1}{2N - M} \sum_{i=1}^{N} \left[\left(\frac{\Psi_i^{mod} - \Psi_i^{exp}}{\sigma_{\Psi,i}^{exp}}\right)^2 + \left(\frac{\Delta_i^{mod} - \Delta_i^{exp}}{\sigma_{\Delta,i}^{exp}}\right)^2\right]}$$

Eq. 3-6

where N is number of measured pairs of ellipsometric parameters ψ and Δ; M is the total number of fitted parameters. $\sigma_{\Psi,i}^{exp}$ and $\sigma_{\Delta,i}^{exp}$ are estimated experimental errors of ellipsometric parameters [28].

3.6. Amplitude modulated atomic force microscopy (AM-AFM)

Atomic force microscopy seems to be powerful tool to examine the topographical properties of the surface of dielectric thin films such as chalcogenides. Lacking the electrons on the surface of such films, this scanning probe microscopy technique uses the special probe (cantilever) usually having silicon or silicon nitride tip with the reflective backside coating. The attractive/repulsive forces between the cantilever tip and the scanned surface cause the deflection of the tip, which is detected using laser diode and position photodetector (quadrant photodiode). Perhaps most often used AFM technique is amplitude modulated atomic force microscopy (AM-AFM). In AM-AFM, the tip of the cantilever is not in the contact with the

sample; however intermitted contact between the tip and the sample may occur. For this reason, AM-AFM is sometimes called “tapping mode” or “semi-contact mode”, [29].

Cantilever being “exited” using piezo close to its resonant frequency is approached to the sample surface until the set value of amplitude deflection (SetPoint) is achieved. Surface roughness of the film is then recorded by means of deviation from the SetPoint value. Feedback loop of the Z-signal returns the cantilever to the initial SetPoint value immediately, so the lateral information about the sample surface roughness is obtained [30]. The scheme of AM-AFM is shown in figure 3-5.

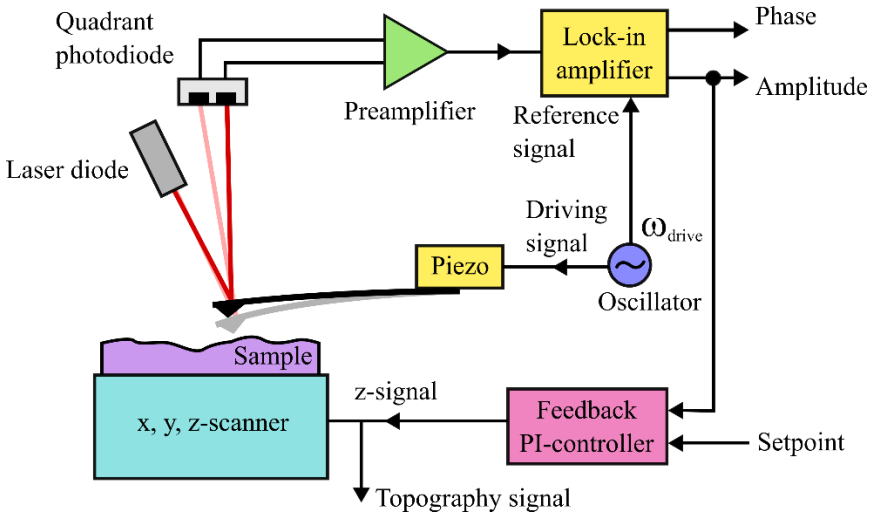

Fig. 3-5 AM-AFM detection scheme with lock-in amplifier for the detection of deviation of the oscillation amplitude from the SetPoint value – redraw from Voigtländer [30].

When one obtains the *z* information of lateral image (*x*, *y*), sample surface roughness is usually expressed by means of average roughness:

$$RA = \frac{1}{N}\sum_{i=1}^{N}|z_i - \bar{z}|$$

Eq. 3-7

or more often by root-mean squared roughness:

$$RMS = \left[\frac{1}{N}\sum_{i=1}^{N}(z_i - \bar{z})^2\right]^{1/2}$$

Eq. 3-8

3.7. Raman scattering spectroscopy

When the intense beam of monochromatic light interacts with the sample, it undergoes both elastic and inelastic scattering. The former, also called Rayleigh (or Tyndall) scattering, thus has the same frequency as the exciting radiation. The later called Raman scattering (Smekal-Raman effect) appears at both lower (Stokes) and higher (anti-Stokes) wavenumbers compared to excitation frequency (fig. 3-6), [31]. The stored energy produced by the distortion of electron clouds due to the incident electric field is transferred to the sample, exciting the vibrational modes [32]. The intensity of the Stokes line is proportional to λ^{-4}.

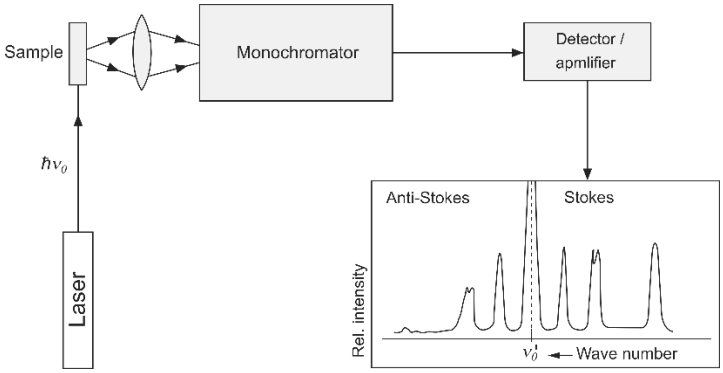

Fig. 3-6 Simplified scheme of Raman spectrometer and resulting spectrum – redraw from Klöpffer [31].

Raman spectroscopy is a primarily a structural characterization tool, which is more sensitive to the lengths, strengths and arrangement of bonds in a material than it is to the chemical composition. It is also particularly useful for investigating the structure of amorphous materials. Generally, the Raman spectra of amorphous solids exhibit broad bands centered at the wavenumbers which might correspond to the vibrational modes of their crystalline counterparts [32]. However, the peak position is strongly affected by the local structure in the glass network.

3.8. Beam self-trapping technique

Beam self-trapping technique is an experimental technique suitable for the measurements of nonlinear optical properties of thin films. It is based on the analysis of the spatial light beam distribution propagating in the slab waveguide. As depicted in figure 3-7, in such measurement the laser beam reshaped to an elliptical spot by cylindrical lens and focused by × 40 microscope objective enters the waveguide. The light is coupled using the combination of half-wave plate and polarizer. Beam distribution at the output of the waveguide is then monitored using IR camera with × 10 microscope objective [33].

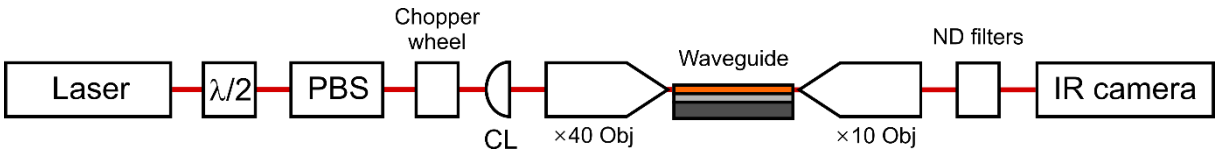

Fig. 3-7 Experimental set-up for beam self-action in chalcogenide planar waveguides. λ/2, half-wave plate; PBS, polarizing beam splitter; CL, cylindrical lens; Obj, microscope objective – redraw from Kuriakose *et al.* [34].

In the linear regime, the input bean being narrow (*i.e.* few tens of micrometres) enlarges due to the diffraction along few millimetres propagation distance. In nonlinear regime, the diffraction is modified due to either self-focusing (fig. 2-7 in chapter 1) or self-defocusing [35]. Considering both linear and nonlinear absorption the optical beam propagation is modelled by the nonlinear Schrödinger equation [36]:

$$\frac{\partial E}{\partial z} = -\frac{\alpha}{2} - \frac{\beta}{2}|E^2|\,E + iK_0 n_2 |E^2|\,E$$

Eq. 3-9

where electric field E is related to the intensity by $I = \lceil E^2 \rceil$. K_0 is the propagation constant in the medium. Nonlinear refractive index n_2 is deduced by analysis of the output beam profile modification as a function of the injected light power [35].

References

1. Kolobov A.V., Tominaga J., Chalcogenides : metastability and phase change phenomena, Berlin ; New York Springer, 2012,
2. Frumar M., Frumarova B., Nemec P., Wagner T., Jedelsky J., Hrdlicka M. Thin chalcogenide films prepared by pulsed laser deposition – new amorphous materials applicable in optoelectronics and chemical sensors. *Journal of Non-Crystalline Solids.* 2006;*352:*544-561.
3. Němec P., Frumar M., Frumarová B., Jelínek M., Lančok J., Jedelský J. Pulsed laser deposition of pure and praseodymium-doped Ge–Ga–Se amorphous chalcogenide films. *Optical Materials.* 2000;*15:*191-197.
4. Bouška M., Střižík L., Dostál L., Růžička A., Lyčka A., Beneš L., Vlček M., Přikryl J., Knotek P., Wágner T., Jambor R. Mixed Organotin(IV) Chalcogenides: From Molecules to Sn-S-Se Semiconducting Thin Films Deposited by Spin-Coating. *Chemistry - A European Journal.* 2013;*19:*1877-1881.
5. Keavney D., Falco C. Deposition Techniques for Magnetic Thin Films and Multilayers. In A. Chtchelkanova, S. Wolf and Y. Idzerda (eds), *Magnetic Interactions and Spin Transport*. Boston, MA: Springer US, 2003, 413-447.
6. Westwood W.D. Physical Vapor Deposition. In R. A. Levy (ed), *Microelectronic Materials and Processes*. Dordrecht: Springer Netherlands, 1989, 133-201.
7. Sarkar J. Chapter 2 - Sputtering and Thin Film Deposition. *Sputtering Materials for VLSI and Thin Film Devices*. Boston: William Andrew Publishing, 2014, 93-170.
8. Lin L., Wang G., Shen X., Dai S., Xu T., Nie Q. Photo-induced structural changes in Ge-Sb-Se films. *Infrared Physics & Technology.* 2017;*81:*59-63.
9. Halenkovič T., Gutwirth J., Němec P., Baudet E., Specht M., Gueguen Y., Sangleboeuf J.-C., Nazabal V. Amorphous Ge-Sb-Se thin films fabricated by co-sputtering: Properties and photosensitivity. *Journal of the American Ceramic Society.* 2018;*101:*2877-2887.
10. Wang H., Wang G., Shi D., Shen X., Lu Y., Nie Q. Compositional dependence of crystallization and structural stability in Ge–Sb–Se chalcogenide films. *Journal of Non-Crystalline Solids.* 2016;*453:*108-112.
11. Chen F., Zhang Z., Wang Y., Nie Q., Shen X., Dai S. Optical properties of amorphous In-doped GeSe2 films for all-optical applications. *Infrared Physics & Technology.* 2015;*69:*32-35.
12. Cho J.-Y., Kim D., Park Y.-J., Yang T.-Y., Lee Y.-Y., Joo Y.-C. The phase-change kinetics of amorphous Ge2Sb2Te5 and device characteristics investigated by thin-film mechanics. *Acta Materialia.* 2015;*94:*143-151.
13. Park T.-J., Choi S.-Y., Kang M.-J. Phase transition characteristics of Bi/Sn doped Ge2Sb2Te5thin film for PRAM application. *Thin Solid Films.* 2007;*515:*5049-5053.
14. Thornton J.A. Influence of substrate temperature and deposition rate on structure of thick sputtered Cu coatings. *Journal of Vacuum Science and Technology.* 1975;*12:*830-835.
15. Messier R.F. The nano-world of thin films. 2008.
16. Boolchand P., Georgiev D.G., Micoulaut M. Nature of glass transition in chalcogenides. *Journal of Optoelectronics and Advanced materials.* 2002;*4:*823-836.
17. Bindell J.B. 2.2 - SEM: Scanning Electron Microscopy. *Encyclopedia of Materials Characterization*. Boston: Butterworth-Heinemann, 1992, 70-84.
18. Ashby M.F., Ferreira P.J., Schodek D.L. Chapter 8 - Nanomaterials: Synthesis and Characterization. *Nanomaterials, Nanotechnologies and Design*. Boston: Butterworth-Heinemann, 2009, 257-290.
19. Morent R., De Geyter N. 1 - Improved textile functionality through surface modifications. *Functional Textiles for Improved Performance, Protection and Health*: Woodhead Publishing, 2011, 3-26.

20. Geiss R.H. 3.1 - EDS: Energy-Dispersive X-Ray Spectroscopy. *Encyclopedia of Materials Characterization*. Boston: Butterworth-Heinemann, 1992, 120-134.
21. Goldstein J.I., Newbury D.E., Echlin P., Joy D.C., Lyman C.E., Lifshin E., Sawyer L., Michael J.R. Generation of X-Rays in the SEM Specimen. *Scanning Electron Microscopy and X-ray Microanalysis: Third Edition*. Boston, MA: Springer US, 2003, 271-296.
22. Bertin E.P. Excitation and Nature of X-Rays; X-Ray Spectra. *Principles and Practice of X-Ray Spectrometric Analysis*. Boston, MA: Springer US, 1975, 3-49.
23. Toney M.F. 4.1 - XRD: X-Ray Diffraction. *Encyclopedia of Materials Characterization*. Boston: Butterworth-Heinemann, 1992, 198-213.
24. Zheng Y.-X., Zhang R.-J., Chen L.-Y. Ellipsometry and Its Applications in Stoichiometry. In A. Innocenti and N. Kamarulzaman (eds), *Stoichiometry and Materials Science - When Numbers Matter*, 2012.
25. Losurdo M., Bergmair M., Bruno G., Cattelan D., Cobet C., de Martino A., Fleischer K., Dohcevic-Mitrovic Z., Esser N., Galliet M., Gajic R., Hemzal D., Hingerl K., Humlicek J., Ossikovski R., Popovic Z.V., Saxl O. Spectroscopic ellipsometry and polarimetry for materials and systems analysis at the nanometer scale: state-of-the-art, potential, and perspectives. *Journal of Nanoparticle Research.* 2009;*11:*1521-1554.
26. Němec P., Zhang S., Nazabal V., Fedus K., Boudebs G., Moreac A., Cathelinaud M., Zhang X.H. Photo-stability of pulsed laser deposited GexAsySe100-x-y amorphous thin films. *Optics Express.* 2010;*18:*22944-22957.
27. Tanaka K. Minimal Urbach energy in non-crystalline materials. *Journal of Non-Crystalline Solids.* 2014;*389:*35-37.
28. Němec P., Moreac A., Nazabal V., Pavlišta M., Přikryl J., Frumar M. Ge–Sb–Te thin films deposited by pulsed laser: An ellipsometry and Raman scattering spectroscopy study. *Journal of Applied Physics.* 2009;*106:*103509.
29. Hölscher H., Schwarz U.D. Theory of amplitude modulation atomic force microscopy with and without Q-Control. *International Journal of Non-Linear Mechanics.* 2007;*42:*608-625.
30. Voigtländer B., Scanning Probe Microscopy: Atomic Force Microscopy and Scanning Tunneling Microscopy, Springer Berlin Heidelberg, 2015,
31. Klöpffer W. Raman Spectroscopy. *Introduction to Polymer Spectroscopy*. Berlin, Heidelberg: Springer Berlin Heidelberg, 1984, 62-75.
32. White W.B. 8.2 - Raman Spectroscopy. *Encyclopedia of Materials Characterization*. Boston: Butterworth-Heinemann, 1992, 428-441.
33. Kuriakose T., Baudet E., Halenkovič T., Elsawy M.M.R., Němec P., Nazabal V., Renversez G., Chauvet M. Measurement of ultrafast optical Kerr effect of Ge–Sb–Se chalcogenide slab waveguides by the beam self-trapping technique. *Optics Communications.* 2017;*403:*352-357.
34. Kuriakose T., Renversez G., Nazabal V., Elsawy M., Halenkovic T., Nemec P., Chauvet M. Experimental demonstration of plasmon-soliton coupling. *ArXiv e-prints*, 2018.
35. Kuriakose T., Nazabal V., Renversez G., Baudet E., Němec P., Boidin R., Chauvet M. Beam self-action in planar chalcogenide waveguides. *SPIE Photonics Europe*: 2016.
36. Aitchison J.S., Hutchings D.C., Kang J.U., Stegeman G.I., Villeneuve A. The nonlinear optical properties of AlGaAs at the half band gap. *IEEE Journal of Quantum Electronics.* 1997;*33:*341-348.

Chapter III

Results and discussion

1. Choice of the system

The thin films studied in the frame of this work come from Ge-Sb-Se, Ga-Sb-Se and Ge-Sb-Se-Te systems. The choice of studied systems was made based on below described reasons.

Due to the presence of arsenic in classical binary chalcogenides (As_2S_3, As_2Se_3), which is highly toxic in its elemental form, arsenic-based chalcogenides are supposed to be environmentally improper for some applications [1]. These include (bio)chemical sensors that are likely to be discarded after their use [2]. Thus, exploiting germanium as an alternative glass network former, with respect to required wide transparency in mid-IR region, high (non)linear refractive index and glass-forming ability, the Ge-Se system should be advantageous when compared to Ge-S or Ge-Te [3, 4]. Moreover, in contrast with arsenic-based chalcogenides, four-fold coordinated germanium atoms spatially sustain the glass network resulting in higher glass-transition temperature (T_g) and improved mechanical properties, *i.e.* network rigidity, strength and hardness [5]. Covalent glasses of ternary Ge-As-Se and Ge-Sb-Se systems have been recently widely studied due to relatively large glass-forming domain and good physical and mechanical properties in comparison with classical binary chalcogenide compounds. Despite the particular attractivity of Ge-As-Se system having greater glass-forming ability when compared to Ge-Sb-Se system, the introduction of antimony in the glass network provides higher polarizability increasing (non)linear refractive index and reduced photosensitivity [6] offering an interesting option for the applications in the field of nonlinear optics [7-9]. The glass-forming domain of Ge-Sb-Se system is shown in figure 1-1a.

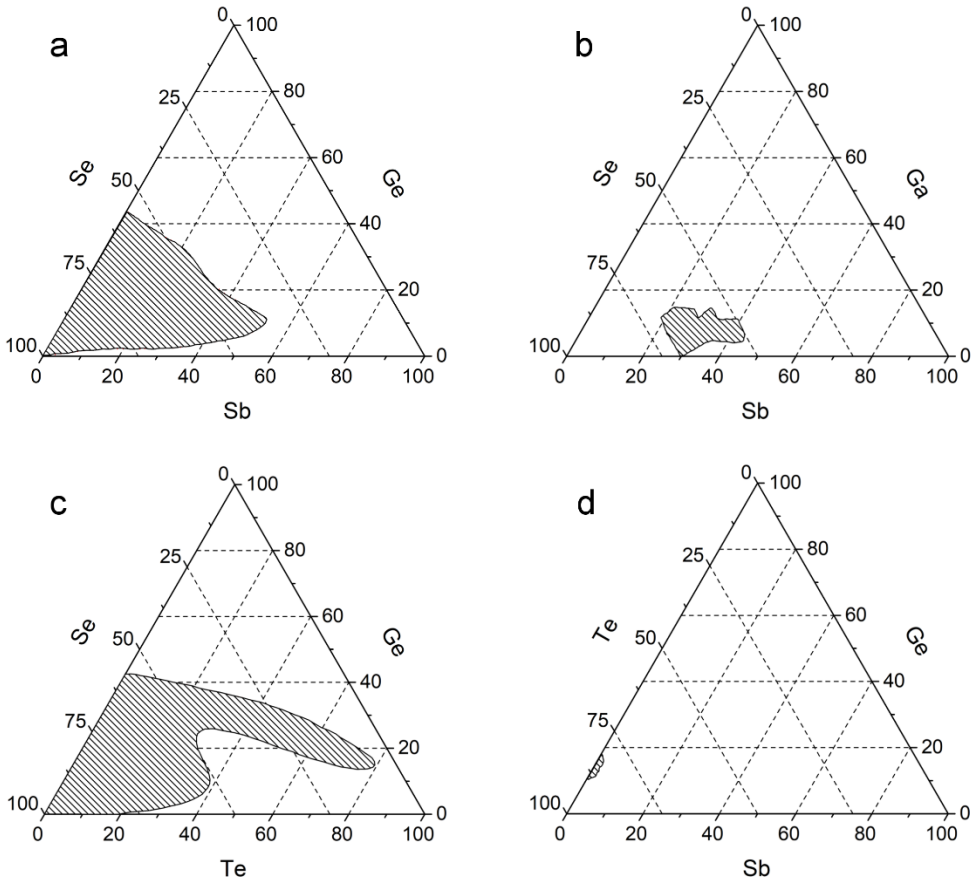

Fig. 1-1 Glass domains of chalcogenide glasses of **(a)** Ge-Sb-Se, **(b)** Ga-Sb-Se, **(c)** Ge-Se-Te and **(d)** Ge-Sb-Te systems – digitized data from various references [10-12].

Recently, germanium-free chalcogenide system of Ga-Sb-Se has been investigated by Lecomte *et al.* for the potential night-vision applications [11]. Furthermore, Sb-rich Ga-Sb-Se co-sputtered films are considered to be a potential replacement of GST for phase-change memories having higher thermal stability, smaller density change and higher crystallization speed when compared to GST [13]. The glass-forming domain of Ga-Sb-Se system is relatively large when compared to the Ge-Sb-Te one as shown in figures 1-1b and 1-1d. Potential application of Ga-Sb-Se amorphous thin films in the field of nonlinear optics should be also considered. Finally, this system may be also interesting for luminescence studies due to the good solubility of rare-earth elements in gallium-containing chalcogenide glasses/films. However, the photo-sensitivity of Ga-Sb-Se glasses/thin films has not been investigated until now.

The last system investigated in the frame of this thesis is Ge-Sb-Se-Te quaternary with Te content of 10 and 15 atomic percent. It has been shown by Sharma *et al.* that the substitution of selenium by tellurium leads to the increase in (non)linear refractive index making these chalcogenide glasses potential candidates for integrated optics, ultrahigh-bandwidth signal processing and infrared optical sensor applications [14]. High selenium concentration in Ge-Sb-Se-Te quaternary alloys is expected to increase the glass-forming domain as can be deduced from Ge-Se-Te ternary (fig. 1-1c).

2. Composition, optical properties and quality of co-sputtered and sputtered films

Optical properties of co-sputtered Ge-Sb-Se, Ga-Sb-Se and sputtered Ge-Sb-Se-Te thin films in the wavelength region of 300-2300 nm were investigated using variable angle spectroscopic ellipsometry (VASE, J. A. Woollam Co., Inc., Lincoln, NE, USA). For Ge-Sb-Se and Ga-Sb-Se thin films deposited on BK7 substrates, the data were collected at the angles of incidence of 50, 60 and 70° with 10 nm step. Three-layer model, consisting of substrate, actual thin film and simulated surface roughness (effective medium approximation consisting of 50 % of voids and 50 % of optical constants of film layer), was used for the determination of optical properties (*i.e.* optical bandgap and refractive index) and thickness. Imaginary part of dielectric function was fitted using Cody-Lorentz oscillator model. The data were fitted using WASE32 software.

Higher values of mean-squared error might be caused by the depolarization of light due to the reflection from the substrate (backside reflection). Such an effect may result in ~ 6 - 9 % of the incident light depolarization at the angle of incidence 70°. In the further research, the scotch tape was used to minimize the backside reflection effect. Using the scotch tape, which has similar value of refractive index as the substrate (however causes the scattering of the incident light), the depolarization of light coming from substrate backside reflection was minimized. Thus, the depolarization of light in the further measurements was mostly generated solely by the surface roughness. It should be noted, that the WASE32 software enables to adapt the data to the backside reflection effect. However, in this case, the backside reflection is not high enough to enable to fix this problem in this way. For the convenience the optical energy bandgap determined by VASE *via* CL model is referred to as E_g^{CL}.

Furthermore, optical bandgap was also determined from transmission-reflectance measurements in the range of 350-2500 nm employing Lambda 1050 spectrophotometer (Perkin-Elmer Inc., Waltham, MA, USA) or transmission measurements in the range of 180-3300 nm using spectrophotometer UV-3600 Plus (Shimadzu Co., Kyoto, Japan). Additionally to VASE, optical bandgap energy E_g^{opt}(hereinafter referred to as E_g^T) was obtained following Tauc approach [15] from energy dependence of $(\alpha\hbar\omega)^{1/2}$ by an extrapolation the linear part of the absorption edge curve found in the high absorption region ($\alpha \gtrsim 10^4$ cm^{-1}).

Generally, there is a good agreement between the values of E_g^{CL} and E_g^T, though the former is usually little bit higher. This can be reasonably explained when one compares the methodology of determination of optical bandgap values by these two methods [4].

2.1. Co-sputtered Ge-Sb-Se thin films

For the investigation of optical properties of thin films from Ge-Sb-Se system, co-sputtering of pseudo-binary systems of $GeSe_2$-Sb_2Se_3, $GeSe_2$-$Ge_{28}Sb_{12}Se_{60}$, Sb_2Se_3-$Ge_{28}Sb_{12}Se_{60}$ and $GeSe_4$-Sb_2Se_3 were examined. Three commercial targets with following composition were selected: polycrystalline $GeSe_2$ (American Elements Corp., Los Angeles, CA, USA), polycrystalline Sb_2Se_3 (American Elements Corp., Los Angeles, CA, USA), glassy $Ge_{28}Sb_{12}Se_{60}$ (Vitron GmbH., Jena, Germany). $GeSe_4$ target was prepared by conventional melt-quenching technique. X-ray diffraction of bulky $GeSe_4$ taken in the range of 2θ from 5 to 90° (with 0.026° step) indicates that the melt-quenched target is amorphous (fig. 2-1). The composition according EDS measurements is $Ge_{21.1}Se_{78.9}$ (± 1 at. %). The density measured at the room temperature (20 °C) was found to be 4.28 g.cm^{-3}. Finally, T_g was found to be 180 °C (at heating rate of 10 °C.min^{-1}) according the DSC measurements.

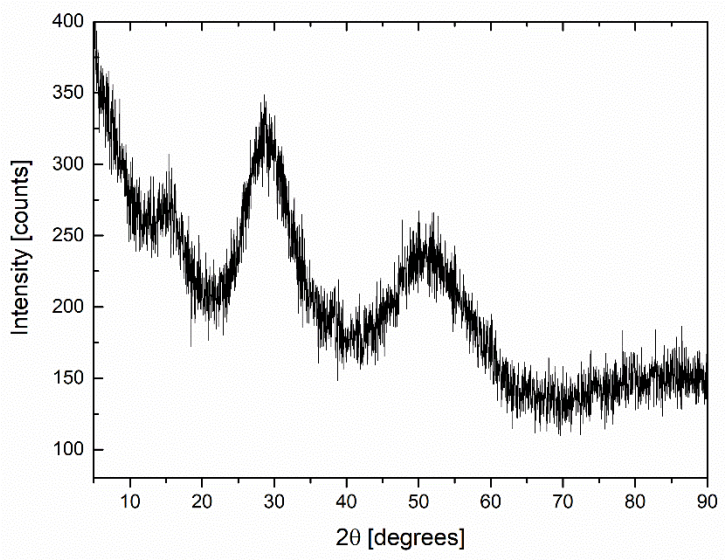

Fig. 2-1 XRD pattern of $GeSe_4$ bulk sample – raw data.

The sputtering depositions were performed at room temperature using MPE600 multi-chamber deposition system (Plassys-Bestek, Marolles-en-Hurepoix, France) with symmetrically arranged confocal deposition cluster consisting of three cathodes. The experimental conditions were held constant throughout all the depositions: background pressure $\leq 5 \times 10^{-7}$ mbar, Ar working pressure 5×10^{-3} mbar, Ar flow rate 75 sscm, with substrate holder rotation.

For the co-sputtering depositions from $GeSe_2$, Sb_2Se_3 and $Ge_{28}Sb_{12}Se_{60}$ targets, the electrical power on cathodes was chosen so the $P(C_x)+P(C_y)$ was always equal to 20 W. For the further investigation of $GeSe_4$-Sb_2Se_3 the maximum electrical power on $GeSe_4$ target was set to 12 W to minimize the damage of fragile target due to the erosion.

The depositions' details (electrical power on individual cathodes, deposition times) together with thicknesses, calculated deposition rates and measured chemical composition data are listed in tables 2-1 and 2-2. It should be noted that the morphology and the chemical composition was studied by scanning electron microscopy (SEM) with an energy-dispersive X-ray analyser (EDS, JSM 6400-OXFORD Link INCA, JEOL Ltd., Tokyo, Japan). For the evaluation of the chemical composition via EDS, L-lines were selected for all the constituting elements. Accelerating voltage used for SEM-EDS measurements was 10 kV.

As seen from Table 2-1 and 2-2, chemical composition of sputtered films obtained from $GeSe_2$, $GeSe_4$, Sb_2Se_3 and $Ge_{28}Sb_{12}Se_{60}$ was found to be close to the composition of targets in frame of EDS measurements uncertainty. It is worth to mention that the electrical power of 5 W on the cathode with $GeSe_2$ (sample Nr. 2) does not allow the detection of germanium by EDS. This indicates that the content of germanium is probably below the threshold limit of this technique. Even for the long experiment with deposition duration of 200 minutes resulting in the film with thickness of 1,110 nm (not shown in the table) the germanium was absent according EDS. It can be explained by the fact that the deposition rate at 5 W applied on the cathode with $GeSe_2$ is only ~0.6 $nm.min^{-1}$ compared to Sb_2Se_3 at 15 W (6.2 $nm.min^{-1}$) as found from 240 minutes long deposition. The average deposition rate at applied power of 10 W (15 W) is ~1.9 (3.7) $nm.min^{-1}$, ~3.0 (6.2) $nm.min^{-1}$ and ~2.4 (4.8) $nm.min^{-1}$ for $GeSe_2$, Sb_2Se_3, and $Ge_{28}Sb_{12}Se_{60}$. For $GeSe_4$, the average deposition rate at 10 W is ~2.0 $nm.min^{-1}$.

Table 2-1 The summary of deposition parameters of selected co-sputtered Ge-Sb-Se thin films from $GeSe_2$, Sb_2Se_3 and $Ge_{28}Sb_{12}Se_{60}$ targets with their thicknesses determined from VASE (± 2 nm), deposition rate and chemical compositions (± 1 at. %) evaluated by EDS.

Nr	Power (W)			Duration	Thickness	Deposition rate	Composition
	$GeSe_2$	Sb_2Se_3	$Ge_{28}Sb_{12}Se_{60}$	(min)	(nm)	($nm \cdot min^{-1}$)	(at. %)
1	-	15	-	120	740	6.2	$Sb_{39.4}Se_{60.6}$
2	5	15	-	150	950	6.3	$Sb_{39.9}Se_{60.1}$
3	7	13	-	150	890	6.0	$Ge_{5.0}Sb_{33.4}Se_{61.6}$
4	9	11	-	150	810	5.4	$Ge_{9.5}Sb_{28.7}Se_{61.8}$
5	10	10	-	150	830	5.5	$Ge_{12.3}Sb_{24.8}Se_{62.9}$
6	11	9	-	150	750	5.0	$Ge_{16.4}Sb_{19.4}Se_{64.2}$
7	13	7	-	150	650	4.3	$Ge_{23.4}Sb_{11.5}Se_{65.1}$
8	15	5	-	150	670	4.5	$Ge_{27.7}Sb_{5.9}Se_{66.4}$
9	15	-	-	120	440	3.6	$Ge_{32.1}Se_{67.9}$
10	15	-	5	150	710	4.6	$Ge_{32.5}Sb_{1.2}Se_{66.3}$
11	10	-	10	150	700	4.7	$Ge_{30.6}Sb_{6.7}Se_{62.7}$
12	5	-	15	150	720	4.8	$Ge_{27.3}Sb_{12.3}Se_{60.4}$
13	-	-	15	120	570	4.8	$Ge_{27.7}Sb_{12.3}Se_{60.0}$
14	-	5	15	150	830	5.5	$Ge_{23.3}Sb_{16.0}Se_{60.7}$
15	-	10	10	150	880	5.9	$Ge_{11.2}Sb_{28.4}Se_{60.4}$
16	-	15	5	150	1070	7.1	$Ge_{3.0}Sb_{36.3}Se_{60.7}$

Despite relatively different deposition rates, the real chemical compositions of films deposited at 10/10 W were found to be close to its theoretical pseudo-binary counterparts $(C_x)_{50}(C_y)_{50}$. The real chemical composition of co-sputtered $GeSe_2/Sb_2Se_3$ 10/10 W (sample Nr. 5 in Table 1) was found to be very close to an expected $(GeSe_2)_{50}(Sb_2Se_3)_{50}$, *i.e.* real composition $Ge_{12.3}Sb_{24.8}Se_{62.9}$ against theoretical $Ge_{12.5}Sb_{25}Se_{62.5}$. It is the case also for $GeSe_4/Sb_2Se_3$ 10/10 W (sample Nr. 22 listed in table 2) where the real composition is $Ge_{7.4}Sb_{24.5}Se_{68.1}$ against theoretical $Ge_{7.5}Sb_{25.0}Se_{67.5}$ in $(GeSe_4)_{50}(Sb_2Se_3)_{50}$ pseudo-binary. Similarly, in sample Nr. 11 in table 1 at 10/10 W deposited from $GeSe_2/Ge_{28}Se_{12}Se_{60}$, the real composition is $Ge_{30.6}Sb_{6.7}Se_{62.7}$ against $Ge_{30.7}Sb_{6.0}Se_{63.3}$. Finally, film deposited at the 10/10 W from $Sb_2Se_3/Ge_{28}Sb_{12}Se_{60}$ with composition $Ge_{11.2}Sb_{28.4}Se_{60.4}$ (sample Nr. 15 in table 1) contains a small deficit of antimony when compared to its theoretical pseudo-binary counterpart $(Sb_2Se_3)_{50}(Ge_{28}Sb_{12}Se_{60})_{50}$ having composition $Ge_{10.5}Sb_{29.5}Se_{60.0}$. This shows only very small limitation of predictive approach of co-sputtered film composition. Thus, the perfect knowledge

of deposition rate of individual targets, plasma characteristics, density and molecular weight of targets and films is necessary for predicting the chemical composition of co-sputtered films. However, the selenium content in the films is well maintained at given electrical power and argon working pressure [4].

Table 2-2 The summary of deposition parameters of selected co-sputtered Ge-Sb-Se thin films from $GeSe_4$ and Sb_2Se_3 targets with their thicknesses determined from VASE (± 2 nm), deposition rate and chemical compositions (± 1 at. %) evaluated by EDS.

Nr	Power (W)		Duration	Thickness	Deposition rate	Composition
	$GeSe_4$	Sb_2Se_3	(min)	(nm)	(nm·min^{-1})	(at. %)
17	10	-	360	710	2.0	$Ge_{19.6}Se_{80.4}$
18	12	5	180	740	4.1	$Ge_{14.0}Sb_{5.7}Se_{80.3}$
19	10	5	210	690	3.3	$Ge_{12.7}Sb_{10.5}Se_{76.8}$
20	10	6	180	650	3.6	$Ge_{10.9}Sb_{13.9}Se_{75.2}$
21	10	8	150	690	4.6	$Ge_{9.0}Sb_{20.2}Se_{70.8}$
22	10	10	150	820	5.5	$Ge_{7.4}Sb_{24.5}Se_{68.1}$
23	8	10	150	720	4.8	$Ge_{5.7}Sb_{28.8}Se_{65.5}$
24	6	10	180	720	4.0	$Ge_{2.9}Sb_{35.1}Se_{62.0}$

For clarity, chemical composition of co-sputtered Ge-Sb-Se thin films is also shown in the ternary diagram (fig. 2-2).

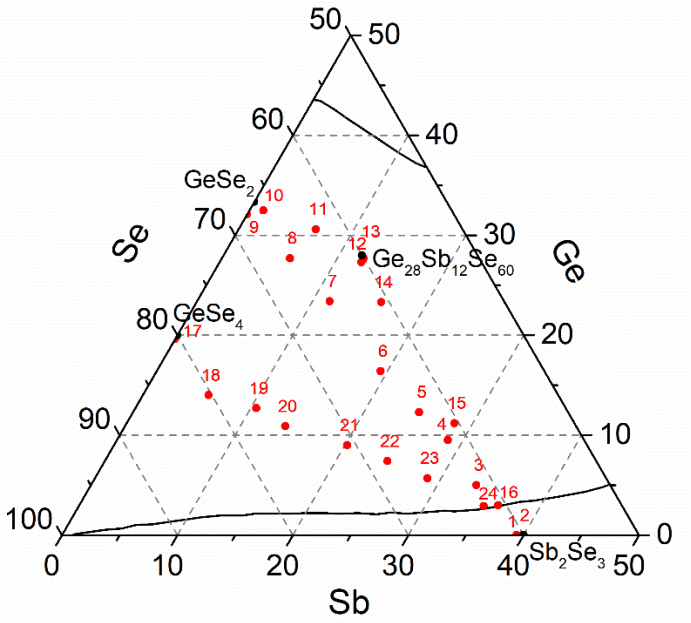

Fig. 2-2 Ternary Ge-Sb-Se diagram with indicated positions of co-sputtered thin films' composition (red points), targets' composition (black points), and glass-forming region (black curves).

Co-sputtered Ge-Sb-Se thin films were found to be of a good quality according SEM and AFM measurements. The amorphous state was confirmed by XRD (fig. 2-3). SEM micrographs of the surface have shown a good smoothness of fabricated co-sputtered thin films. Surface micrographs are shown in the figure 2-4. Furthermore, the cross-section micrographs (fig. 2-5)

have shown that the films are homogenous without any pores or cracks. Only a minimal columnar structure may be observed in fig. 2-5 (d).

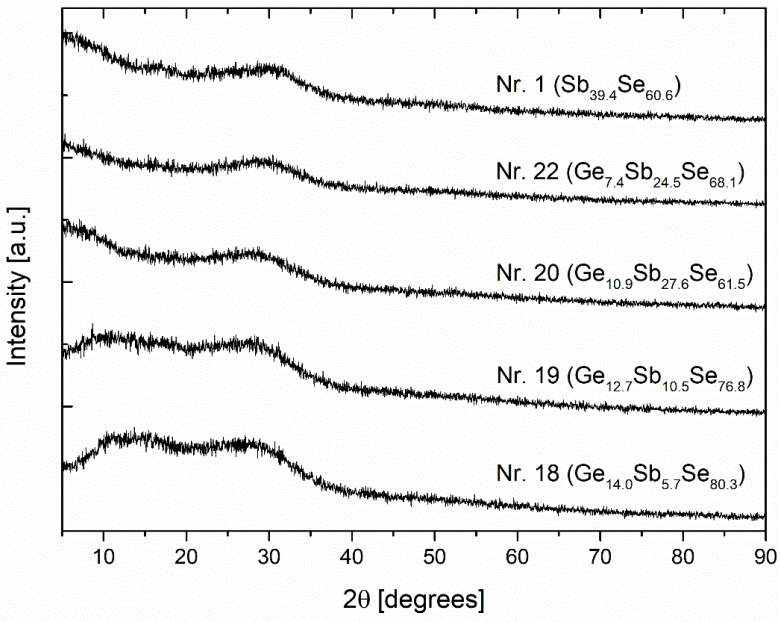

Fig. 2-3 XRD patterns of selected Ge-Sb-Se samples – raw data taken in the range of *2θ* from 5 to 90° (with 0.026° step).

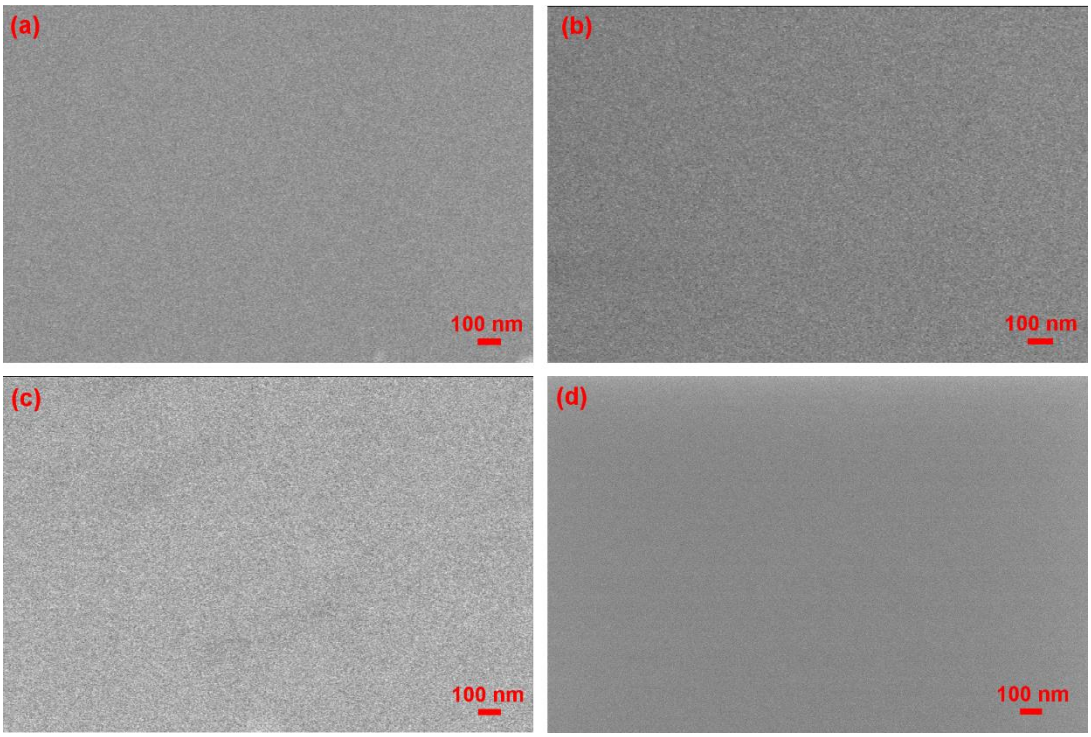

Fig. 2-4 SEM micrographs of the surface of Ge-Sb-Se co-sputtered films, **(a)** $GeSe_2/Sb_2Se_3$ 10/10 W, **(b)** $GeSe_2/Ge_{28}Sb_{12}Se_{60}$ 10/10 W, **(c)** $Sb_2Se_3/Ge_{28}Sb_{12}Se_{60}$ 10/10 W, **(d)** $GeSe_4/Sb_2Se_3$ 10/10 W.

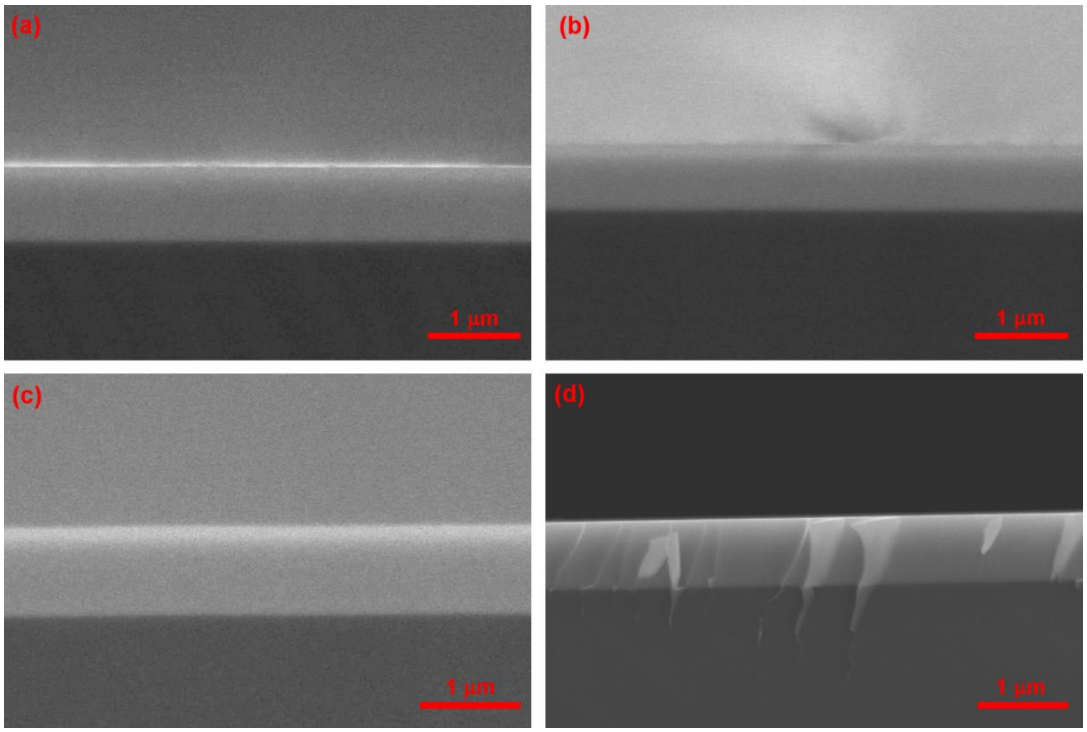

Fig. 2-5 Cross-section SEM micrographs of Ge-Sb-Se co-sputtered films, **(a)** $GeSe_2/Sb_2Se_3$ 10/10 W, **(b)** $GeSe_2/Ge_{28}Sb_{12}Se_{60}$ 10/10 W, **(c)** $Sb_2Se_3/Ge_{28}Sb_{12}Se_{60}$ 10/10 W, **(d)** $GeSe_4/Sb_2Se_3$ 10/10 W.

AFM measurements were performed within thin films deposited on the single crystalline silicon <100>. The rows were aligned using 2nd degree polynomial function. Surface topography of thin films is dependent on the target used for the deposition as seen in the figure 2-6. Root mean square roughness (Sq) values of co-sputtered films from $GeSe_2$, Sb_2Se_3 and $Ge_{28}Sb_{12}Se_{60}$ (samples Nr. 1 to Nr. 16) with the thickness range of ~440-1070 nm are typically ~0.4 ± 0.2 nm. However, the differences in topography were found for the particular targets. Grainier surface is observed for $Ge_{28}Sb_{12}Se_{60}$ target (fig. 2-6c). Moreover, high values of Sq were found for $GeSe_4$ sputtered film (fig. 2-6d). On the other hand, single cathode sputtered films of Sb_2Se_3 and $GeSe_2$ have very smooth surface (fig. 2-6a,b) confirmed by low values of Sq. During the co-sputtering with Sb_2Se_3 target, the roughness significantly decreases resulting in Sq values of about 0.2 nm.

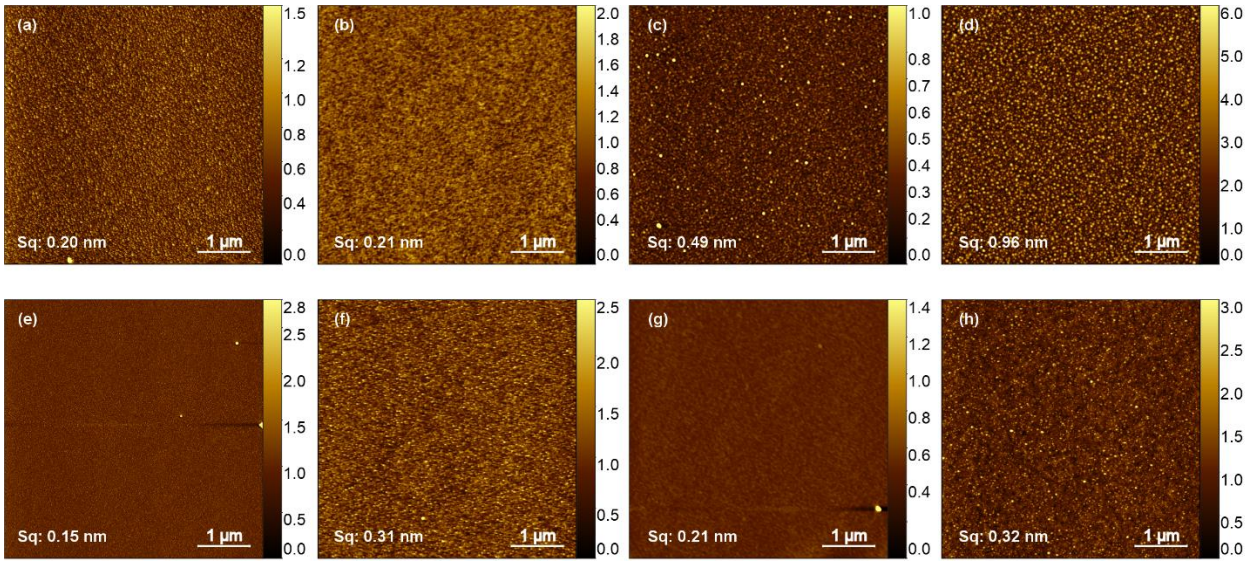

Fig. 2-6 AFM images of sputtered and co-sputtered films with indicated root-mean squared roughness (Sq); **(a)** $GeSe_2$ 10 W, **(b)** Sb_2Se_3 10 W, **(c)** $Ge_{28}Sb_{12}Se_{60}$ 10 W, **(d)** $GeSe_4$ 10 W, **(e)** $GeSe_2/Sb_2Se_3$ 10/10 W, **(f)** $GeSe_2/Ge_{28}Sb_{12}Se_{60}$ 10/10 W, **(g)** $Sb_2Se_3/Ge_{28}Sb_{12}Se_{60}$ 10/10 W, **(h)** $GeSe_4/Sb_2Se_3$ 10/10 W; values of z axis are in nanometres.

VASE data analysis results for co-sputtered Ge-Sb-Se thin films are summarized in the table 2-3. Due to the backside reflection resulting in high MSE values, some samples were fitted using the data collected only at the angles of incidence 50 and 60°. The backside reflection increases with increasing angle of incidence, so the data collected at 70° were excluded from the fit of those samples. MSE values of VASE data fits are lower than 6 (table 2-3), which can be considered as a good fit taking into account the thickness of films. For co-sputtered films Nr. 8, 11 and 24 is the value of MSE even below 2 confirming the suitability of CL model for the ellipsometry data fitting.

Table 2-3 The summary of selected co-sputtered Ge-Sb-Se thin films from $GeSe_2$, $GeSe_4$, Sb_2Se_3 and $Ge_{28}Sb_{12}Se_{60}$ targets with their chemical compositions (± 1 at. %) evaluated by EDS, mean-squared error (MSE) values of VASE data fits, optical bandgap energy E_g^{CL} (± 0.02 eV), refractive index at 1.55 μm (± 0.01), values of parameter E_u (Urbach energy, ± 10 meV) determined from VASE and optical bandgap energy determined from Tauc plots E_g^T (± 0.02 eV).

Nr	Composition (at. %)	MSE	E_g^{CL}(eV)	n @1.55 μm	E_u (meV)	E_g^T(eV)
1	$Sb_{39.4}Se_{60.6}$	5.45	1.34	3.34	55	1.39
2	$Sb_{39.9}Se_{60.1}$	4.98	1.37	3.33	59	1.39
3	$Ge_{5.0}Sb_{33.4}Se_{61.6}$	5.15*	1.45	3.07	95	1.52
4	$Ge_{9.5}Sb_{28.7}Se_{61.8}$	5.69*	1.55	2.92	111	1.64
5	$Ge_{12.3}Sb_{24.8}Se_{62.9}$	4.57*	1.65	2.80	98	1.68
6	$Ge_{16.4}Sb_{19.4}Se_{64.2}$	3.45*	1.73	2.69	146	1.78
7	$Ge_{23.4}Sb_{11.5}Se_{65.1}$	4.25*	1.85	2.52	154	1.95
8	$Ge_{27.7}Sb_{5.9}Se_{66.4}$	1.93*	1.93	2.45	183	2.03
9	$Ge_{32.1}Se_{67.9}$	5.19	2.09	2.38	87	2.11
10	$Ge_{32.5}Sb_{1.2}Se_{66.3}$	4.13*	2.01	2.37	86	2.08
11	$Ge_{30.6}Sb_{6.7}Se_{62.7}$	1.75*	1.93	2.48	113	1.94
12	$Ge_{27.3}Sb_{12.3}Se_{60.4}$	3.14*	1.70	2.64	122	1.75
13	$Ge_{27.7}Sb_{12.3}Se_{60.0}$	3.33	1.68	2.66	98	1.77
14	$Ge_{23.3}Sb_{16.0}Se_{60.7}$	4.45*	1.67	2.67	92	1.75
15	$Ge_{11.2}Sb_{28.4}Se_{60.4}$	4.62	1.55	2.93	89	1.63
16	$Ge_{3.0}Sb_{36.3}Se_{60.7}$	4.12*	1.40	3.20	65	1.45
17	$Ge_{19.6}Se_{80.4}$	2.36	1.97	2.44	111	1.99
18	$Ge_{14.0}Sb_{5.7}Se_{80.3}$	2.31	1.87	2.56	91	1.88
19	$Ge_{12.7}Sb_{10.5}Se_{76.8}$	2.66	1.82	2.59	121	1.83
20	$Ge_{10.9}Sb_{13.9}Se_{75.2}$	2.31	1.77	2.66	118	1.80
21	$Ge_{9.0}Sb_{20.2}Se_{70.8}$	2.35	1.68	2.76	74	1.69
22	$Ge_{7.4}Sb_{24.5}Se_{68.1}$	2.22	1.61	2.86	92	1.61
23	$Ge_{5.7}Sb_{28.8}Se_{65.5}$	2.81	1.55	2.95	84	1.54
24	$Ge_{2.9}Sb_{35.1}Se_{62.0}$	1.86	1.47	3.12	86	1.46

* Angle of incidence of 70° excluded from the fit.

The study of optical properties, by means of optical bandgap values, of single cathode depositions from targets of $GeSe_2$, Sb_2Se_3, $Ge_{12}Sb_{28}Se_{60}$ and $GeSe_4$ showed a good agreement with the literature. Optical bandgap of sputtered Sb_2Se_3 determined by VASE was found to be 1.34 ± 0.02 eV (E_g^T = 1.39 ± 0.02 eV), which is close to the value of 1.39 ± 0.02 eV for evaporated Sb_2Se_3 films reported by Chen *et al.* determined by ellipsometry [16]. For $GeSe_2$ film, E_g^{CL} having the value of 2.09 ± 0.02 eV (E_g^T = 2.11 ± 0.02 eV) is close to the data published by various authors. For evaporated thin films, the value of optical bandgap of 2.06 eV determined from Tauc plot was reported by Tichý *et al.* [17]. Using the same approach, Chen *et al.* [18] reported the value of 2.04 eV. Somewhat lower value of Tauc bandgap for pulsed-laser deposited films having the value of 1.95 eV ± 0.01 eV was found by Pan *et al.* [19]. $E_g^{CL}$and E_g^T for sputtered $Ge_{28}Sb_{12}Se_{60}$ films were found to be 1.68 ± 0.02 eV and 1.77 ± 0.02 eV respectively. These values are in a good agreement with data reported for sputtered films by Balan *et al.*, where E_g^T is ~ 1.65 eV [20]. Finally, optical bandgap E_g^{CL} of sputtered $GeSe_4$ was

found to be 1.97 eV ± 0.02 eV (E_g^T = 1.99 ± 0.02 eV) being only slightly higher than the value of pulsed-laser deposited $GeSe_4$ (E_g^T = 1.92 ± 0.01 eV) reported by Pan *et al.* [19].

The minimum value of parameter E_U was found in the sample Nr. 1 (Sb_2Se_3). For the samples Nr. 9 ($GeSe_2$) and Nr. 17 ($GeSe_4$) are E_U values of 87 and 111 meV, respectively. These are much higher than those found by Oheda [21] who referred the values of Urbach slope in ~100 to 200 μm thick bulk samples of Ge_xSe_{1-x} system of about ~73 and ~74 meV for $GeSe_2$ and $GeSe_4$ respectively. This can be probably explained by potential higher degree of disorder in thin films when compared to bulk glasses. For co-sputtered Ge-Sb-Se thin films, no direct relationship between electrical power on individual cathodes can be concluded. However, the high antimony content in films seems to result in the 'sharpening' of the absorption edge.

The band structure of ternary glasses is not precisely known and its preparation-dependency plays a significant role in the optical properties. However, the general trends can be predicted from the normal bonding structure of Ge-Sb-Se system [4]. Electronic structure of amorphous and crystalline $GeSe_2$ *via* density functional theory (DFT) of valence band (VB) and conduction band (CB) density of states (DOS) was reported by Hachiya [22]. According to Carey *et al.* [23], the VB in Sb_2Se_3 comprises of Sb *5 s/p* with a contribution from Se *4p* states as determined by DOS. Furthermore, Sati *et al.* [24] published the XPS data for valence bands in $Ge_{40-x}Sb_xSe_{60}$ (x = 8, 10) glasses. The peaks at the very top of VB (valence band maxima – VBM) are ascribed to lone-pair electron states in selenium and Sb *5p* bonding electrons in Sb–Sb bonds. Another contributions found at the VBM are coming from Ge *4p* states participating in Ge–Ge bonds and Se *4p* states [24]. Similar behaviour was found in Ge-Sb-S glasses where the VBM in XPS spectra comprises of Ge *4p*, S *3p* and S lone-pair states [25]. From the comparison of XPS spectra of valence band in $Ge_{32}Sb_8Se_{60}$ and $Ge_{20}Sb_{20}Se_{60}$ glasses, slight shift in the binding energy may be observed [24]. Thus, the reduction in the bandgap energy in Ge-Sb-Se system when increasing antimony content may be ascribed to the Sb *5p* bonding electrons contributing to VBM [4]. Red-shift in the fundamental short-wavelength absorption edge with increasing antimony content in co-sputtered $GeSe_2$-Sb_2Se_3 (E_g^{CL}= 2.09-1.34 eV), $GeSe_2$-$Ge_{28}Sb_{12}Se_{60}$ (E_g^{CL}= 2.09-1.68 eV) and Sb_2Se_3-$Ge_{28}Sb_{12}Se_{60}$ (E_g^{CL}= 1.34-1.68 eV) films is shown in the figure 2-7. Qualitatively similar red-shift is found also in co-sputtered $GeSe_4$-Sb_2Se_3 (E_g^{CL}= 1.97-1.34 eV) thin films (fig. 2-8).

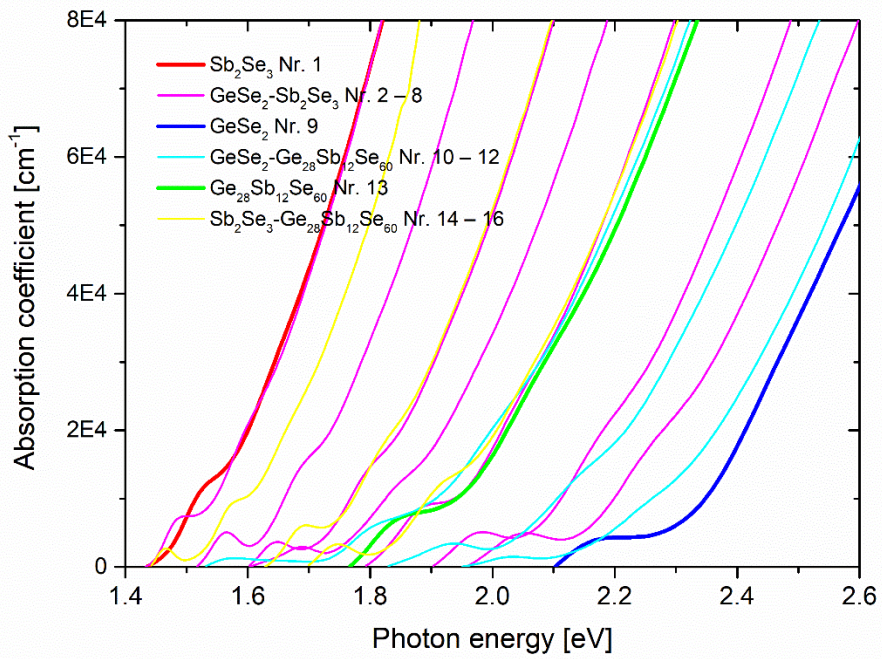

Fig. 2-7 Fundamental short-wavelength absorption edge of co-sputtered $GeSe_2$-Sb_2Se_3, $GeSe_2$-$Ge_{28}Sb_{12}Se_{60}$ and Sb_2Se_3-$Ge_{28}Sb_{12}Se_{60}$ films and films sputtered from individual targets.

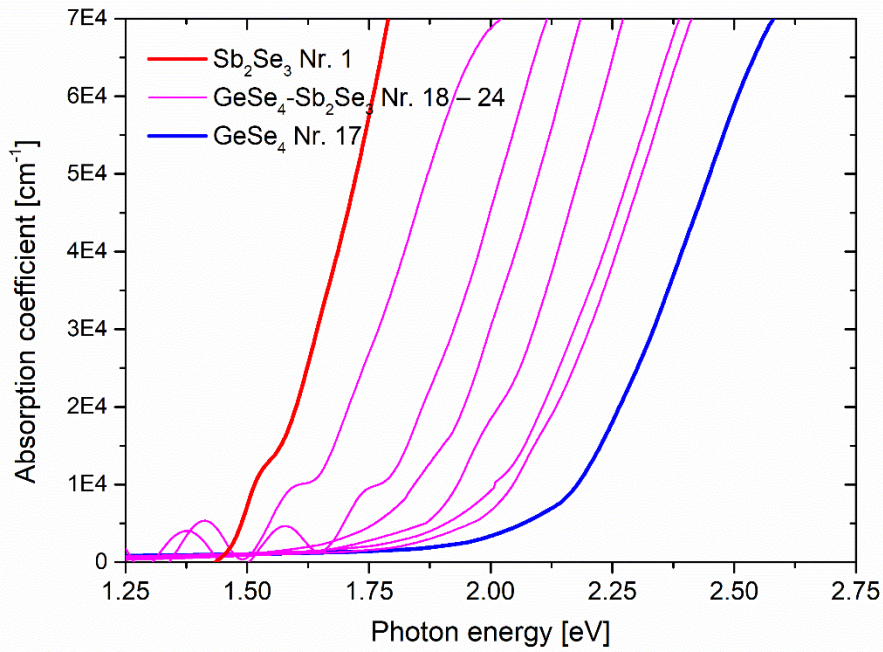

Fig. 2-8 Fundamental short-wavelength absorption edge of $GeSe_4$-Sb_2Se_3 co-sputtered films.

Values of optical bandgap energy E_g^{CL} and refractive index at 1.55 µm are plotted in the ternary contour diagrams shown in the figure 2-9. The black dots correspond to the data points of each selenide thin films and the colored surfaces correspond to an interpolation between the data points. As seen, optical properties of co-sputtered films can be gradually tailored in terms of optical bandgap and refractive index. Furthermore, wide range of bandgap and refractive index is obtained by simple variation of electrical power on individual cathodes by co-sputtering technique. Values of E_g^{CL} and refractive index at 1.55 µm are found to cover the range between extreme values representing the individual targets – *i.e.* 2.09 eV (n = 2.38) for $GeSe_2$,

1.97 eV (n = 2.44) for $GeSe_4$, 1.68 eV for $Ge_{28}Sb_{12}Se_{60}$ (n = 2.66) and 1.34 eV for Sb_2Se_3 (n = 3.34).

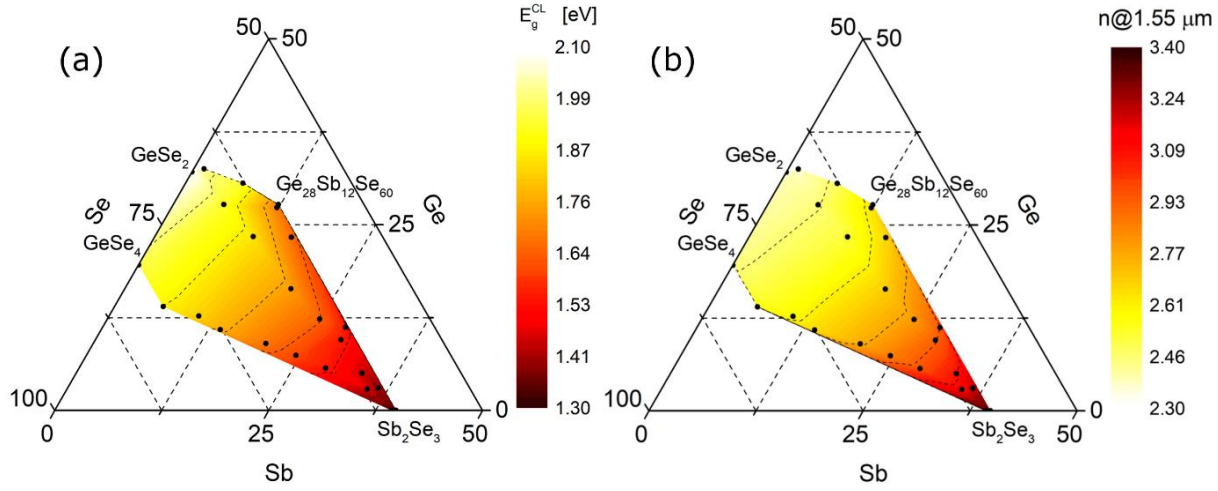

Fig. 2-9 Ternary contour diagrams showing the variation of optical bandgap energy **(a)** and refractive index **(b)** at 1.55 µm throughout the composition of Ge-Sb-Se co-sputtered thin films.

2.2. Co-sputtered Ga-Sb-Se thin films

Co-sputtered thin films from the system Ga-Sb-Se were deposited using polycrystalline targets of Ga_2Se_3 and Sb_2Se_3. The deposition rate of Ga_2Se_3 was found to be only around 0.8 and 1.8 nm·min^{-1} at 10 and 15 W, respectively. Recalling estimated deposition rates for Sb_2Se_3, *i.e.* ~3.0 and 6.2 nm·min^{-1} for 10 and 15 W, respectively, it is obvious that no composition equal to the composition of pseudo-binary $(Ga_2Se_3)_{50}(Sb_2Se_3)_{50}$ (*i.e.* $Ga_{20}Sb_{20}Se_{60}$) can be achieved. The depositions were carried out in order to achieve acceptable thickness (at least 500 nm); however, due to the large difference in the deposition rate of the two targets and low deposition rate for Ga_2Se_3, it was not possible to use $P(C_x)+P(C_y)$ always equal to 20 W as for co-sputtered Ge-Sb-Se films. An overview of the deposition parameters used for fabrication of Ga-Sb-Se thin films *via* co-sputtering is summarized in the table 2-4. The morphology and the chemical composition was studied by SEM-EDS (TESCAN 5130SB, TESCAN, Brno, Czech Republic). Accelerating voltage used for SEM-EDS measurements was 10 kV.

Table 2-4 The summary of deposition parameters of selected co-sputtered Ga-Sb-Se thin films from Ga_2Se_3 and Sb_2Se_3 targets with their thicknesses determined from VASE (± 2 nm), deposition rate and chemical compositions (± 1 at. %) evaluated by EDS.

Nr	Power (W)		Duration	Thickness	Deposition rate	Composition
	Ga_2Se_3	Sb_2Se_3	(min)	(nm)	(nm·min^{-1})	(at. %)
1	20	0	300	790	2.6	$Ga_{37.6}Se_{62.4}$
2	25	5	180	610	3.4	$Ga_{31.7}Sb_{5.2}Se_{63.1}$
3	20	5	240	700	2.9	$Ga_{30.3}Sb_{6.9}Se_{62.8}$
4	20	8	210	790	3.7	$Ga_{19.2}Sb_{17.5}Se_{63.3}$
5	20	10	120	560	4.7	$Ga_{16.7}Sb_{21.7}Se_{61.6}$
6	20	12	120	670	5.6	$Ga_{13.6}Sb_{24.7}Se_{61.7}$
7	20	15	90	620	6.9	$Ga_{10.9}Sb_{27.6}Se_{61.5}$
8	15	15	120	730	6.1	$Ga_{7.6}Sb_{31.2}Se_{61.2}$

It should be noted that only very few reports about Ga-Sb-Se system has been published. One of the reasons may be the fact that this system exhibits limited glass-forming ability (fig. 2-10). Figure 2-10 also shows the chemical composition of Ga-Sb-Se co-sputtered thin films in ternary diagram. Based on above mentioned facts, it is evident that co-sputtering is an efficient deposition method to fabricate amorphous thin films whose composition is out of glass-forming region of the system under study.

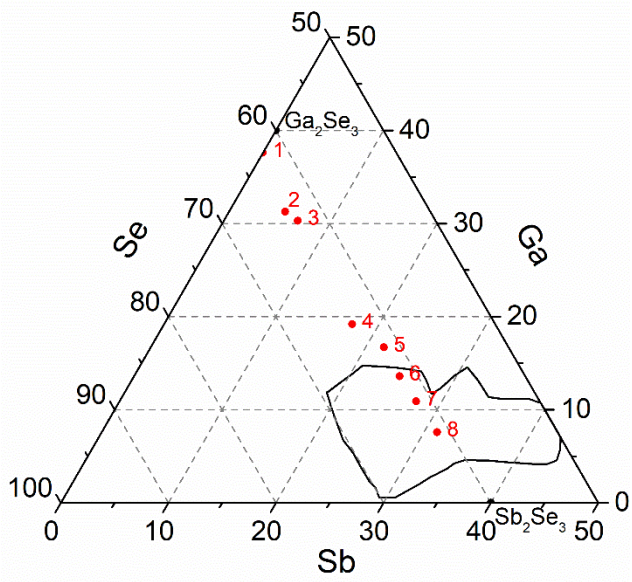

Fig. 2-10 Ternary Ga-Sb-Se diagram with indicated positions of co-sputtered thin films' composition (red points), targets' composition (black points) and glass-forming region (black curve).

Amorphous state of the prepared Ga-Sb-Se thin films was confirmed by measured XRD data (fig. 2-11). SEM micrographs of the surface confirmed a good quality of co-sputtered Ga-Sb-Se thin films as shown in the figure 2-12.

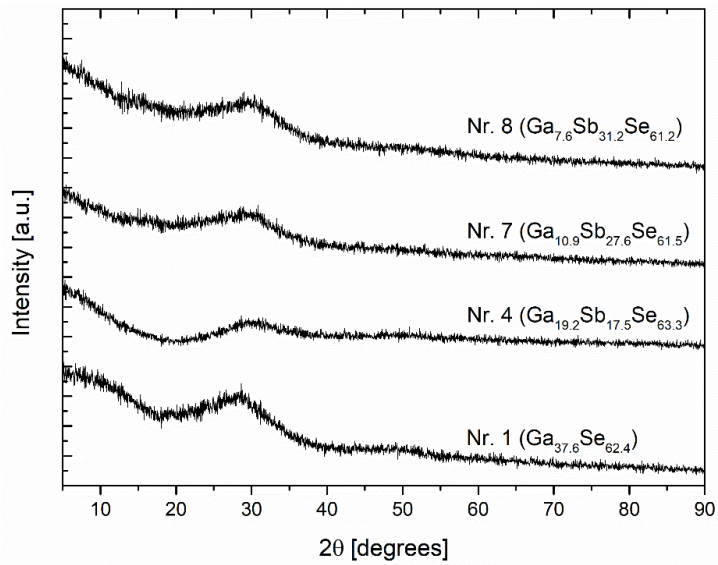

Fig. 2-11 XRD patterns of selected Ga-Sb-Se thin films – raw data taken in the range of 2θ from 5 to 90° (with 0.026° step).

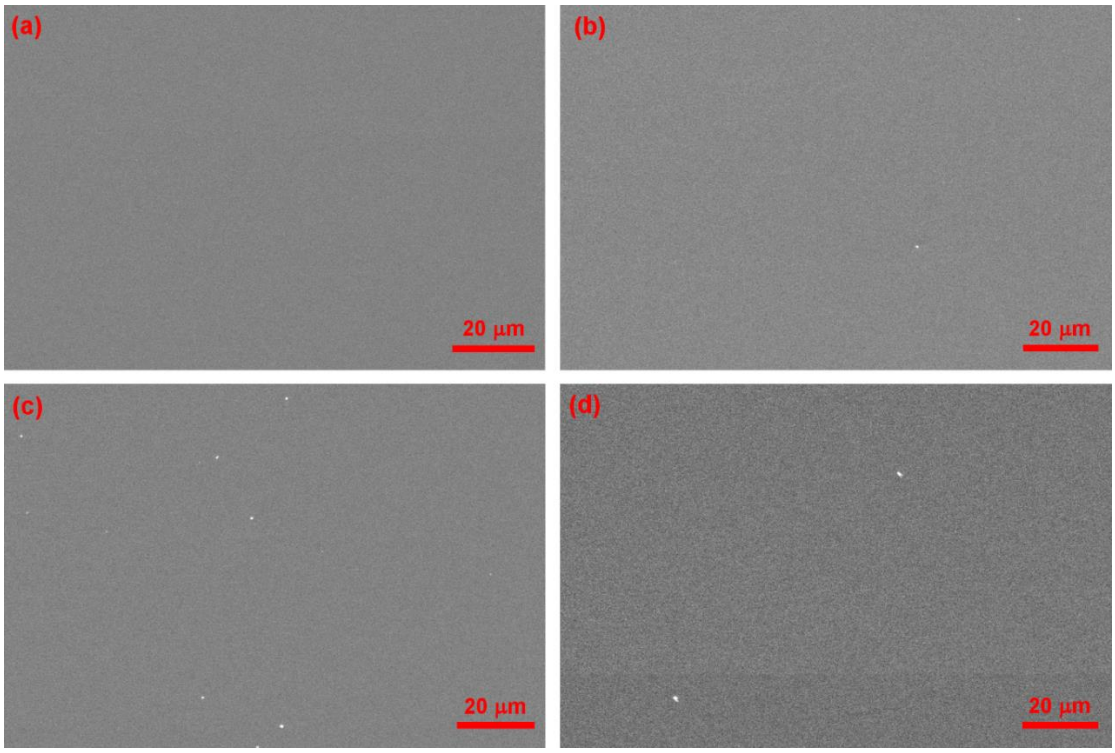

Fig. 2-12 SEM micrographs of the surface of sputtered Ga_2Se_3 film and Ga-Sb-Se co-sputtered films, (a) Ga_2Se_3 20 W, (b) Ga_2Se_3/Sb_2Se_3 20/15 W, (c) Ga_2Se_3/Sb_2Se_3 20/15 W, (d) Ga_2Se_3/Sb_2Se_3 15/15 W.

Furthermore, AFM images (fig. 2-13) have shown that the film deposited from Ga_2Se_3 target only contains particles ranging in the size between 35-60 nm (fig. 2-13a). Presence of these particles results in the high Sq value of 3.0 nm. Moreover, AFM scans performed on the area of 1×1 µm (fig. 2-13e) showed no deviation in topography (and RMS roughness) when compared with the other films when Sb_2Se_3 target is used for co-sputtering. For further depositions above mentioned particles were not observed and the values of RMS roughness were ~0.2 ± 0.1 nm for Ga-Sb-Se film thickness of about 600-800 nm. Similarly, as in the case of Ge-Sb-Se co-sputtered films, Sb_2Se_3 cathode decreases the roughness significantly when used.

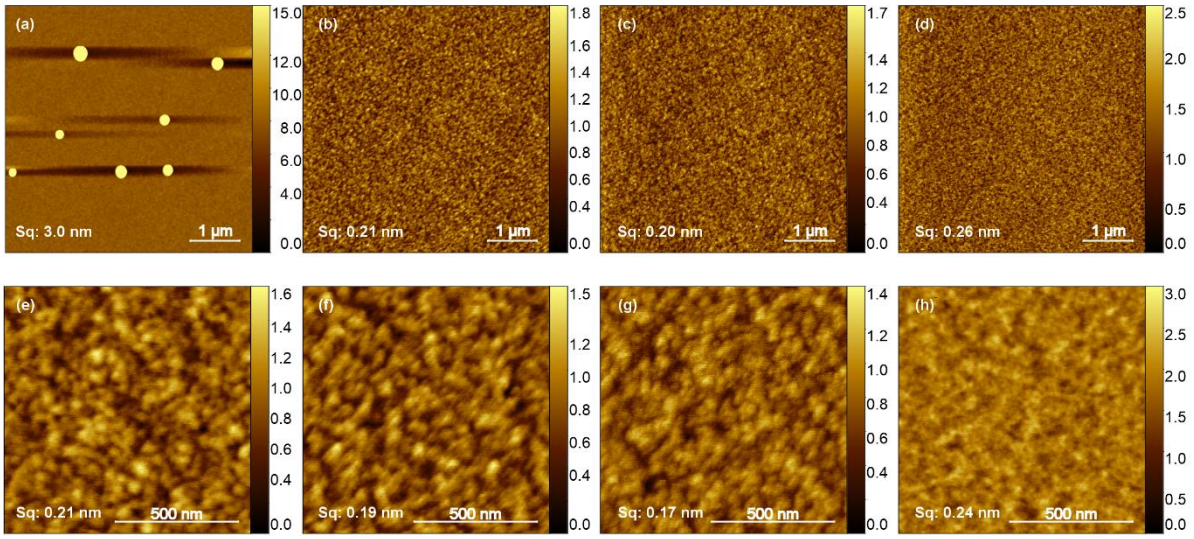

Fig. 2-13 AFM images of sputtered Ga_2Se_3 and co-sputtered Ga-Sb-Se films with indicated root-mean squared roughness (Sq); **(a)** Ga_2Se_3 20 W, 5×5 µm, **(b)** Ga_2Se_3/Sb_2Se_3 20/10 W, 5×5 µm, **(c)** Ga_2Se_3/Sb_2Se_3 20/15 W, 5×5 µm, **(d)** Ga_2Se_3/Sb_2Se_3 15/15 W, 5×5 µm, **(e)** Ga_2Se_3 20 W, 1×1 µm, **(f)** Ga_2Se_3/Sb_2Se_3 20/10 W, 1×1 µm, **(g)** Ga_2Se_3/Sb_2Se_3 20/15, W 1×1 µm, **(h)** Ga_2Se_3/Sb_2Se_3 15/15 W, 1×1 µm; values of z axis are in nanometres.

Table 2-5 The summary of selected co-sputtered Ga-Sb-Se thin films from Ga_2Se_3 and Sb_2Se_3 targets with their chemical compositions (± 1 at. %) evaluated by EDS, mean-squared error (MSE) values of VASE data fits, optical bandgap energy E_g^{CL} (± 0.02 eV), refractive index at 1.55 µm (± 0.01), values of parameter E_u (Urbach energy, ± 20 meV) determined from VASE and optical bandgap energy determined from Tauc plots E_g^T (± 0.02 eV).

Nr	Composition (at. %)	MSE	E_g^{CL}(eV)	n @1.55 µm	E_u (meV)	E_g^T(eV)
1	$Ga_{37.6}Se_{62.4}$	1.23	1.92	2.47	160	2.02
2	$Ga_{31.7}Sb_{5.2}Se_{63.1}$	1.25	1.80	2.59	140	1.83
3	$Ga_{30.3}Sb_{6.9}Se_{62.8}$	0.98	1.74	2.62	120	1.79
4	$Ga_{19.2}Sb_{17.5}Se_{63.3}$	1.47	1.65	2.80	90	1.65
5	$Ga_{16.7}Sb_{21.7}Se_{61.6}$	1.47	1.58	2.87	96	1.61
6	$Ga_{13.6}Sb_{24.7}Se_{61.7}$	1.11	1.56	2.94	85	1.60
7	$Ga_{10.9}Sb_{27.6}Se_{61.5}$	0.95	1.53	3.02	79	1.57
8	$Ga_{7.6}Sb_{31.2}Se_{61.2}$	1.11	1.48	3.11	76	1.53

VASE data analysis results for co-sputtered Ga-Sb-Se thin films are summarized in the table 2-5. Data were fitted using the data measured at angles of incidence of 50, 60 and 70°. Fitting of the ellipsometry data using CL model seems to be suitable for these films since the MSE values are pretty low, not exceeding 1.5.

The value of optical bandgap energy E_g^T of Ga_2Se_3 film is in a good agreement with the literature. Afifi *et al.* [26] reported the value of 2.06 eV for evaporated Ga_2Se_3 using Tauc extrapolation (E_g extracted from ellipsometry data). As expected, the increase of antimony content shifts the fundamental short-wavelength absorption edge towards the lower energies. Furthermore, as seen from the table 2-5, the value of E_U corresponding to Urbach energy decreases from 160 ± 20 meV in Ga_2Se_3 film down to 76 ± 20 meV in $Ga_{7.6}Sb_{31.2}Se_{61.2}$. Therefore, it can be concluded that the values of E_u parameter decrease with increasing

antimony content. Such 'sharpening' of absorption edge is also demonstrated in the figure 2-14 *via* change in the slope of the absorption coefficient curves. This may indicate that the introduction of three-fold coordinated antimony induces the higher order in disordered films, possibly reducing the number of homopolar bonds such as Se–Se, Ga–Ga and selenium chains.

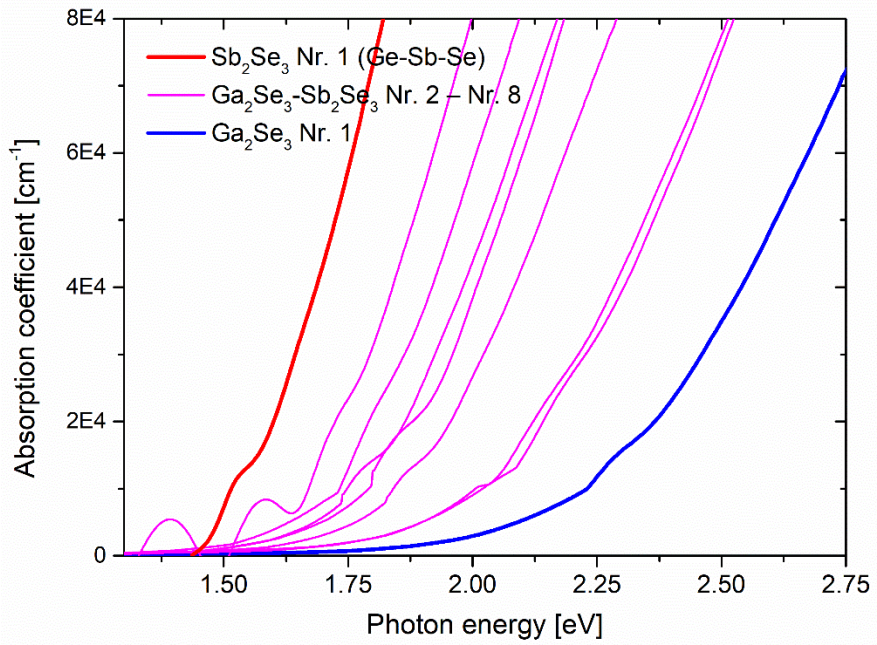

Fig. 2-14 Fundamental short-wavelength absorption edge of Ga-Sb-Se co-sputtered films.

2.3. Sputtered Ge-Sb-Se-Te thin films

Thin amorphous Ge-Sb-Se-Te films were sputtered using the targets with the composition based on the Ge-Sb-Se glass previously described as 2S1G-Se4 by Olivier *et al.* corresponding to $(GeSe_2)_{70}(Sb_2Se_3)_{30}$ pseudo-binary $(Ge_{19.4}Sb_{16.7}Se_{63.9})$ [8]. This particular composition was selected due to its suitability for nonlinear photonics devices applications [27]. Due to its good transparency in mid-IR region relative to sulphides, this composition is also suitable for the mid-IR sensors for the sea water pollution detection [28, 29]. In order to increase the refractive index, selenium was partially altered by tellurium in the amount of 10 and 15 atomic percent. Thus, these compositions will be referred to as 2S1G-Se4-Te10 afterwards. Sputtering targets were prepared by conventional melt-quenching technique. X-ray diffraction patterns of bulky Ge-Sb-Se-Te taken in the range of 2θ from 5 to 90° (with 0.026° step) indicate that the melt-quenched targets are predominantly amorphous (fig. 2-15). The values of T_g for these compositions were found to be 244 and 231 °C (at heating rate of 10 °C.min^{-1}) respectively, according the DSC measurements. The decrease of T_g with increasing tellurium content is in a good agreement with recently published data for Tb^{3+} doped $Ga_5Ge_{20}Sb_{10}Se_{65-x}Te_x$ bulk glasses [30].

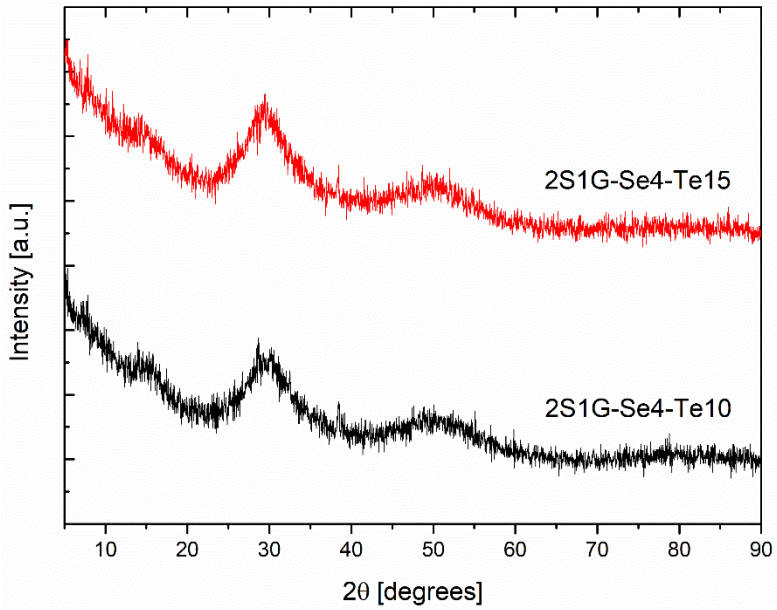

Fig. 2-15 XRD patterns of 2S1G-Se4-Te10 and 2S1G-Se-Te15 bulk samples – raw data taken in the range of 2θ from 5 to 90° (with 0.026° step).

Thin films were deposited at the constant deposition duration of 60 minutes. The electrical power on cathode was set to 10 and 15 W respectively. Furthermore, the argon pressure controlled by argon flow was set on 5×10^{-3} mbar and 10×10^{-3} mbar to assess the influence of argon pressure on the characteristics of the sputtered films. All the depositions' parameters are summarized in table 2-6. Samples exploiting 2S1G-Se4-Te10 target are marked as Nr. 1 – 4 and thin films fabricated using 2S1G-Se-Te15 target as Nr. 5 – 8. The deposition rate is significantly higher when compared to co-sputtering technique (table 2-1, 2-2, 2-4). This can be explained by the differences in the geometry of these two techniques and also of the two sputtering machines. In the sputtering technique used for the deposition of Ge-Sb-Se-Te thin films, the substrate rotating around its own axis is much closer to the target during the sputtering. While there is only negligible influence of argon pressure on the deposition rate, the electrical power increment by 5 W almost doubles this parameter – roughly from ~11 to ~21 $nm.min^{-1}$ and from ~13 to ~21 $nm.min^{-1}$ for 2S1G-Se4-Te10 and 2S1G-Se4-Te10 respectively. By means of stoichiometry determined by EDS, all the samples contain lower tellurium content than expected. However, the loss of tellurium is probably coming from the synthesis process according the EDS measurements performed on bulk material. For the EDS, the JEOL JED-2300 analysis station was used (L-lines for all the elements). Accelerating voltage used for SEM-EDS measurements was 10 kV.

X-ray diffraction patterns of sputtered Ge-Sb-Se-Te films confirmed that fabricated films are amorphous (fig. 2-16).

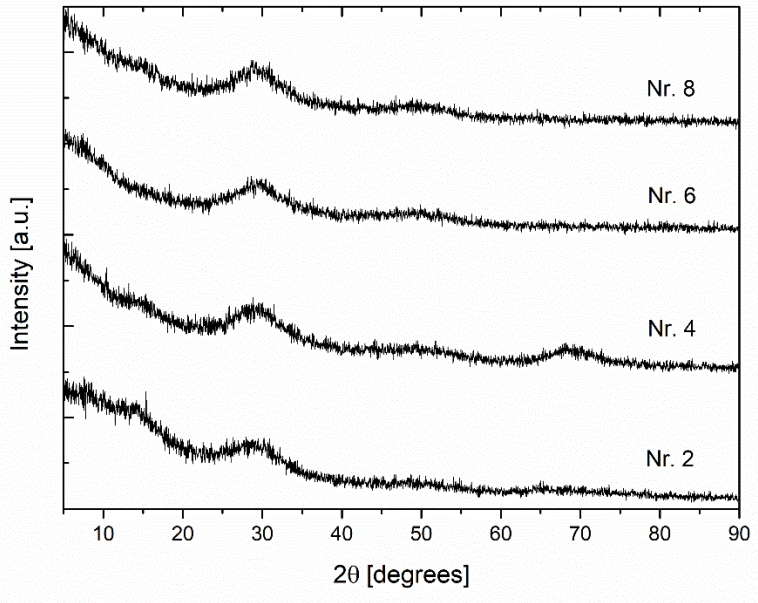

Fig. 2-16 XRD patterns of selected Ge-Sb-Se-Te samples – raw data taken in the range of *2θ* from 5 to 90° (with 0.026° step).

Table 2-6 The summary of deposition parameters of sputtered Ge-Sb-Se-Te thin films with their thicknesses determined from VASE (± 2 nm), deposition rate and chemical compositions (± 1 at. %) evaluated by EDS.

Nr	Power (W)	Argon pressure ($\times 10^{-3}$ mbar)	Thickness (nm)	Deposition rate ($nm \cdot min^{-1}$)	Composition (at. %)
1	10	5	690	11.4	$Ge_{22.5}Sb_{12.8}Se_{58.2}Te_{6.5}$
2	15	5	1270	21.1	$Ge_{22.2}Sb_{15.2}Se_{55.2}Te_{7.4}$
3	10	10	690	11.5	$Ge_{23.9}Sb_{14.6}Se_{54.9}Te_{6.6}$
4	15	10	1290	21.6	$Ge_{22.6}Sb_{14.1}Se_{56.7}Te_{6.6}$
5	10	5	790	13.2	$Ge_{23.6}Sb_{15.0}Se_{50.9}Te_{10.5}$
6	15	5	1460	24.3	$Ge_{23.5}Sb_{17.6}Se_{47.4}Te_{11.5}$
7	10	10	810	13.6	$Ge_{23.7}Sb_{14.6}Se_{50.9}Te_{10.8}$
8	15	10	1470	24.5	$Ge_{20.9}Sb_{17.2}Se_{49.5}Te_{12.4}$

The surface topography of Ge-Sb-Se-Te films is depicted in figures 2-17 and 2-18 for 2S1G-Se4-Te10 and 2S1G-Se-Te15 respectively. In the case of 2S1G-Se4-Te10 sputtered films, the surface topography does not seem to be affected significantly by the change of the argon pressure nor by electrical power. The RMS roughness of these films measured on 5 × 5 μm area is slightly higher at the argon pressure of 5×10^{-3} mbar (fig. 2-17a,b) – roughly ~0.3 nm at 5×10^{-3} mbar and ~0.15 nm at 10×10^{-3} mbar.

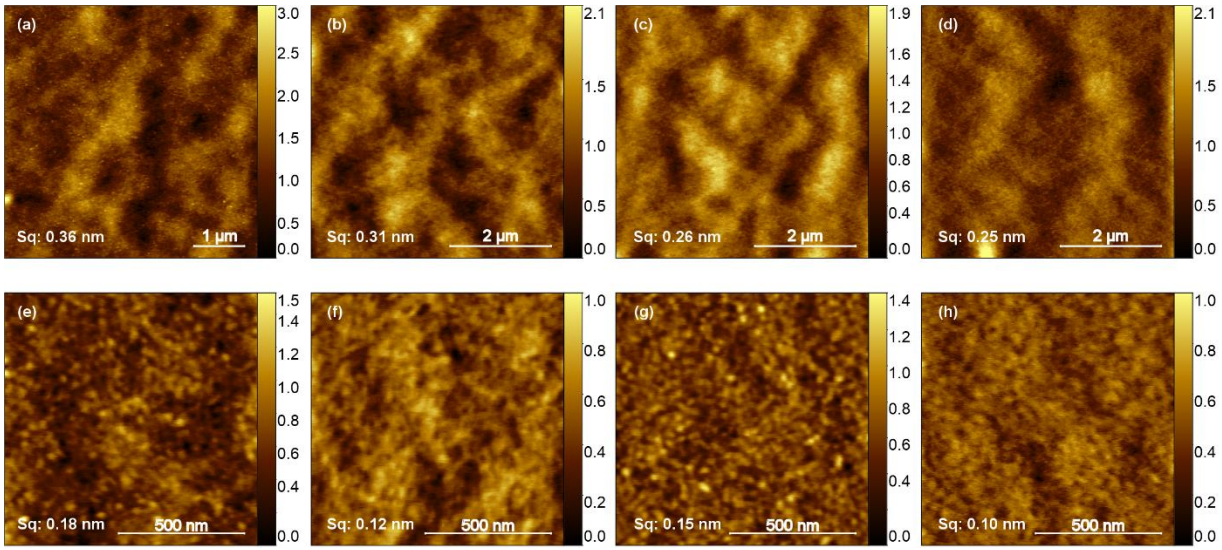

Fig. 2-17 AFM images of sputtered 2S1G-Se4-Te10 films with indicated root-mean squared roughness (Sq); **(a)** Nr. 1, 5×5 µm, **(b)** Nr. 2, 5×5 µm, **(c)** Nr. 3, 5×5 µm, **(d)** Nr. 4, 5×5 µm, **(e)** Nr. 1, 1×1 µm, **(f)** Nr. 2, 1×1 µm, **(g)** Nr. 3, 1×1 µm, **(h)** Nr. 4, 1×1 µm; values of z axis are in nanometres.

Sputtered films of 2S1G-Se4-Te15 exhibit rather different topography when compared to those deposited from 2S1G-Se4-Te10 target. The RMS roughness values are around Sq = 0.3 ± 0.1 nm for samples Nr. 5 – 7, and 0.5 ± 0.1 nm for sample number 8 when measured at 5×5 µm area. However, the surface topography was found to be grainier relative to films deposited from 2S1G-Se4-Te10 target.

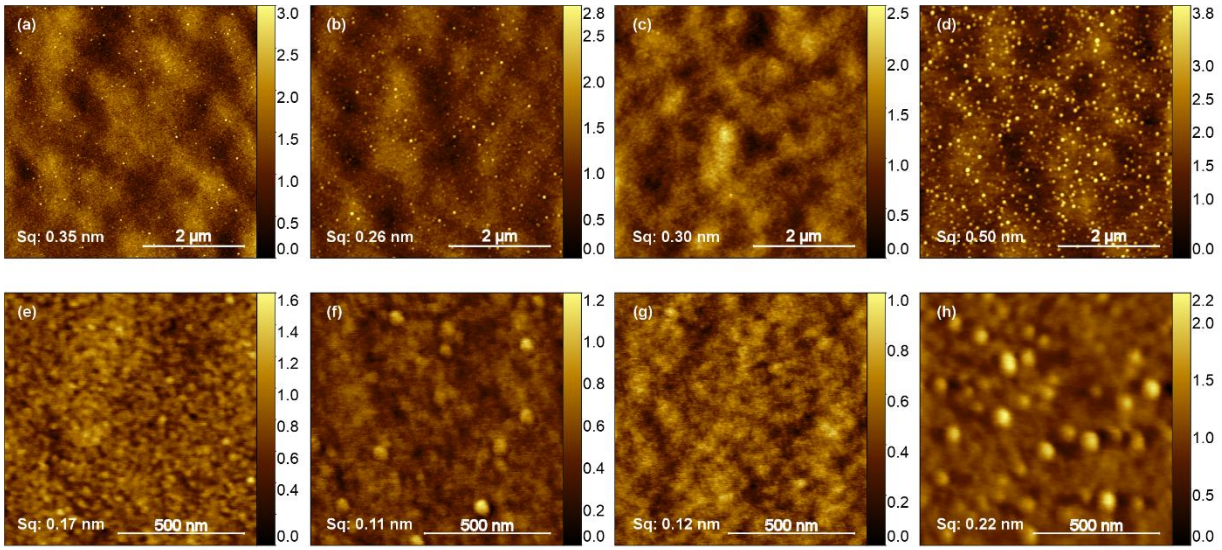

Fig. 2-18 AFM images of sputtered 2S1G-Se4-Te15 films with indicated root-mean squared roughness (Sq); **(a)** Nr. 5, 5×5 µm, **(b)** Nr. 6, 5×5 µm, **(c)** Nr. 7, 5×5 µm, **(d)** Nr. 8, 5×5 µm, **(e)** Nr. 5, 1×1 µm, **(f)** Nr. 6, 1×1 µm, **(g)** Nr. 7, 1×1 µm, **(h)** Nr. 8, 1×1 µm; values of z axis are in nanometers.

Optical properties of Ge-Sb-Se-Te thin films are summarized in table 2-7. Increase of argon pressure during the deposition process seems to affect the optical properties represented by optical bandgap energy (E_g^{CL}) and refractive index obtained from VASE measurements. The MSE values of about ~1 confirm a good fit of the measured data by CL model. Considering the accuracy of the VASE measurements being ± 0.02 for E_g^{CL} and ± 0.01 for *n*, the most important changes were observed for the films deposited from 2S1G-Se4-Te10 target. With an increased argon pressure from 5×10^{-3} mbar to 10×10^{-3} mbar, the optical bandgap decreased by approximately ~0.1 eV. A considerable increase of refractive index connected with the increase of argon pressure was also observed: ~0.1 for samples deposited at 10 W (sample Nr. 1 vs Nr. 3), and 0.07 for samples deposited at 15 W (sample Nr. 2 vs Nr. 4). In the case of samples sputtered from 2S1G-Se4-Te15 target, the observed changes are the opposite, *i.e.* the bandgap energy was increased with increasing argon pressure accompanied with the decrease in refractive index. It should be noted that in sputtered Ge-Sb-Se thin films, the drop of the refractive index reflects morphology changes generated by increased argon pressure [31].

Table 2-7 The summary of deposition parameters of sputtered Ge-Sb-Se-Te thin films with their chemical compositions (± 1 at. %) evaluated by EDS, mean-squared error (MSE) values of VASE data fits, optical bandgap energy E_g^{CL} (± 0.02 eV) and refractive index at 1.55 μm (± 0.01).

Nr	Power (W)	Argon pressure ($\times10^{-3}$ mbar)	Composition (at. %)	MSE	E_g^{CL}(eV)	*n* @1.55 μm
1	10	5	$Ge_{22.5}Sb_{12.8}Se_{58.2}Te_{6.5}$	0.79	1.46	2.81
2	15	5	$Ge_{22.2}Sb_{15.2}Se_{55.2}Te_{7.4}$	0.99	1.46	2.84
3	10	10	$Ge_{23.9}Sb_{14.6}Se_{54.9}Te_{6.6}$	1.11	1.34	2.91
4	15	10	$Ge_{22.6}Sb_{14.1}Se_{56.7}Te_{6.6}$	1.47	1.37	2.91
5	10	5	$Ge_{23.6}Sb_{15.0}Se_{50.9}Te_{10.5}$	0.70	1.27	2.97
6	15	5	$Ge_{23.5}Sb_{17.6}Se_{47.4}Te_{11.5}$	0.90	1.26	3.00
7	10	10	$Ge_{23.7}Sb_{14.6}Se_{50.9}Te_{10.8}$	0.64	1.32	2.93
8	15	10	$Ge_{20.9}Sb_{17.2}Se_{49.5}Te_{12.4}$	1.05	1.28	2.94

Concluding remarks

Thin films of amorphous Ge-Sb-Se and Ga-Sb-Se fabricated by co-sputtering technique were found to be of good optical quality with surface roughness (RMS) typically around ~0.3 ± 0.2 nm and ~0.2 ± 0.1 nm respectively. The optical bandgap energies E_g^{CL} range 1.35-2.09 eV with corresponding refractive index ranging from 3.34 to 2.38 can be reliably covered in Ge-Sb-Se ternary system, when targets with compositions of Sb_2Se_3 (E_g^{CL} = 1.35 eV), $GeSe_2$ (E_g^{CL} = 2.09 eV), $GeSe_4$ (E_g^{CL} = 1.97 eV) and $Ge_{28}Sb_{12}Se_{60}$ (E_g^{CL} = 1.68 eV) are used (fig. 2-9). For Ga-Sb-Se co-sputtered films, the range of E_g^{CL} 1.35-1.92 eV and corresponding refractive index range of 3.34-2.47 is also decently covered, though the deposition rate of Ga_2Se_3 is significantly lower than that of Sb_2Se_3. In both ternary systems, the introduction of heavy antimony atoms is responsible for the decrease of optical bandgap energy accompanied with corresponding increase of refractive index due to its high polarizability.

Sputtered Ge-Sb-Se-Te films, where the selenium is only partially altered by tellurium (10 and 15 at. %) relative to Se-rich Ge-Sb-Se films mentioned above, were also studied. Despite

the fact that the surface roughness (RMS) of most of the prepared samples was only around ~0.3 ± 0.1 nm, thin films with higher tellurium content seem to be much grainier by means of topography. The studies of optical properties of sputtered films revealed expected drop of optical bandgap energy accompanied by increase of refractive index relative to tellurium-free Ge-Sb-Se films. The introduction of heavy tellurium provides the higher polarizability increasing the refractive index.

3. Nonlinear optical properties

The nonlinear refractive index n_2 and 2PA coefficient β at the wavelength of 1.55 μm were calculated by Sheik-Bahae's formulae [32] given in the first chapter (eq. 2-10 and 2-12 respectively). This approach was chosen for its relative simplicity when the linear refractive index dispersion and the optical bandgap are used. The dispersion curves and optical bandgap energies of thin films were obtained from the VASE data analysis. Taking in account the uncertainty of VASE measurements together with the mean absolute deviation from the Miller's rule (eq. 3-1), considered accuracy of these calculations in about ~13 %. The figure of merit (FOM), calculated by eq. 2-24 given in chapter one, was used for the assessment of the applicability of prepared films in the field of nonlinear optics.

3.1. Nonlinear optical properties of Ge-Sb-Se thin films

Nonlinear refractive index (n_2) at the 1.55 μm depending on the optical bandgap for all Ge-Sb-Se thin films prepared in this work are shown in the fig. 3-1. As seen, the values of n_2 cover the range from 3.74×10^{-18} m^2W^{-1} for antimony-free $GeSe_2$ up to 2.27×10^{-17} m^2W^{-1} for the sample Nr. 3 ($Ge_{5.0}Sb_{33.4}Se_{61.6}$). However, high value of n_2 in combination with low value of optical bandgap leads to the high two-photon absorption (2PA) at desired wavelength as seen in the figure 3-2. It should be noted that As_2Se_3 thin film deposited under the same conditions as all the other films (with electrical power applied of 10 W) is used as a reference. Calculated value of n_2 for As_2Se_3 is 9.03×10^{-18} m^2W^{-1} at 1.55 μm and is in a good agreement with value of nonlinear refractive index reported by Quémard *et al.* (n_2 at 1.43 μm is 1×10^{-17} m^2W^{-1}) and also with value of n_2 reported by Dai et al. (n_2 at 1.55 μm is 1×10^{-17} m^2W^{-1}) for 1 mm bulk glass discs [33, 34]. A good agreement with the value of n_2 at 1.5 μm reported by Lenz *et al.* was also found in case of $Ge_{28}Sb_{12}Se_{60}$ bulk glass. Reported experimental value is 11.31×10^{-18} m^2W^{-1}, which is close to the calculated value of 12.3×10^{-18} m^2W^{-1} at this wavelength [35]. For $GeSe_4$ thin film (sample Nr. 17), the n_2 at 1.06 μm was found to be 7.91×10^{-18} m^2W^{-1}. This value is somewhat lower than the one reported by Smektala *et al.* for 1 mm thick bulk glass using the z-scan technique at 1.064 μm being 13×10^{-18} m^2W^{-1} [36]. It should be noted that the evolution of n_2 on optical bandgap energy clearly copies the shape of function G_2.

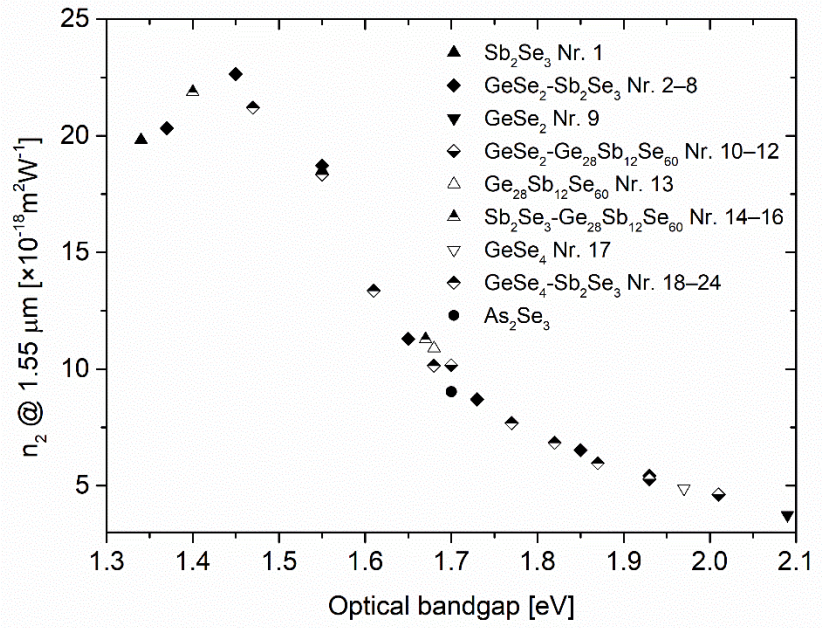

Fig. 3-1 Dependence of nonlinear refractive index at the telecommunication wavelength on the optical bandgap of Ge-Sb-Se thin films.

The utmost value of 2PA coefficient β is found for thin film of Sb_2Se_3 as seen in the figure 3-2. Moreover, for co-sputtered Ge-Sb-Se thin films β equals to zero for all the samples having the optical bandgap energy (E_g^{CL}) higher than 1.61 found for the sample Nr. 22 ($Ge_{7.4}Sb_{24.5}Se_{68.1}$). Corresponding linear refractive index (n_0) at 1.55 μm for this sample is 2.86. The value of nonlinear refractive index of this sample n_2 at 1.55 μm is 1.34×10^{-17} m^2W^{-1}.

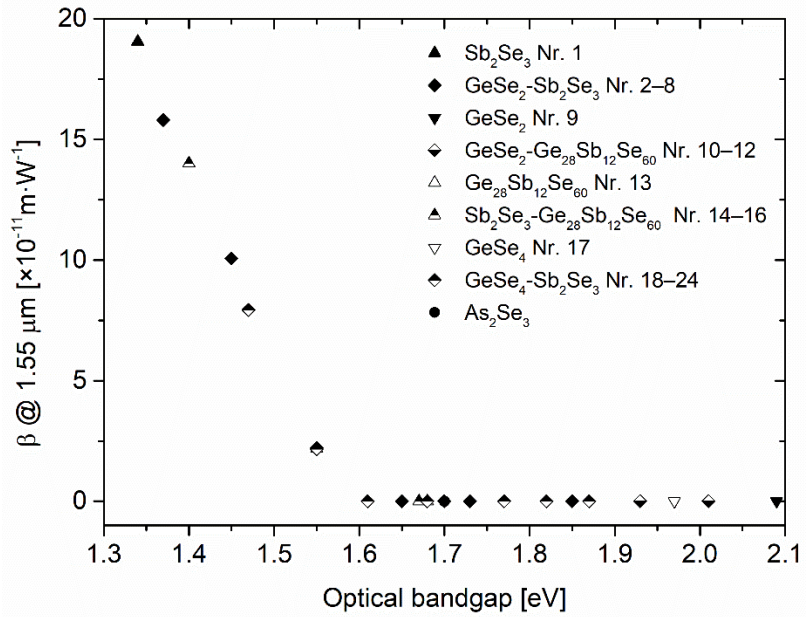

Fig. 3-2 Dependence of 2PA coefficient β at the telecommunication wavelength on the optical bandgap of Ge-Sb-Se thin films.

As depicted in the figure 3-3, calculated data of nonlinear refractive index for co-sputtered films are in a good agreement with data measured by Wang *et al.* who performed z-scan measurements at 1.55 μm within Ge-Sb-Se bulk glasses of thickness of ~2 mm [37]. Similarly, the values of n_2 are close to the data reported by Olivier *et al.* for bulk glasses of ~2 mm

thickness measured by beam self-trapping technique at 1.55 μm [8]. The data reported by Kuriakose *et al.* for Ge-Sb-Se slab waveguides measured by the same technique at 1.55 μm [27] give a little bit higher values of n_2. Furthermore, calculated data given in figure 3-3 are in a good agreement with semi-empirical Miller's rule expressed as:

$$n_2 = 4.27 \times 10^{-20} \frac{(n_0^2 - 1)^4}{n_0^2} \ m^2 W^{-1}$$

Eq. 3-1

Tichá and Tichý [38] reported some values of n_2 for bulk Ge-Sb-Se glasses calculated by generalized Miller rule corresponding to n_0 at $\lambda \rightarrow \infty$. Their data in esu units were converted to SI units in figure 3-3 by simple relationship $n_2[SI] = (40\pi/(cn_0) \cdot n_2[esu]$.

Moreover, Dai *et al.* reported nonlinear refractive index z-scan measurements at telecommunication wavelength for some 1 mm Ge-Sb-Se bulk glasses [33]. Despite small differences in the composition, relatively good agreement was found for some comparable samples. For example, for $Ge_{25}Sb_{10}Se_{65}$ bulk glass which is close to the thin film Nr. 7 ($Ge_{23.4}Sb_{11.5}Se_{65.1}$), the nonlinear refractive index n_2 is 6.5×10^{-18} m^2W^{-1} (vs 5.4×10^{-18} m^2W^{-1} calculated for sample Nr. 7). For $Ge_{15}Sb_{20}Se_{65}$ the reported value is 7.4×10^{-18} m^2W^{-1}, which is close to 6.5×10^{-18} m^2W^{-1} calculated for sample Nr. 6 ($Ge_{16.4}Sb_{19.4}Se_{64.2}$).

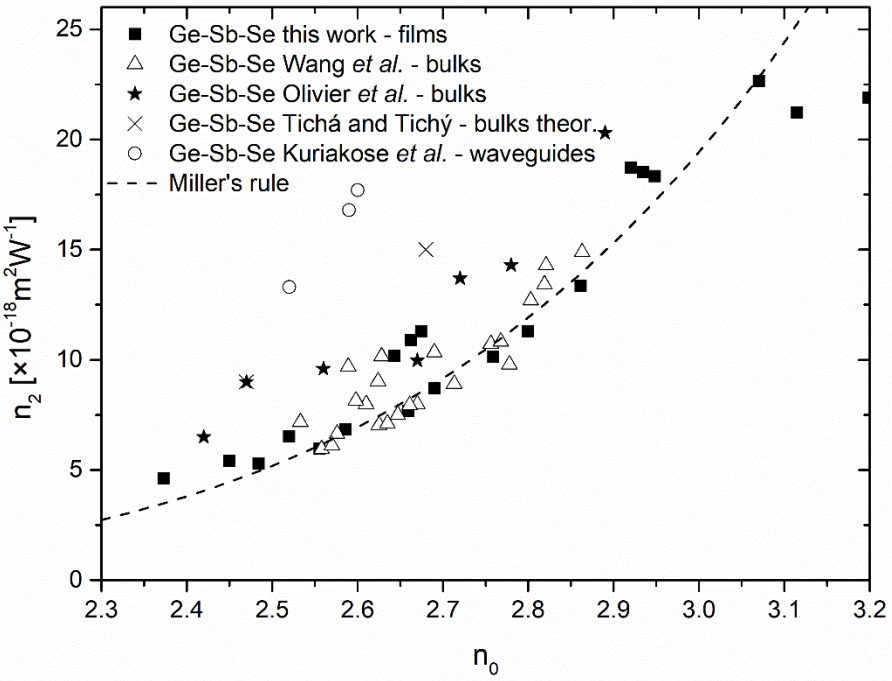

Fig. 3-3 Comparison of nonlinear refractive index n_2 at 1.55 μm of Ge-Sb-Se co-sputtered thin films calculated using Sheik-Bahae's model with experimental data taken from Wang *et al.* (z-scan measurements of bulk glasses with thickness of ~2 mm) at 1.55 μm [37], from Olivier *et al.* (beam self-trapping measurements of bulk glasses of ~2 mm) at 1.55 μm [8], from Kuriakose *et al.* (beam self-trapping measurements of Ge-Sb-Se slab waveguides) at 1.55 μm [27], theoretical values of n_2 (calculated by generalized Miller rule by Tichá and Tichý for Ge-Sb-Se bulk glasses) at $\lambda \rightarrow \infty$ [38] and semi-empirical Miller's rule by Eq. 3-1.

Figure 3-4 shows the FOM (eq. 2-24 in chapter 1) calculated for all co-sputtered films. It confirms that the films with the linear refractive index higher than that of sample Nr. 22

($Ge_{7.4}Sb_{24.5}Se_{68.1}$) may be limited for the application in nonlinear optics at the telecommunication wavelength, *i.e.* FOM for these films at 1.55 μm is higher than 1.

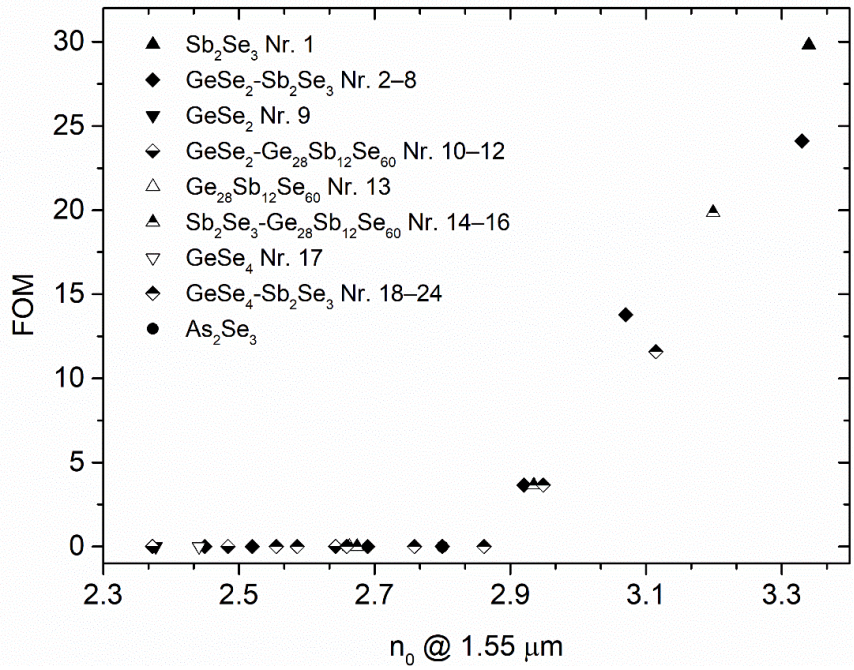

Fig. 3-4 Dependence of FOM on the linear refractive index (n_0) at 1.55 μm of Ge-Sb-Se thin films

3.2. Nonlinear optical properties of Ga-Sb-Se thin films

In Ga-Sb-Se system, co-sputtered films corresponding to Ga_2Se_3-Sb_2Se_3 pseudo-binary were considered for nonlinear optics applications. Nonlinear refractive indices (n_2) at the 1.55 μm depending on the optical bandgap for all fabricated thin film samples are shown in the figure 3-5. The values of n_2 ranges from 5.50×10^{-18} m^2W^{-1} for antimony-free Ga_2Se_3 up to 2.09×10^{-17} m^2W^{-1} for the sample Nr. 8 ($Ga_{7.6}Sb_{31.2}Se_{61.2}$) as depicted in the figure 3-5. 2PA coefficient $ß$ for co-sputtered Ga-Sb-Se films reaches zero (fig. 3-6) for samples having optical bandgap E_g^{CL} higher than 1.65 eV corresponding to sample Nr. 4 ($Ga_{19.2}Sb_{17.5}Se_{63.3}$). The linear refractive index of this sample (n_0) at 1.55 μm is 2.80.

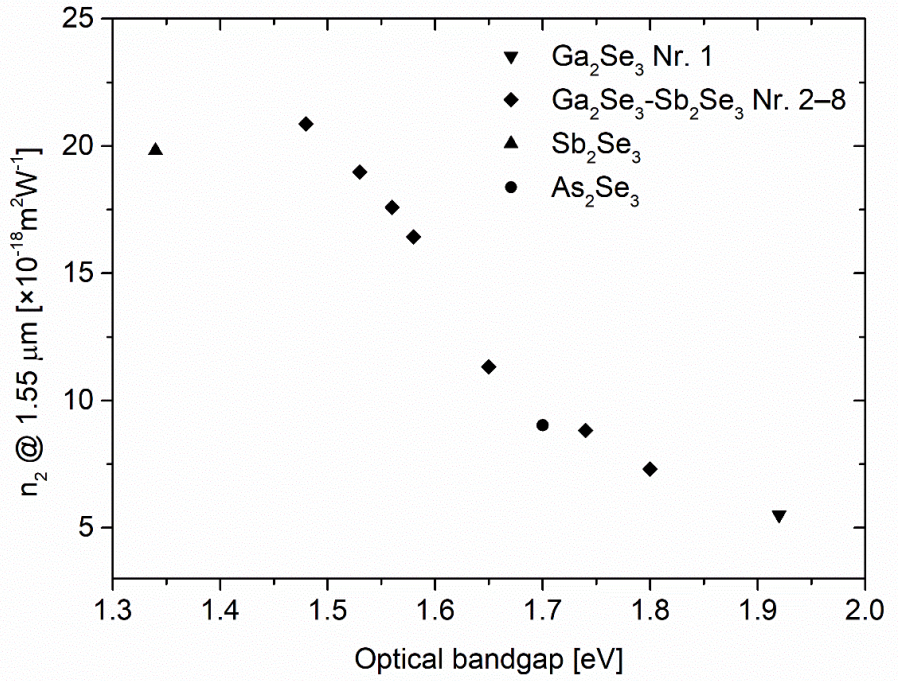

Fig. 3-5 Dependence of nonlinear refractive index at the telecommunication wavelength on the optical bandgap of Ga-Sb-Se thin films.

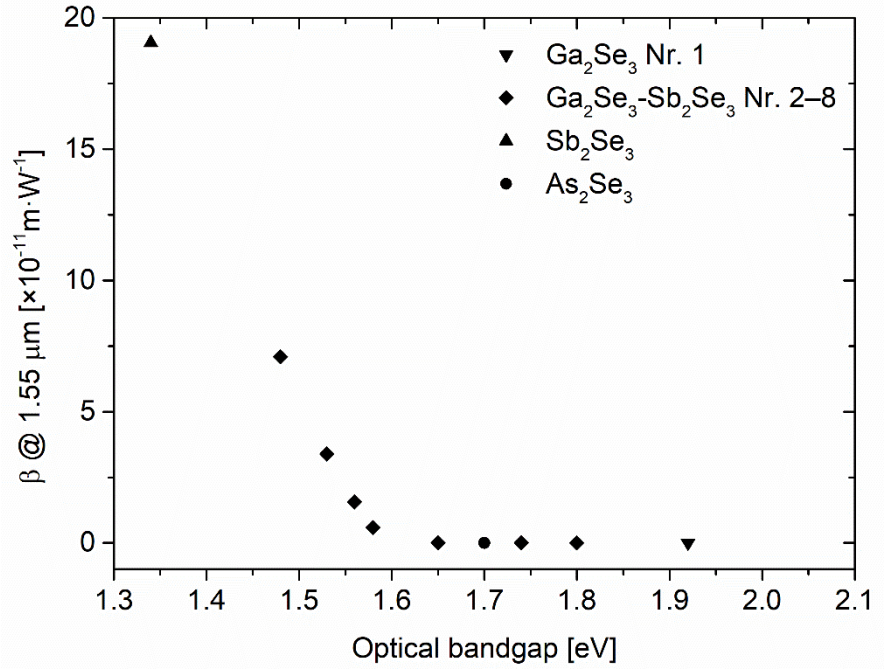

Fig. 3-6 Dependence of 2PA coefficient β at the telecommunication wavelength on the optical bandgap of Ga-Sb-Se thin films.

The suitability of co-sputtered Ga-Sb-Se thin films in nonlinear optics represented by means of FOM (fig. 3-7) is very similar to that of Ge-Sb-Se system. This makes the ternary system of Ga-Sb-Se an interesting option to Ge-Sb-Se especially when one compares the current market price of gallium when compared to germanium [11].

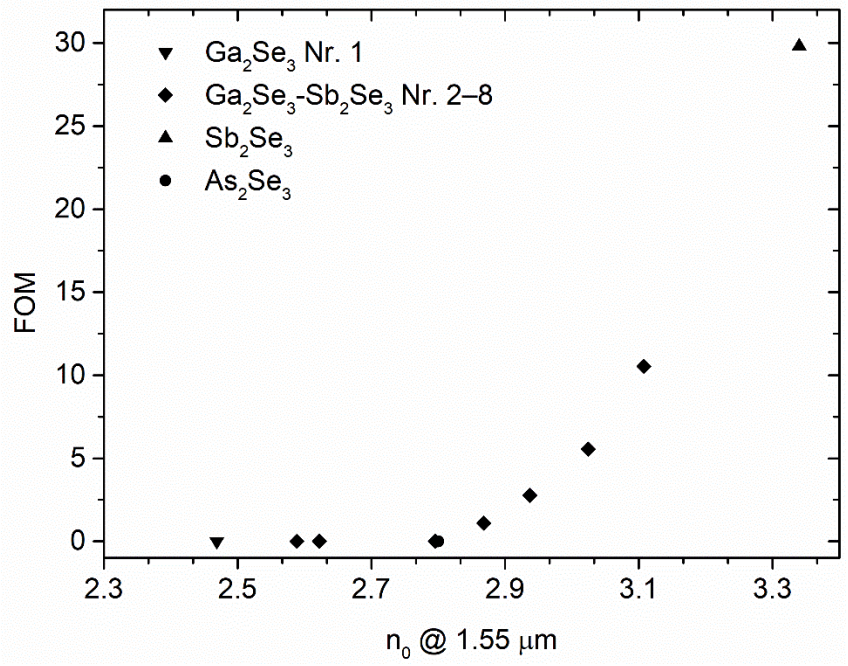

Fig. 3-7 Dependence of FOM on the linear refractive index (n_0) at 1.55 μm of Ga-Sb-Se thin films.

3.3. Nonlinear optical properties of Ge-Sb-Se-Te thin films

The nonlinear refractive index against the optical bandgap for Ge-Sb-Se-Te system is plotted in the figure 3-8. The values of nonlinear refractive index are higher than those of Ge-Sb-Se system (~2.1-2.6 m^2W^{-1}). However, the low optical bandgap values E_g^{CL} lead to the considerably high 2PA coefficient β (fig. 3-9) which may reach more than ~30 × 10^{-11} $m \cdot W^{-1}$ (~0.3 $cm \cdot GW^{-1}$) for 2S1G-Se4-Te15 sputtered films. Unfortunately, this fact confirmed also by high FOM (fig. 3-10) makes Ge-Sb-Se-Te films considerably ineffective for the applications in nonlinear optics at the telecommunication wavelengths. Furthermore, the evolution of n_2 depending on optical bandgap energy (fig. 3-8) clearly does not copy the shape of the function G_2 as it is for co-sputtered Ge-Sb-Se and Ga-Sb-Se thin films. This may be caused by the small differences in n_0 and E_g^{CL} used for the calculations so the range of n_2 is rather small when compared to the previous studied films.

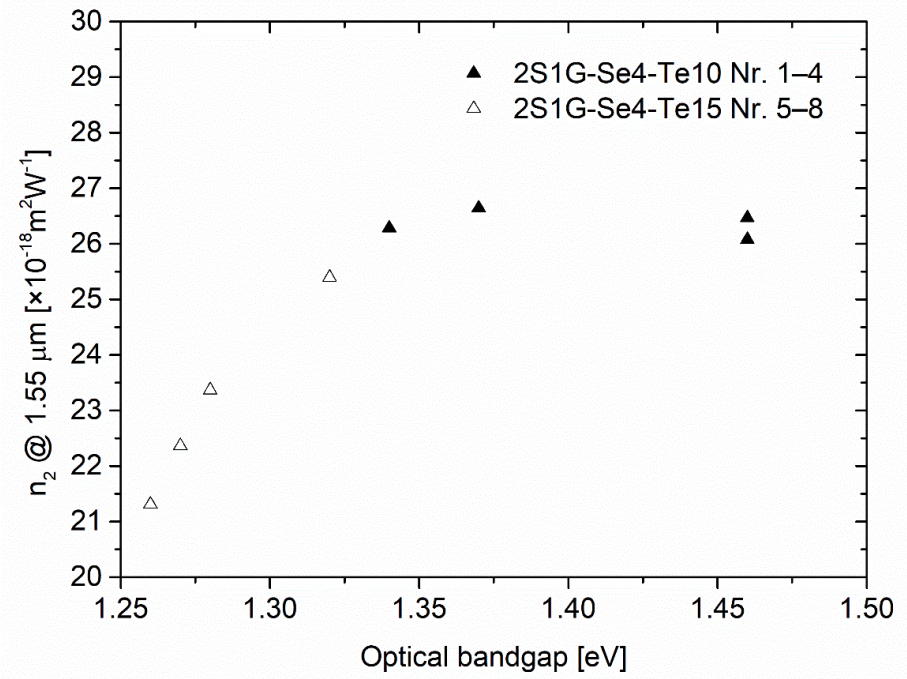

Fig. 3-8 Dependence of nonlinear refractive index at the telecommunication wavelength on the optical bandgap of Ge-Sb-Se-Te thin films.

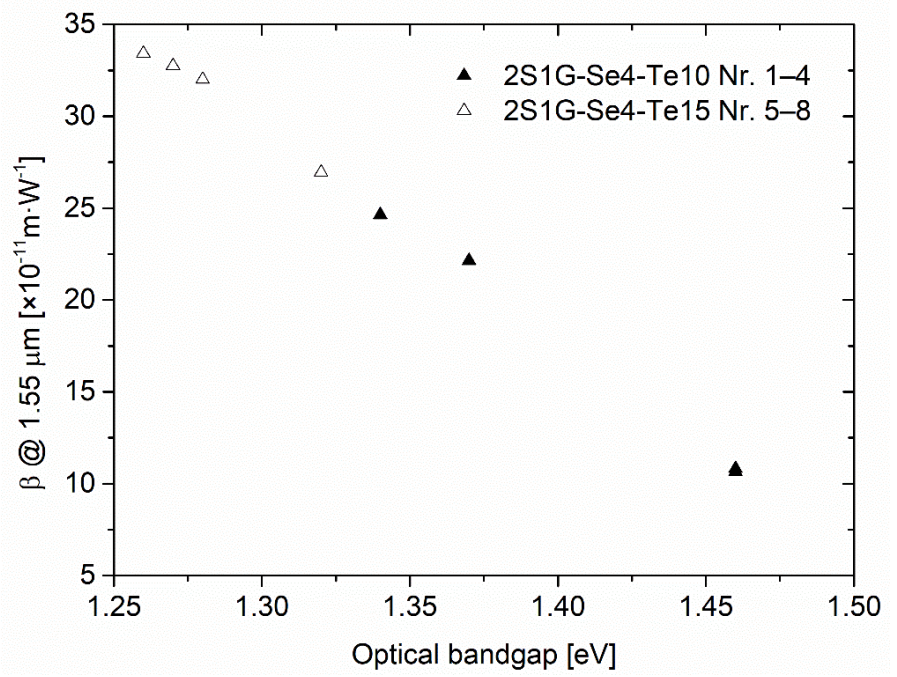

Fig. 3-9 Dependence of 2PA coefficient β at the telecommunication wavelength on the optical bandgap of Ge-Sb-Se-Te thin films.

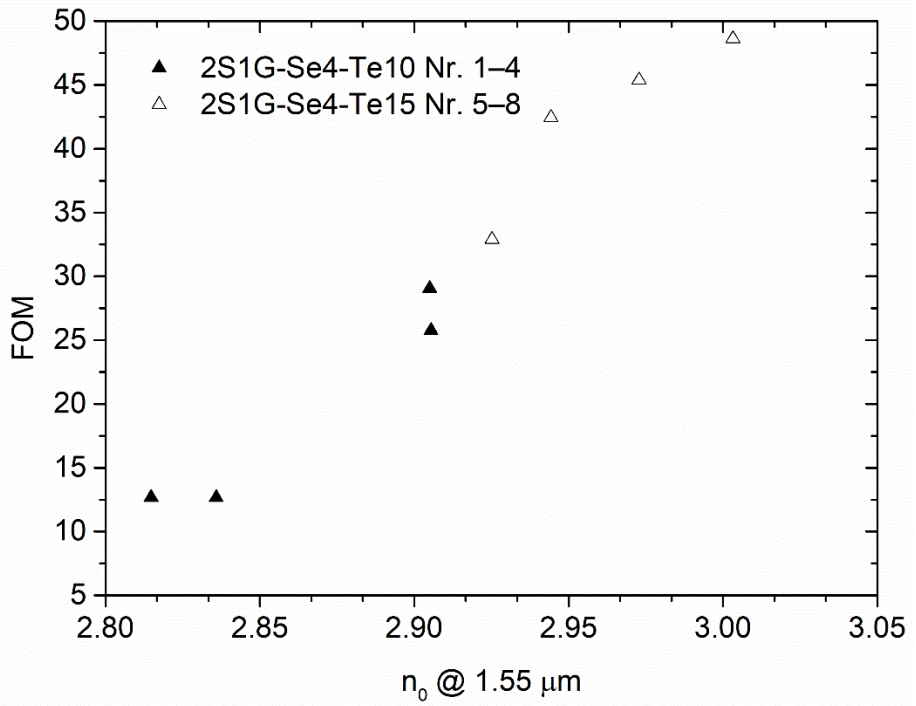

Fig. 3-10 Dependence of FOM on the linear refractive index (n_0) at 1.55 μm of Ge-Sb-Se-Te thin films.

Concluding remarks

Nonlinear optical properties of co-sputtered ternary Ge-Sb-Se and Ga-Sb-Se and sputtered quaternary Ge-Sb-Se-Te films were studied by means of nonlinear refractive index (Kerr coefficient) n_2 and two-photon absorption (2PA) coefficient β. Numerical calculations of these coefficients were estimated by Sheik-Bahae's formalism [32] using the ellipsometry data (dispersion curves and optical bandgap energy E_g^{CL}). The balance between the refractive index and optical bandgap seems to be very important since the optical losses due to the large two-photon absorption can represent the limitation of a material for applications in nonlinear optics at desired wavelengths. For ternary Ge-Sb-Se and Ga-Sb-Se co-sputtered films, the value of optical bandgap energy of at least ~1.60 eV with corresponding refractive index at 1.55 μm around ~2.80 seems to be limit value for possible applications at telecommunication wavelength. This is in a suitable accordance with Tanaka who proposed materials with the Tauc gap of ≈ 1.80 eV as a best choice for nonlinear optical fibers [39]. The limiting calculated values of n_2 at 1.55 μm according this work are between ~1.13-1.34 × 10^{-17} m^2W^{-1}. These values are more than three orders of magnitude larger than that of silica (n_2 ~ 3 × 10^{-20} m^2W^{-1}) [40]. It should be noted that calculated values of n_2 using Sheik-Bahae's model for Ge-Sb-Se sputtered films are in a very good agreement with the literature.

Furthermore, high two-photon absorption may be expected in Ge-Sb-Se-Te films fabricated by sputtering. The alteration of selenium by tellurium in such system causes high decrease in optical bandgap which gives rise to high values of 2PA coefficient at 1.55 μm.

4. Local structure of thin films by Raman scattering spectroscopy

The local structure of deposited films was studied using micro-Raman spectroscopy (LabRam HR800, Horiba Jobin-Yvon, NJ, USA) coupled with a ×100 microscope (Olympus, JP) with the excitation wavelength of 785 nm. In order to prevent the sample heating, neutral density filters were used to attenuate the laser intensity. The effect of thermal population at low wavenumbers was minimized by the reduction of Raman intensity defined in [41] as $I_{red}(\omega) = I_{meas}(\omega) \cdot \omega/[n(\omega)+1]$, where $I_{meas}(\omega)$ represents the experimental Raman intensity at a frequency ω and $n(\omega)$ is the Bose-Einstein temperature occupation factor for the Stokes shift, given by $n(\omega) = (\exp[(\hbar\omega/k_B T) - 1])^{-1}$. Here, $\hbar$ is a reduced Planck constant, k_B is a Boltzman constant and T is a temperature. After the reduction, the spectra were normalized by means of the division by the maximum.

4.1. Local structure of Ge-Sb-Se thin films

First, the local structure of thin films fabricated by co-sputtering from $GeSe_2$-Sb_2Se_3 (fig. 4-1), $GeSe_2$-$Ge_{28}Sb_{12}Se_{60}$ and Sb_2Se_3-$Ge_{28}Sb_{12}Se_{60}$ (fig. 4-2) pseudo-binaries is discussed. The influence of irradiation on Raman spectra of as-deposited co-sputtered thin films will be discussed in chapter 5.

For germanium rich films, Raman bands peaking at ~198 and ~216 cm^{-1} dominate the spectra. These are ascribed to the symmetric stretching vibrations of heteropolar Ge–Se bonds in corner-sharing (A_1) and edge-sharing (accompanion mode, A_1^C) [$GeSe_{4/2}$] tetrahedra [9, 42-44]. Furthermore, Raman bands corresponding to stretching vibration modes of Ge–Ge homopolar bonds in [$Ge_2Se_{6/2}$] and [Ge–Ge_mSe_{4-m}] (m=1, 2, 3, 4) entities are found at ~175 cm^{-1} accompanied by a small contribution at ~270 cm^{-1} [45].

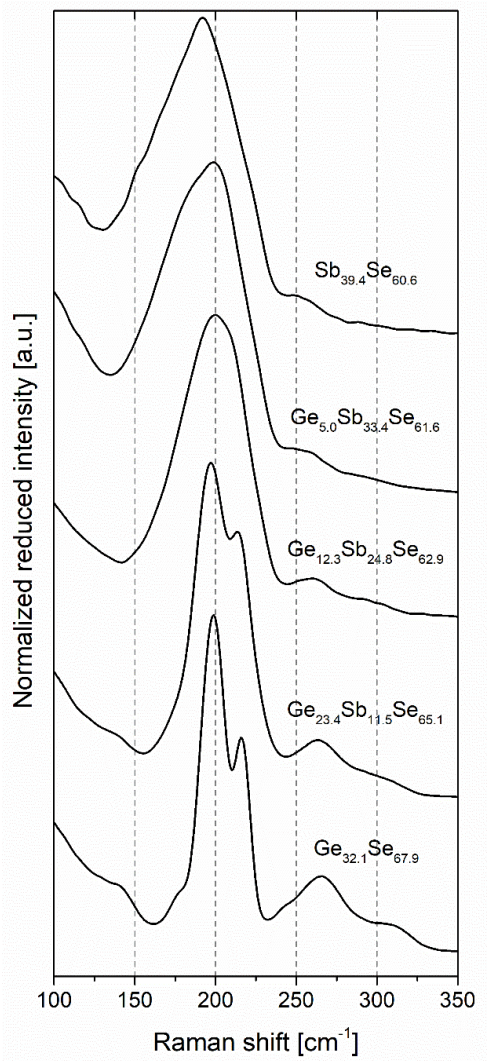

Fig. 4-1 Raman spectra of Ge-Sb-Se co-sputtered thin films ($GeSe_2$ and Sb_2Se_3 targets) with indicated compositions – samples shown in the plot correspond to the samples in table 2-1 – from top Nr. 1, 5, 3, 7 and Nr. 9.

It should be noted that the Raman band assigned to Ge–Ge vibrations at ~175 cm^{-1} becomes more significant when the $Ge_{28}Sb_{12}Se_{60}$ target is involved. This can be seen from the spectra of samples Nr. 11, 13 and 14 which are shown in the figure 4-2. However, it is not the case for $GeSe_2$ and Sb_2Se_3 respecting the stoichiometry of the main [$GeSe_{4/2}$] and [$SbSe_{3/2}$] entities forming the glass network. For the films where the higher electrical power (*e.g.* spectra of sample Nr. 9 in fig. 4-1 or spectra of sample Nr. 10 in fig. 4-2) was applied onto the cathode with $GeSe_2$ target, the content of Ge–Ge homopolar bonds was not found to be as significant as for $Ge_{28}Sb_{12}Se_{60}$ target presenting a deficit in Se. Creation of more favourable heteropolar bonds during the deposition process is expected in these films due to the higher selenium content [4].

With the decreasing germanium concentration, symmetric stretching vibrations of corner-sharing (A_1) and edge-sharing (A_1^C) [$GeSe_{4/2}$] tetrahedra typical for Ge-rich films gradually evolve to Sb–Se stretching vibration modes in [$SbSe_{3/2}$] pyramidal units, resulting in the broad, high-intensity Raman band peaking at ~190 cm^{-1} in stoichiometric Sb_2Se_3films [42, 46].

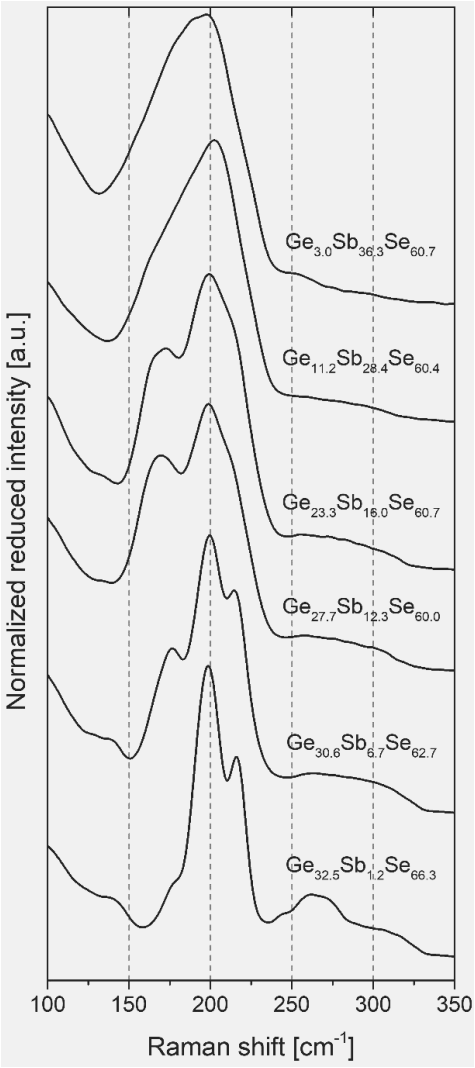

Fig. 4-2 Raman spectra of Ge-Sb-Se co-sputtered thin films ($GeSe_2$ or Sb_2Se_3 combined with $Ge_{28}Sb_{12}Se_{60}$ target) with indicated compositions – samples shown in the plot correspond to the samples in table 2-1 – from top Nr. 16, 15, 14, 13, 11 and Nr. 10.

Apart from weak Raman band at ~270 cm^{-1}, other contributions can be found in the stretching vibrational region between ~250 and 330 cm^{-1}. First, Se–Se stretching mode at the outrigger is located at ~245 cm^{-1} [47]. Furthermore, a contribution which is considered to originate from Se–Se vibrations at ~265 cm^{-1} coming from [$GeSe_{4/2}$] tetrahedra where at least one of the selenium atoms at the tetrahedron corner is bonded to another one, forming Se–Se dimers or short selenium chains (Se_n) [45]. Finally, F_2 asymmetric vibration modes of $GeSe_4$ tetrahedra are found at ~305 cm^{-1} [48]. The weak band, usually ascribed to Se–Se bending mode vibrations, can be identified at ~136 cm^{-1} [49].

It can be seen, that the low-intensity Raman band found in stoichiometric Sb_2Se_3 films at ~249 cm^{-1} assigned to Se–Se bond stretching vibrations in short selenium chains, shifts towards the higher wavenumbers with increasing germanium content [9]. For Sb-rich samples, the low intensity Raman band with maximum at ~159 cm^{-1} assigned to Sb–Sb homopolar bonds' vibrations in the Se_2Sb-$SbSe_2$ units can be found [4, 48].

In the case of thin films co-sputtered from $GeSe_4$-Sb_2Se_3 pseudo-binary system (figure 4-3), Raman peak corresponding to the edge-sharing (A_1^C) [$GeSe_{4/2}$] tetrahedra vibrational modes (~216 cm^{-1}) is much less intense when compared to the films co-sputtered from $GeSe_2$-Sb_2Se_3 pseudo-binary. Furthermore, high-intensity peak considered to be coming from Se–Se dimers

or short selenium chains (Se_n) can be found at ~260 cm^{-1}. By means of the structure, it can be assumed that the lower intensity of edge-sharing [$GeSe_{4/2}$] tetrahedra vibrational modes is caused by the creation of Se–Se dimers and short selenium chains due to the large selenium content [50]. Moreover, Ge–Ge vibrations at ~175 cm^{-1} cannot be identified from Raman spectra of these films indicating that almost all of the germanium atoms are probably connected to selenium atoms. Similarly, the peak at ~305 cm^{-1} has very low intensity when compared to the films co-sputtered using $GeSe_2$ and Sb_2Se_3 targets. The evolvement of Sb–Se stretching vibration modes in [$SbSe_{3/2}$] pyramidal units with increasing antimony content was also found in these films.

To illustrate an assignment of bands identified in the Raman spectra, it is plausible to give an example of spectra decomposition procedure for sputtered $GeSe_2$ and $Ge_{28}Sb_{12}Se_{60}$ films exploiting different number of Gaussians (fig. 4-4). The complete assignment of vibrational modes observed in the Raman spectra of Ge-Sb-Se co-sputtered films is given in table 4-1.

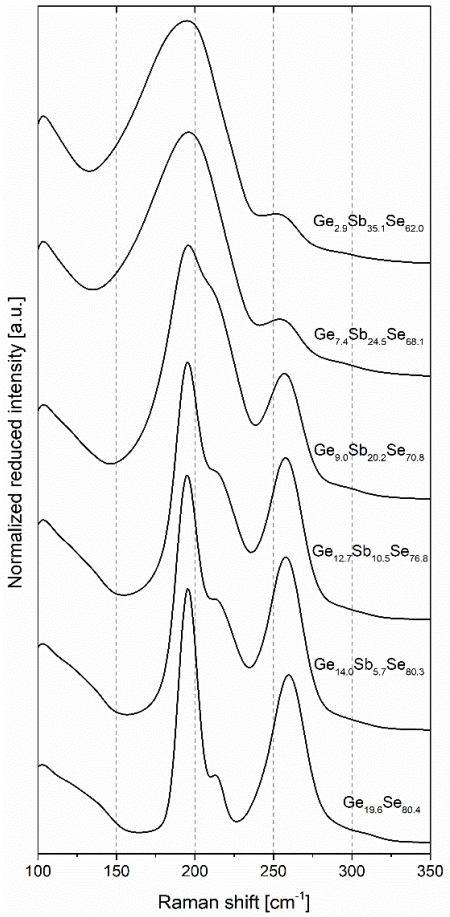

Fig. 4-3 Raman spectra of Ge-Sb-Se co-sputtered thin films ($GeSe_4$ and Sb_2Se_3 targets) with indicated compositions – samples shown in the plot correspond to the samples in table 2-2 – from top Nr. 24, 22, 21, 19, 18 and Nr. 17.

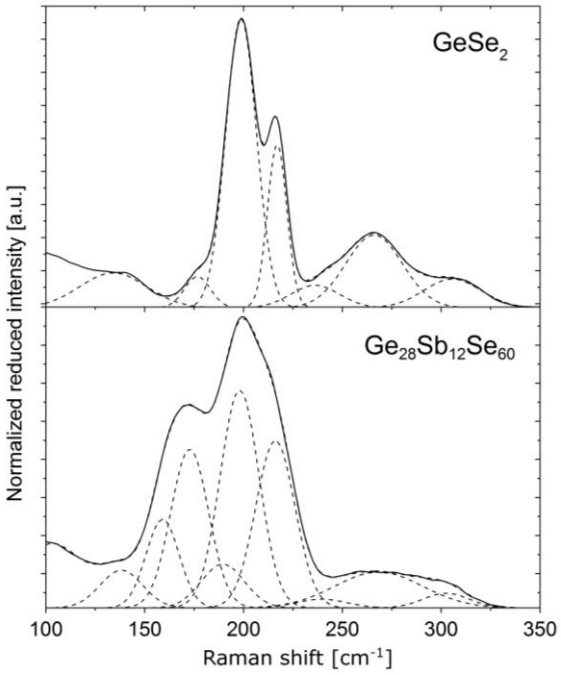

Fig. 4-4 Gaussian peaks decomposition of Raman spectra of $GeSe_2$ (top panel) and $Ge_{28}Sb_{12}Se_{60}$ thin films sputtered at 10 W – from Halenkovič *et al.* [4].

Table 4-1 Contributions of different structural entities to Raman scattering spectra in Ge-Sb-Se glasses and thin films

Wavenumber (cm^{-1})	Vibrational mode	Environment	Reference
138	rotational	Se polymeric chains	[8, 51]
138-145	bending	Se–Se at the outrigger	[49]
159	Sb–Sb	Se_2Sb-$SbSe_2$	[52, 53]
175 270	Ge–Ge	$[Ge_2Se_{6/2}]$ $[Ge–Ge_mSe_{4-m}]$ m=1, 2, 3, 4	[8, 54, 55]
190	Sb–Se stretching	$[SbSe_{3/2}]$ pyramidal units	[8, 52]
198	A_1 symmetric stretching	$[GeSe_{4/2}]$ connected by corner	[47, 53, 55]
216	A_1^C breathing companion	$[GeSe_{4/2}]$ connected by edge	[47, 54, 55]
235	A_1	Se_n chains in amorphous Se	[8, 51]
245	stretching mode	Se–Se at the outrigger	[47]
240-250	A_1	Se_n rings	[8, 51, 53]
260-265	A_1	Se_n chains $[GeSe_{4/2}]$ corner linked (dimers, short chains)	[8, 47, 53] [8, 56]
285-305	F_2 asymmetric	$GeSe_4$	[4, 47, 57]

4.2. Local structure of Ga-Sb-Se thin films

It is generally proposed that gallium atoms are four-fold coordinated in the glass network having similar structure as that of germanium based chalcogenide glasses, *i.e.* tetrahedral coordination of gallium [58]. However, the structure of these glasses still remains unclear [11].

Raman spectrum of single cathode deposited Ga_2Se_3 shows clearly more peaks when compared to its crystalline counterpart which is dominated by sharp peak at ~155 cm^{-1} and two broad peaks at 250 and 300 cm^{-1}, [59, 60]. Raman spectra of Ga-Sb-Se thin films are shown in the figure 4-5. The dominant peak at ~169 cm^{-1} was found in the spectrum of Sb-free sample. With increasing Sb content, the intensity of this peak is reduced and shifted towards the higher wavenumbers. Interestingly, similar behaviour was reported by Verger *et al.* for Ge-Sb-Se glasses where the high intensity peak at ~170 cm^{-1} ascribed to the stretching vibration modes of Ge–Ge bonds in $[Ge_2Se_{6/2}]$ or $[Ge_{x/4}–Ge–Se_{(4-x)/2}]$ found in $Ge_{38}Se_{62}$ was reduced in glasses containing lower content of germanium [61]. This hypothesis would explain the occurrence of high intensity peaks in the stretching vibrational region between ~250-330 cm^{-1}. Peak in this region at ~264 cm^{-1} decreases in the intensity with increasing antimony content. Another peak found in this region is at ~246 cm^{-1}. This peak may possibly be coming from Se–Se stretching modes at the outrigger.

Other peaks in Raman spectra of Ga-Sb-Se thin films are found at ~187 cm^{-1} and ~217 cm^{-1}. These two peaks are gradually merging with the peak at ~190 cm^{-1} in stoichiometric Sb_2Se_3 films corresponding to Sb–Se stretching vibration modes in $[SbSe_{3/2}]$ pyramidal units. Finally, low intensity Raman band peaking at ~123 cm^{-1} tends to disappear with increasing Sb content.

For more precise analysis of the local structure of Ga-Sb-Se thin films DFT calculations may be valuable to predict and identify individual modes proposed above.

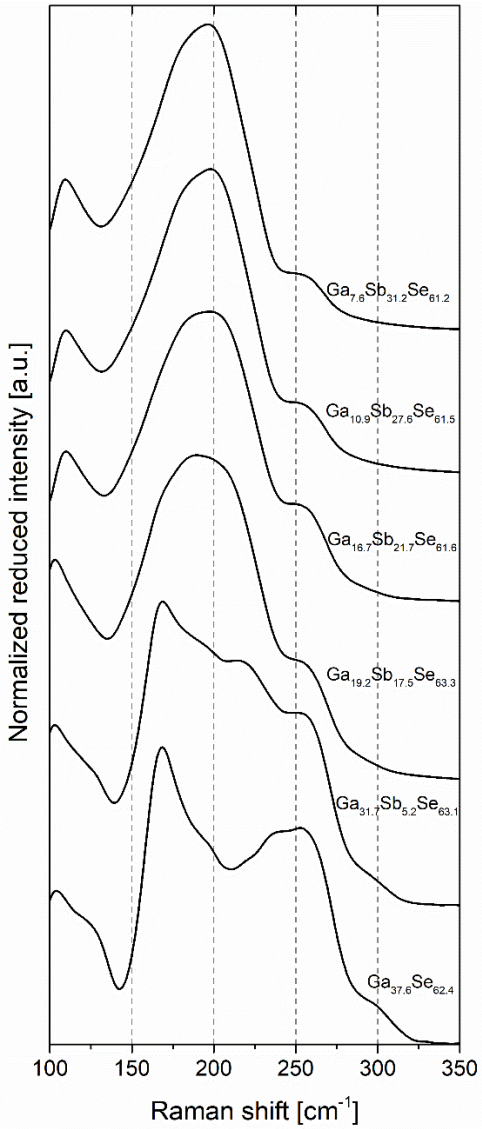

Fig. 4-5 Raman spectra of Ga-Sb-Se co-sputtered thin films with indicated compositions – samples shown in the plot correspond to the samples in table 2-4 – from bottom Nr. 1, 2, 4, 5, 7 and Nr. 8.

4.3. Local structure of Ge-Sb-Se-Te thin films

Raman spectra of Ge-Sb-Se-Te thin films are showed in the figure 4-6. In samples 2S1G-Se4-Te10 ($Ge_{19.4}Sb_{16.7}Se_{53.9}Te_{10}$) two bands dominate the spectra, specifically with maxima at ~166 and 198 cm^{-1}. In samples 2S1G-Se-Te15 ($Ge_{19.4}Sb_{16.7}Se_{48.9}Te_{15}$) the first peak is slightly shifted towards the lower wavenumbers peaking at ~160 cm^{-1} and the peak at 198 cm^{-1} is reduced in the intensity. It is assumed that the introduction of tellurium in the glass network leads to the formation of mixed entities such as [$GeSe_{4-x}Te_x$], [$SbSe_{3-x}Te_x$], Se–$Se_{(n-x)}$–Te_x or short Te–Te chains [30]. Peaks at ~166 and ~198 cm^{-1} can be possibly originating from symmetric stretching vibration modes in mixed tetrahedron [$GeSe_{2/2}Te_{2/2}$] [30]. Furthermore, the presence of tellurium affects the stretching vibrational region ~250 and 330 cm^{-1} [62]. It can be expected that some of the selenium atoms in Se–Se dimers, short selenium chains (Se_n) or at the outrigger in [$GeSe_{4/2}$] tetrahedra will be replaced by tellurium atoms resulting in shift of the peak at ~265 cm^{-1}, found in tellurium-free Ge-Sb-Se films, towards lower wavenumbers. The presence of tellurium also reduces the intensity of this peak [62]. All the mentioned features can be observed

when one compares the Raman spectra of tellurium-free 2S1G-Se4 thin film with 2S1G-Se4-Te10 and 2S1G-Se4-Te15 (fig. 4-7) deposited at the same conditions (*i.e.* electrical power of 10 W, Ar pressure of 5×10^{-3} mbar).

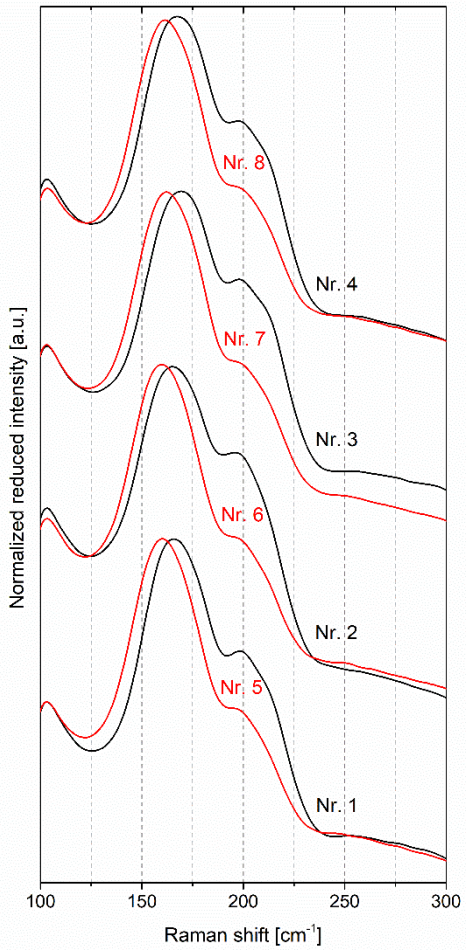

Fig. 4-6 Raman spectra of sputtered 2S1G-Se4-Te10 (black, Nr. 1 – 4 in table 2-6) and 2S1G-Se-Te15 (red lines, Nr. 5 – 8 in table 2-6) thin films.

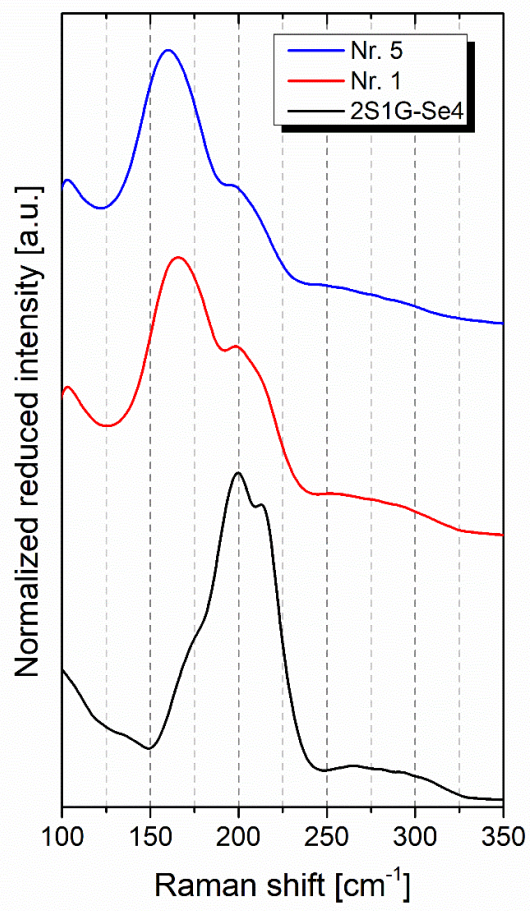

Fig. 4-7 Comparison of Raman spectra of tellurium-free 2S1G-Se4, 2S1G-Se4-Te10 and 2S1G-Se4-Te15.

Concluding remarks

The study of local structure of fabricated films was performed by means of Raman spectroscopy data analysis. In germanium-rich thin films fabricated by co-sputtering, tetrahedral structure (*i.e.* [$GeSe_{4/2}$]) is expected where the $GeSe_2$ or $GeSe_4$ target is employed. In the case of films fabricated using the high electrical power on $GeSe_2$ target, Raman spectrum is dominated by two bands peaking at ~198 and ~216 cm^{-1} ascribed to symmetric stretching vibrations of heteropolar Ge–Se bonds in corner-sharing (A_1) and edge-sharing (accompanion mode, A_1^C) [$GeSe_{4/2}$] structural unit. The intensity of Raman band at ~216 cm^{-1} is much lower for films co-sputtered from $GeSe_4$ target indicating that the structure is predominantly governed by heteropolar Ge–Se bonds in corner-sharing [$GeSe_{4/2}$] units in selenium-rich films. Presence of Se–Se dimers and short selenium chains (Se_n) in Se-rich films is also considered. In germanium-rich films, the presence of Ge–Ge homopolar bonds can be identified at ~175 cm^{-1}. The intensity of this peak becomes more significant when selenium-deficient $Ge_{28}Sb_{12}Se_{60}$ target is used.

The structure of co-sputtered amorphous Ga-Sb-Se thin films is still not well understood. It is assumed that gallium with its electronic configuration of s^2p^1 is 4-fold coordinated in chalcogenide glasses creating the dative bond *via* interaction with *p* lone pair of chalcogen atoms [63]. However, there is still lack of information for this system due to the certain facts such as limited glass-forming ability and high boiling point. For more precise analysis of the local structure of co-sputtered films DFT calculations may be valuable to predict and identify specific vibrational modes in this system. The addition of antimony in both Ge-Sb-Se and Ga-

Sb-Se systems induces the evolvement of Sb–Se stretching vibration modes in [$SbSe_{3/2}$] pyramidal units.

Finally, in Ge-Sb-Se-Te, the substitution of selenium by tellurium relative to Te-free Ge-Sb-Se films, seems to induce the various mixtures of entities, where the atoms of selenium are partly replaced by tellurium. Such replacement seems to shift corresponding peaks of these entities towards lower wavenumbers. This observation is consistent with the effect of chalcogen-chalcogen substitution on the structure of Ge-S-Se glasses [64].

5. Photosensitivity of sputtered and co-sputtered thin films

VASE was used for the determination of the optical bandgap energy and refractive index of thin films before (in as-deposited state) and after the irradiation. Photoinduced changes by means of optical bandgap change and the refractive index at 1.55 μm change are thus $\Delta E_g^{CL} = E_g^{CL}(irradiated) - E_g^{CL}(as-deposited)$ and $\Delta n = n(irradiated) - n(as-deposited)$ respectively.

Moreover, direct transmission measurements using portable spectrophotometer EPP 2000 (StellarNet Inc., Tampa, FL, USA) were carried out to quickly control the shift of the short-wavelength absorption edge during the irradiation. The typical set-up for the irradiation of the chalcogenide thin films is shown in the figure 5-1.

For the experiments, the used light source is continuous-wave monochromatic diode-pumped solid state laser or laser diode of desired wavelength. The distance between the laser source and the sample is approximately 75 cm. In this path, the beam may be attenuated or reshaped if needed so the beam of the intensity of 150 mW·cm^{-1} (±10 %) is achieved. The sample is placed in the photo-kinetic cell under pure argon atmosphere in order to minimize the surface oxidation of the samples. All the samples were irradiated for 180 minutes.

For the irradiation, the laser source with the wavelength near the optical bandgap was chosen. Specifically, the penetration depth (1/α) of the source must be larger, but close to the film's thickness. In this work, appropriate light sources operating at 532 nm (2.33 eV), 593.5 nm (2.09 eV), 635 nm (1.95 eV), 656 nm (1.89 eV), 730 nm (1.70 eV), 785 nm (1.58 eV) and 808 nm (1.53 eV) were at the disposal.

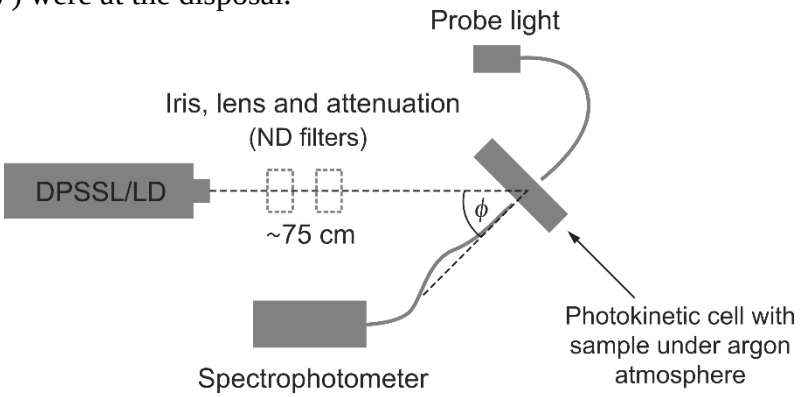

Fig. 5-1 Experimental set-up for irradiations.

5.1. Photosensitivity of Ge-Sb-Se thin films

The prolonged irradiation of Ge-Sb-Se co-sputtered films have shown two different trends by means of change in the optical properties. First, for the films co-sputtered from $GeSe_2$, Sb_2Se_3 and $Ge_{28}Sb_{12}Se_{60}$ (samples Nr. 1 to 16) which were rich in germanium, photobleaching (PB) was observed after 180 minutes of irradiation. The largest PB effect was found in the samples Nr. 10 ($GeSe_2$) and Nr. 11 ($Ge_{32.5}Sb_{1.2}Se_{66.3}$) where the changes ΔE_g^{CL} as high as 0.1 and 0.15 eV were observed, respectively.

As shown in table 5-1, PB tends to decrease with increasing antimony content up to Sb_2Se_3, which was found to be photostable under given conditions of irradiation [4]. For the sample Nr. 13 solely deposited from $Ge_{28}Sb_{12}Se_{60}$ target, only a small PB effect was observed with the optical energy gap change ΔE_g^{CL} of 0.03 eV when irradiated by 635 nm laser source. Furthermore, the changes in optical energy gap may be accompanied by the refractive index

change as shown in table 5-1. Unlike the changes in optical energy gap no clear trends can be justified in the refractive index changes Δn from VASE measurements though some high changes were observed. The largest decrease of refractive index of 0.04 was measured for sample Nr. 8. On the other hand, the increase by 0.04 and 0.03 was measured in sample Nr. 14 and samples Nr. 3, 5, 9, 12 and 16 respectively.

Moreover, *in situ* transmission measurements of these films have shown the crossover from transient photodarkening (PD) to meta-stable PB. This is illustrated in the figure 5-2, which corresponds to the data obtained for sample Nr. 10 and 11. Such behaviour is in accordance with previous results reported by Lin *et al.* and Sati and Jain for co-sputtered [65] and evaporated Ge-Sb-Se thin films respectively [66].

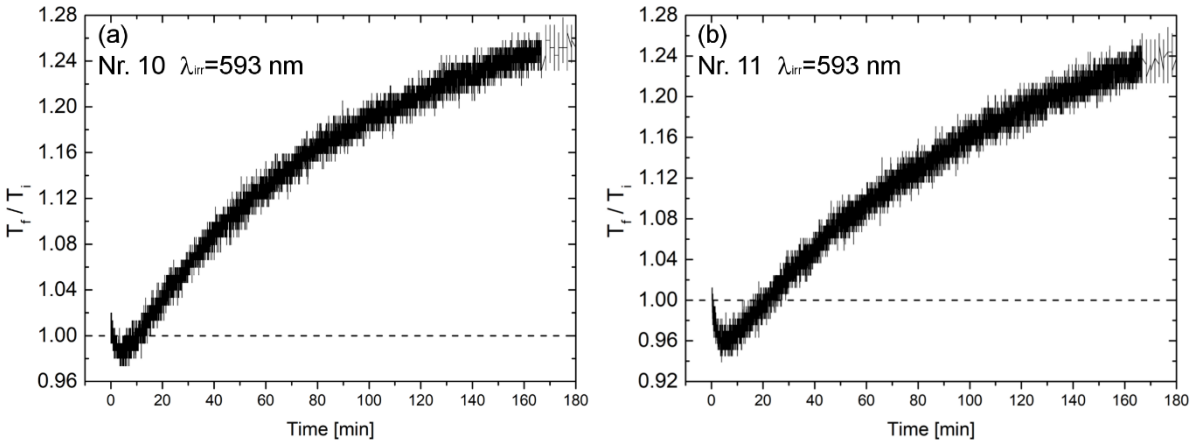

Fig. 5-2 Crossover from transient PD to meta-stable PB in the samples **(a)** Nr. 10 ($Ge_{32.5}Sb_{1.2}Se_{66.3}$) and **(b)** Nr. 11 ($Ge_{30.6}Sb_{6.7}Se_{62.7}$) when irradiated by 593 nm laser source; data collected at initial transmission T_i of 15 %.

Thin films of $GeSe_4$-Sb_2Se_3 pseudo-binary (samples Nr. 17 to 24, table 5-1) richer in selenium were found to undergo slight photodarkening (PD) when irradiated by near-bandgap light. According to direct transmission measurements, some PD persists also in the samples containing antimony. Collected data from transmission measurements shown in the figure 5-5, where transmission ratio T_f/T_i is given by the ratio between the transmission at a certain time divided by the initial transmission value, indicate that the magnitude of PD becomes smaller when the antimony content reached ~ 25 at. %. Furthermore, partial restoration of transmission was observed for all the samples when the laser was turned off. Thus, it seems that both transient and meta-stable processes are responsible for PD in these samples. Both photodarkening and photobleaching were previously reported in germanium-deficient Ge_xSe_{100-x} amorphous films. First, Kumar *et al.* have reported the crossover from PD to PB when the composition changes from germanium-deficient to germanium-rich Ge_xSe_{100-x} evaporated films. In their work, the PD in Ge_5Se_{95}, $Ge_{10}Se_{90}$ and $Ge_{20}Se_{80}$ is considered to be coming from photo-enhanced crystallization of amorphous selenium in Ge-Se matrix as concluded from Raman measurements [67]. It should be noted however that in their work, the intensity of laser beam (500 $mW \cdot cm^{-1}$) as well as the laser source energy (532 nm) was considerably higher than in the present work. Recently, Zhang *et al.* have found PB effect even in germanium-deficient sputtered $Ge_{16.8}Se_{83.2}$ when irradiated by 655 nm laser source at various intensities [68]. Furthermore, coexistence of transient PD and metastable PB was observed in evaporated amorphous Ge_2Se_3 and $GeSe_2$ films [69, 70].

It is reasonable to ask whether or not the interlayer model proposed by Shimakawa *et al.* [71] is relevant for Sb_2Se_3 films and what is the role of potential interlayer slip motion in Ge-Sb-Se films. In the case of Sb_2Se_3 film, transient PD of a small magnitude was also observed

(fig. 5-3). This PD is then followed by PB resulting in restoration of transmission almost to its initial value.

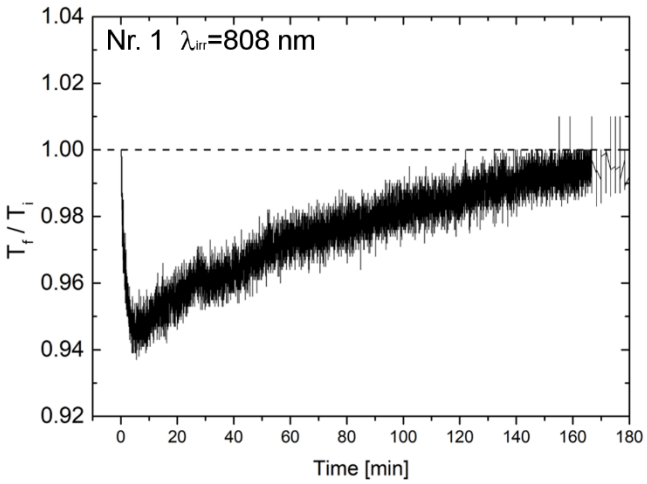

Fig. 5-3 Transient PD in Sb_2Se_3 (sample Nr. 1) thin film irradiated by 808 nm; data collected at initial transmission T_i of 10 %.

To answer the later, as seen from the Raman spectra of films deposited from $GeSe_4$ target, the peak intensity of corner-sharing (A_1) vibrational modes in [$GeSe_{4/2}$] tetrahedra is much higher than that of edge-sharing (A_1^C) ones. In contrast, this ratio is different in films deposited using $GeSe_2$ target. Four-fold coordinated germanium in A_1^C may spatially constrain the glass network so the magnitude of PD is rather low for films co-sputtered from $GeSe_2$ and $Ge_{28}Sb_{12}Se_{60}$. Furthermore, the high selenium content in films deposited from $GeSe_4$ target probably causes the opposite.

Another explanation of coexistence of transient PD and slow PB in Ge-Sb-Se films was recently proposed by Sati and Jain [66]. They assume that during the irradiation of evaporated $Ge_{40-x}Sb_xSe_{60}$ thin films the structural units containing homopolar Ge–Ge, Sb–Sb or Se–Se bonds and heteropolar bonds of Ge–Se, Sb–Se respond independently, creating the competition among Sb–Se, Se–Se and Ge–Se structural units. Sb–Se leads to the initial change by means of PD while Ge–Se bonds formation dominates the PB process. Thus the coexistence of fast PD and PB is given by the diverse nature of structural units [66].

Both interlayer model and bond rearrangement may provide the explanation, why the PB effect is not observed in samples Nr. 17 – 24. Germanium in films co-sputtered from $GeSe_4$ is expected to be almost entirely connected to selenium due to the excess of selenium. In the case of films co-sputtered from $GeSe_2$ and $Ge_{28}Sb_{12}Se_{60}$, homopolar Ge–Ge bonds existing in these films cause large PB in germanium-rich films. Nevertheless, even if the experiments were performed under pure argon atmosphere, we cannot completely exclude that another contribution to PB effect might be originating from some photo-oxidation of the surface.

Raman scattering spectra analysis of co-sputtered films before and after irradiation represented by figure 5-4 did not confirm that the shift in the optical bandgap energy is strictly due to the homo-to-heteropolar bond conversion.

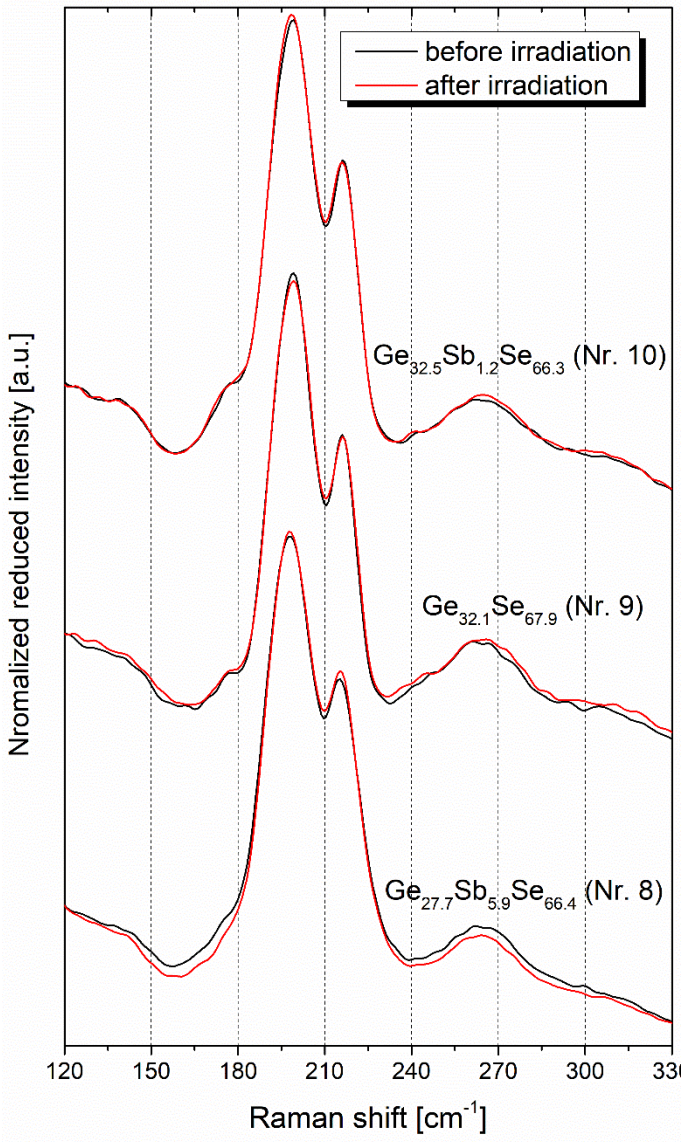

Fig. 5-4 Comparison of normalized reduced Raman spectra of samples Nr. 8 to Nr 10 before and after irradiation.

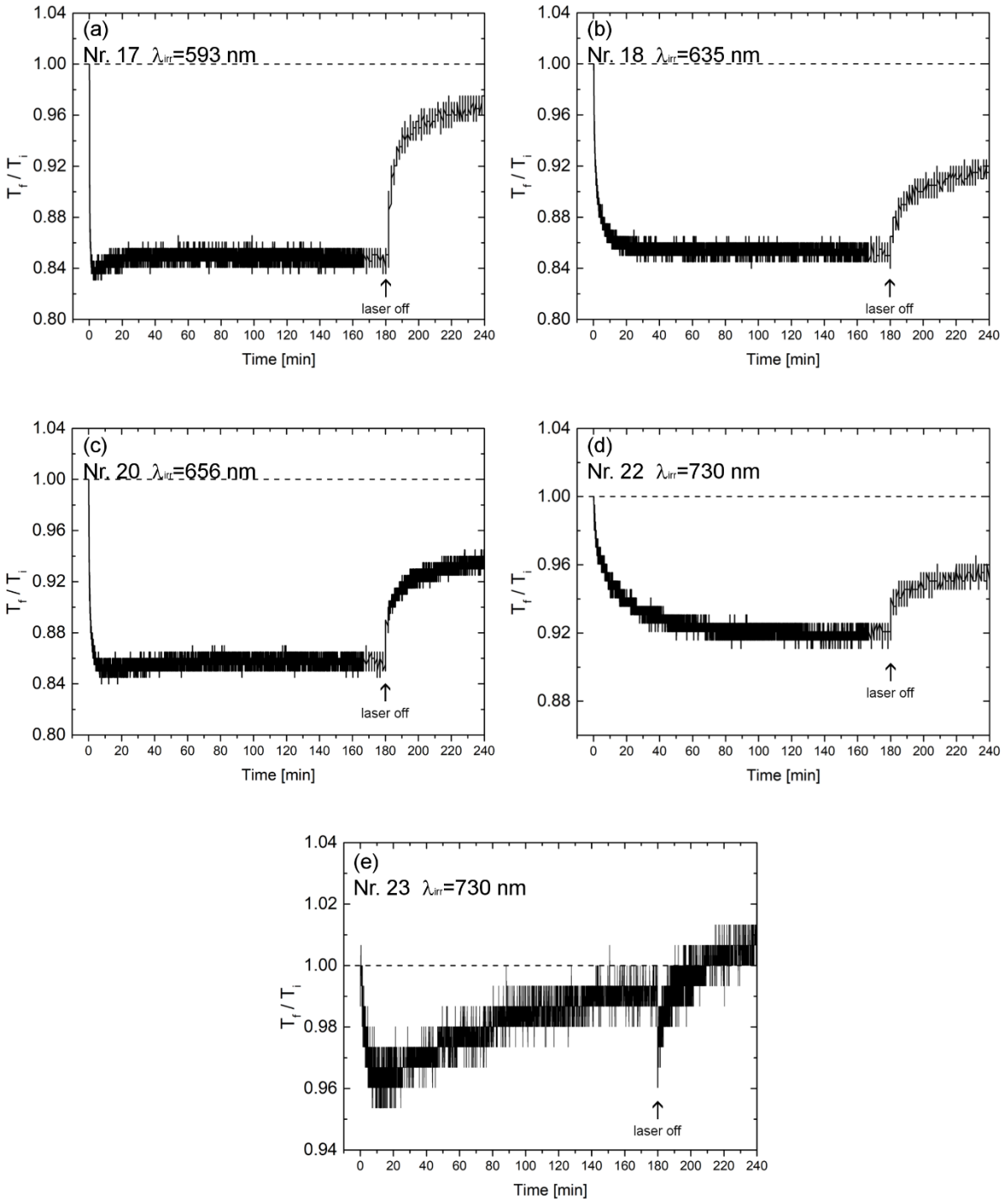

Fig. 5-5 Evolution of transmission ratio during the irradiation of samples **(a)** Nr. 17 ($Ge_{19.6}Se_{80.4}$) – irradiated by 597 nm, **(b)** Nr. 18 ($Ge_{14.0}Sb_{5.7}Se_{80.3}$) – irradiated by 635 nm, **(c)** Nr. 20 ($Ge_{10.9}Sb_{13.9}Se_{75.2}$) – irradiated by 656 nm **(d)** Nr. 22 ($Ge_{7.4}Sb_{24.5}Se_{68.1}$) – irradiated by 730 nm and **(e)** Nr. 23 ($Ge_{5.7}Sb_{28.8}Se_{65.5}$) – irradiated by 730 nm; data collected at initial transmission T_i of 20 %

Table 5-1 Photoinduced changes in optical bandgap ($\Delta E_g^{CL} = E_g^{CL}$(irradiated) $- E_g^{CL}$(as-deposited) and refractive index at 1.55 μm ($\Delta n = n$(irradiated)$-n$(as-deposited) of Ge-Sb-Se thin films with indicated chemical compositions (± 1 at. %) evaluated by EDS and wavelength of irradiation (λ_{irr} in nanometres).

Nr	Composition (at. %)	λ_{irr}	ΔE_g^{CL}(eV)	Δn @1.55 μm
1	$Sb_{39.4}Se_{60.6}$	808	0.01	0.02
2	$Sb_{39.9}Se_{60.1}$	808	-0.01	0.02
3	$Ge_{5.0}Sb_{33.4}Se_{61.6}$	808	0.02	0.03
4	$Ge_{9.5}Sb_{28.7}Se_{61.8}$	730	-0.02	0.00
5	$Ge_{12.3}Sb_{24.8}Se_{62.9}$	690	-0.01	0.03
6	$Ge_{16.4}Sb_{19.4}Se_{64.2}$	635	0.02	0.00
7	$Ge_{23.4}Sb_{11.5}Se_{65.1}$	593	0.07	0.01
8	$Ge_{27.7}Sb_{5.9}Se_{66.4}$	593	0.06	-0.04
9	$Ge_{32.1}Se_{67.9}$	532	0.11	0.03
10	$Ge_{32.5}Sb_{1.2}Se_{66.3}$	593	0.15	0.00
11	$Ge_{30.6}Sb_{6.7}Se_{62.7}$	593	0.04	-0.01
12	$Ge_{27.3}Sb_{12.3}Se_{60.4}$	690	0.03	0.03
13	$Ge_{27.7}Sb_{12.3}Se_{60.0}$	635	0.03	0.00
14	$Ge_{23.3}Sb_{16.0}Se_{60.7}$	690	-0.01	0.04
15	$Ge_{11.2}Sb_{28.4}Se_{60.4}$	730	0.00	0.00
16	$Ge_{3.0}Sb_{36.3}Se_{60.7}$	808	0.01	0.03
17	$Ge_{19.6}Se_{80.4}$	593	-0.02	0.01
18	$Ge_{14.0}Sb_{5.7}Se_{80.3}$	635	-0.05	-0.01
19	$Ge_{12.7}Sb_{10.5}Se_{76.8}$	635	-0.04	0.00
20	$Ge_{10.9}Sb_{13.9}Se_{75.2}$	656	-0.01	-0.01
21	$Ge_{9.0}Sb_{20.2}Se_{70.8}$	-	-	-
22	$Ge_{7.4}Sb_{24.5}Se_{68.1}$	730	-0.04	0.02
23	$Ge_{5.7}Sb_{28.8}Se_{65.5}$	730	0.00	0.00
24	$Ge_{2.9}Sb_{35.1}Se_{62.0}$	-	-	-

It should be noted that for the systems rich in antimony, the reflectivity (and the refractive index) is very high making the identification of the actual spot of irradiation very difficult.

5.2. Photosensitivity of Ga-Sb-Se thin films

To author's knowledge no photosensitivity studies have been conducted for the Ga-Sb-Se system. As illustrated in the figure 5-6 the prolonged irradiation of Ga-Sb-Se co-sputtered films leads to PB effect. Largest PB effect was found in the samples Nr. 1 (Ga_2Se_3) where the change ΔE_g^{CL} is 0.1 eV. The magnitude of PB decreases monotonically with an increasing antimony content. Similar to Ge-rich Ge-Sb-Se thin films, transient PD was observed when the laser was switched on. Photoinduced changes in all the Ga-Sb-Se thin films are summarized in table 5-2. No significant changes in refractive index which may accompany the changes of optical bandgap were observed except for sample Nr. 4 with composition $Ga_{19.2}Sb_{17.5}Se_{63.3}$ with Δn of 0.03.

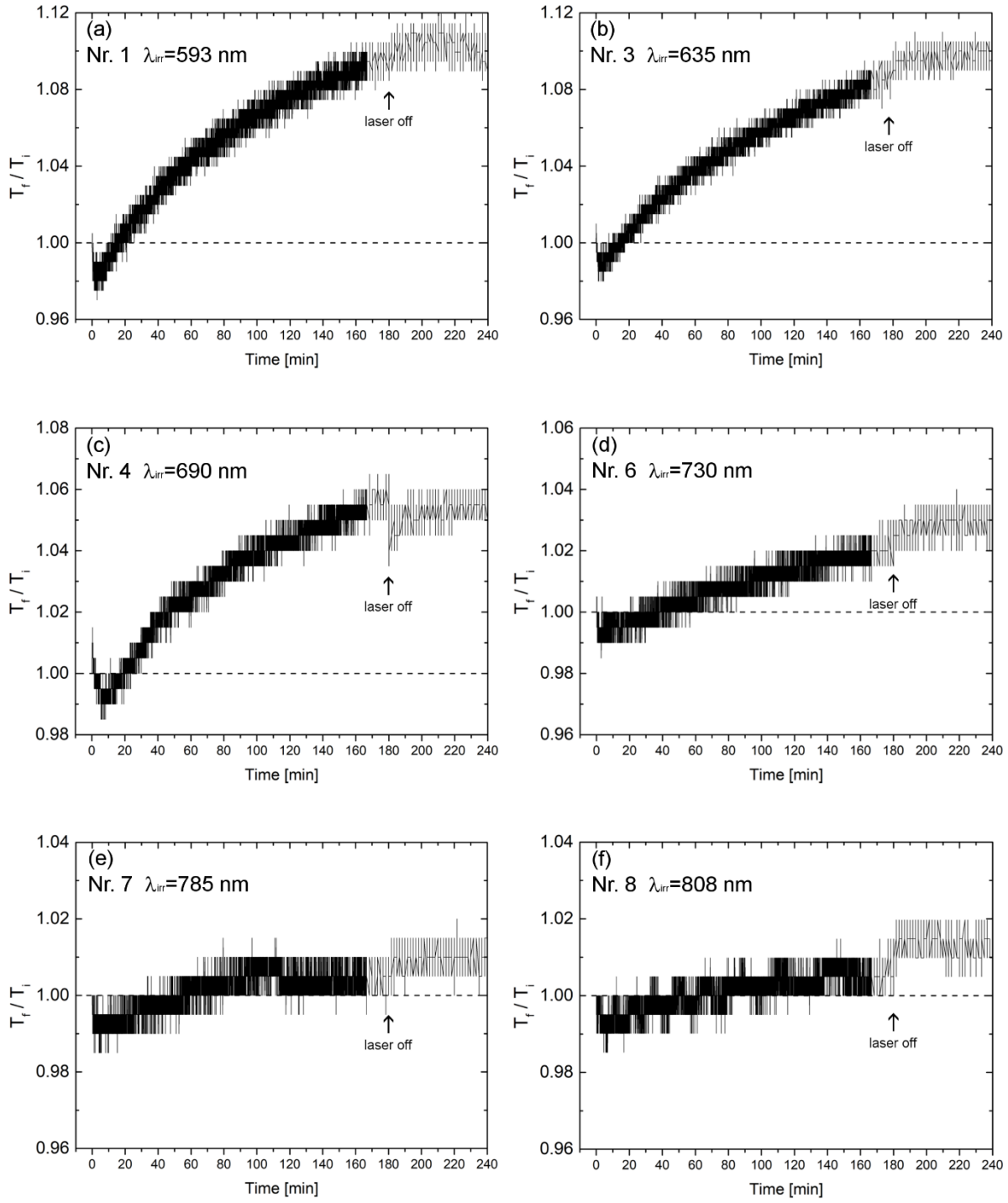

Fig. 5-6 Evolution of transmission ratio during the irradiation of samples (a) Nr. 1 ($Ga_{37.6}Se_{62.4}$) – irradiated by 597 nm, (b) Nr. 3 ($Ga_{30.3}Sb_{6.9}Se_{62.8}$) – irradiated by 635 nm, (c) Nr. 4 ($Ga_{19.2}Sb_{17.5}Se_{63.3}$) – irradiated by 690 nm (d) Nr. 6 ($Ga_{13.6}Sb_{24.7}Se_{61.7}$) – irradiated by 730 nm and (e) Nr. 7 ($Ga_{10.9}Sb_{27.6}Se_{61.5}$) – irradiated by 785, (f) Nr. 8 ($Ga_{7.6}Sb_{31.2}Se_{61.2}$) – irradiated by 808 nm; data collected at initial transmission T_i of 20 %

Table 5-2 Photoinduced changes in optical bandgap ($\Delta E_g^{CL} = E_g^{CL}$(irradiated) $- E_g^{CL}$(as-deposited) and refractive index at 1.55 μm ($\Delta n = n$(irradiated)$-n$(as-deposited) of Ga-Sb-Se thin films with indicated chemical compositions (± 1 at. %) evaluated by EDS and wavelength of irradiation (λ_{irr} in nanometres).

Nr	Composition (at. %)	λ_{irr}	ΔE_g^{CL}(eV)	Δn @1.55 μm
1	$Ga_{37.6}Se_{62.4}$	693	0.10	-0.01
2	$Ga_{31.7}Sb_{5.2}Se_{63.1}$	635	0.06	-0.01
3	$Ga_{30.3}Sb_{6.9}Se_{62.8}$	656	0.06	0.00
4	$Ga_{19.2}Sb_{17.5}Se_{63.3}$	690	-0.01	0.03
5	$Ga_{16.7}Sb_{21.7}Se_{61.6}$	730	0.02	0.01
6	$Ga_{13.6}Sb_{24.7}Se_{61.7}$	730	0.00	0.00
7	$Ga_{10.9}Sb_{27.6}Se_{61.5}$	785	-0.01	0.02
8	$Ga_{7.6}Sb_{31.2}Se_{61.2}$	808	0.00	0.01

Possible explanation of observed photoinduced changes in Ga-Sb-Se thin films may be similar to that one in Ge-Sb-Se system considering the same shape of transmission evolution during the experiments. Nonetheless, as for Ge-Sb-Se films, despite the fact that the experiments were performed under pure argon atmosphere, the influence of humidity (and oxygen) should not be completely ruled out [72]. Photo-enhanced oxidation in crystalline Ga_2Se_3 under prolonged Ar^+ laser irradiation (λ = 514.5 nm) leads to the replacement of selenium by oxygen as reported by Nobuaki *et al.* [73]. This leads to the increase in optical transparency of thin film due to the refractive index difference between Ga_2Se_3 and Ga_2O_3.

Conclusion remarks

Photosensitivity studies were performed by means of prolonged irradiation by near-bandgap light with respect to the penetration depth of used light source. In order to minimize the effect of surface photo-oxidation, samples were placed in photo-kinetic cell with the pure argon atmosphere. In co-sputtered Ge-Sb-Se films, two opposite shifts of the fundamental short-wavelength absorption edge were observed. Specifically, photobleaching effect in germanium-rich films deposited from $GeSe_2$ and PD in selenium-rich films deposited from $GeSe_4$. The increase of bandgap due to the PB expressed as ΔE_g^{CL} may be as high as 0.15 eV ($Ge_{32.5}Sb_{1.2}Se_{66.3}$). The largest magnitude of PD was present in $Ge_{14.0}Sb_{5.7}Se_{80.3}$ ($\Delta E_g^{CL} = -0.4$ eV). The reason for such observation may lie in the different structure of films co-sputtered from these targets. Photodarkening in amorphous selenium is well known phenomena [74]. Kumar *et al.* proposed that the PD in Ge-deficient Ge_xSe_{100-x} evaporated films is due to the photocrystallization of amorphous selenium when irradiated by 532 nm laser source (intensity of 500 $mW \cdot cm^{-1}$) on air [67]. Moreover, Ge-deficient films with the high selenium content are probably more prone to PD due to their underconstrained glass network structure. With increasing germanium content, the glass network becomes more constrained, so the magnitude of PD is supressed. Besides that, at high content of germanium in Ge-Sb-Se films, the presence of Ge–Ge homopolar bonds is probably unavoidable. Although it was not confirmed in this work, homo-to-heteropolar bond conversion usually takes part during the irradiation resulting in PB effect.

To the author's knowledge, the photosensitivity of amorphous co-sputtered Ga-Sb-Se films was performed for the first time. The effect of prolonged irradiation on the optical properties seems to be of same manner as in Ge-Sb-Se system deposited from $GeSe_2$, $Ge_{28}Sb_{12}Se_{60}$ and Sb_2Se_3 targets. The largest PB expressed as ΔE_g^{CL} was found in binary Ga_2Se_3, with the value of 0.10 eV. Increasing antimony content in both Ge-Sb-Se and Ga-Sb-Se tend to decrease the magnitude of PB these films.

Unlike the changes in optical bandgap energy no clear trends can be justified in the photoinduced refractive index changes Δn (extracted from VASE data) in both Ge-Sb-Se and Ga-Sb-Se systems. The largest decrease for Ge-Sb-Se co-sputtered films was found in sample Nr. 8 ($Ge_{27.7}Sb_{5.9}Se_{66.4}$) - the refractive index of this sample decreased by 0.04 on irradiation. On the other hand, the photoinduced increase of highest magnitude was observed for sample Nr. 14 ($Ge_{23.3}Sb_{16.0}Se_{60.}7$) and Nr. 4 ($Ga_{19.2}Sb_{17.5}Se_{63.3}$) from Ge-Sb-Se and Ga-Sb-Se system respectively. The increase of 0.03 was also found for samples Nr. 3, 5, 9, 12 and 16 from Ge-Sb-Se system.

References

1. Halenkovič T., Němec P., Gutwirth J., Baudet E., Specht M., Gueguen Y., Sangleboeuf J.-C., Nazabal V. Co-sputtered amorphous Ge-Sb-Se thin films: optical properties and structure. *SPIE Optics + Optoelectronics*: 2017.
2. Chen Y., Shen X., Wang R., Wang G., Dai S., Xu T., Nie Q. Optical and structural properties of Ge–Sb–Se thin films fabricated by sputtering and thermal evaporation. *Journal of Alloys and Compounds.* 2013;*548:*155-160.
3. Šútorová K., Prokeš L., Nazabal V., Baudet E., Havel J., Němec P. Laser Desorption Ionization Time-of-Flight Mass Spectrometry of Glasses and Amorphous Films from Ge–As–Se System. *Journal of the American Ceramic Society.* 2016;*99:*3594-3599.
4. Halenkovič T., Gutwirth J., Němec P., Baudet E., Specht M., Gueguen Y., Sangleboeuf J.-C., Nazabal V. Amorphous Ge-Sb-Se thin films fabricated by co-sputtering: Properties and photosensitivity. *Journal of the American Ceramic Society.* 2018;*101:*2877-2887.
5. Eggleton B.J., Luther-Davies B., Richardson K. Chalcogenide photonics. *Nat Photon.* 2011;*5:*141-148.
6. Němec P., Olivier M., Baudet E., Kalendová A., Benda P., Nazabal V. Optical properties of (GeSe2)100−x(Sb2Se3)x glasses in near- and middle-infrared spectral regions. *Materials Research Bulletin.* 2014;*51:*176-179.
7. Chen L.Y., Chen F.F., Dai S.X., Tao G.M., Yan L.H., Shen X., Ma H.L., Zhang X.H., Xu Y.S. Third-order nonlinearity in Ge-Sb-Se glasses at mid-infrared wavelengths. *Materials Research Bulletin.* 2015;*70:*204-208.
8. Olivier M., Tchahame J.C., Němec P., Chauvet M., Besse V., Cassagne C., Boudebs G., Renversez G., Boidin R., Baudet E., Nazabal V. Structure, nonlinear properties, and photosensitivity of (GeSe2)100-x(Sb2Se3)x glasses. *Optical Materials Express.* 2014;*4:*525-540.
9. Wei W.-H., Wang R.-P., Shen X., Fang L., Luther-Davies B. Correlation between Structural and Physical Properties in Ge–Sb–Se Glasses. *The Journal of Physical Chemistry C.* 2013;*117:*16571-16576.
10. Haisty R.W., Krebs H. Elektrische Leitfähigkeit und Chalkogenidglas-Bildung in Schmelzen von Ge-As-Se und Ge-Sb-Se. *Angewandte Chemie.* 1968;*80:*999-1000.
11. Lecomte A., Nazabal V., Le Coq D., Calvez L. Ge-free chalcogenide glasses based on Ga-Sb-Se and their stabilization by iodine incorporation. *Journal of Non-Crystalline Solids.* 2018;*481:*543-547.
12. Popescu M., Non-crystalline chalcogenides, Dordrecht ; Boston Kluwer Academic Publishers, 2000,
13. Lu Y., Song S., Shen X., Wang G., Wu L., Song Z., Liu B., Dai S. Phase change characteristics of Sb-rich Ga–Sb–Se materials. *Journal of Alloys and Compounds.* 2014;*586:*669-673.
14. Sharma N., Sharda S., Katyal S.C., Sharma V., Sharma P. Effect of Te on linear and non-linear optical properties of new quaternary Ge-Se-Sb-Te chalcogenide glasses. *Electronic Materials Letters.* 2014;*10:*101-106.
15. Tauc J., Amorphous and liquid semiconductors, London, New York, Plenum, 1974,
16. Chen C., Li W., Zhou Y., Chen C., Luo M., Liu X., Zeng K., Yang B., Zhang C., Han J., Tang J. Optical properties of amorphous and polycrystalline Sb2Se3 thin films prepared by thermal evaporation. *Applied Physics Letters.* 2015;*107:*043905.
17. Tichý L., Sleeckx E., Nagels P., Tichá H. The influence of temperature on the optical absorption edge shift induced by band-gap illumination in thin amorphous GeSe2 films. *Philosophical Magazine Part B.* 1996;*73:*213-221.

18. Chen F., Zhang Z., Wang Y., Nie Q., Shen X., Dai S. Optical properties of amorphous In-doped GeSe2 films for all-optical applications. *Infrared Physics & Technology.* 2015;*69:*32-35.
19. Pan R.K., Tao H.Z., Zang H.C., Zhao X.J., Zhang T.J. Annealing effects on the structure and optical properties of GeSe2 and GeSe4 films prepared by PLD. *Journal of Alloys and Compounds.* 2009;*484:*645-648.
20. Balan V., Vigreux C., Pradel A. Chalcogenide thin films deposited by radio-frequency sputtering. *Journal of Optoelectronics and Advanced materials.* 2004;*6:*875-882.
21. Oheda H. The Exponential Absorption Edge in Amorphous Ge–Se Compounds. *Japanese Journal of Applied Physics.* 1979;*18:*1973.
22. Hachiya K. Density functional electronic structures calculations of GeSe2. *Journal of Non-Crystalline Solids.* 2001;*291:*160-166.
23. Carey J.J., Allen J.P., Scanlon D.O., Watson G.W. The electronic structure of the antimony chalcogenide series: Prospects for optoelectronic applications. *Journal of Solid State Chemistry.* 2014;*213:*116-125.
24. Sati D.C., Kovalskiy A., Golovchak R., Jain H. Structure of SbxGe40-xSe60 glasses around 2.67 average coordination number. *Journal of Non-Crystalline Solids.* 2012;*358:*163-167.
25. Kovalskiy A., Jain H., Miller A.C., Golovchak R.Y., Shpotyuk O.I. A Study of Reversible γ-Induced Structural Transformations in Vitreous Ge23.5Sb11.8S64.7 by High-Resolution X-ray Photoelectron Spectroscopy. *The Journal of Physical Chemistry B.* 2006;*110:*22930-22934.
26. Afifi M.A., Bekheet A.E., El-Shair H.T., Zedan I.T. Determination and analysis of optical constants for Ga2Se3 films near absorption edge. *Physica B: Condensed Matter.* 2003;*325:*308-318.
27. Kuriakose T., Baudet E., Halenkovič T., Elsawy M.M.R., Němec P., Nazabal V., Renversez G., Chauvet M. Measurement of ultrafast optical Kerr effect of Ge–Sb–Se chalcogenide slab waveguides by the beam self-trapping technique. *Optics Communications.* 2017;*403:*352-357.
28. Baudet E., Gutierrez-Arroyo A., Baillieul M., Charrier J., Němec P., Bodiou L., Lemaitre J., Rinnert E., Michel K., Bureau B., Adam J.L., Nazabal V. Development of an evanescent optical integrated sensor in the mid-infrared for detection of pollution in groundwater or seawater. *Advanced Device Materials.* 2017;*3:*23-29.
29. Baillieul M., Halenkovič T., Gutierrez-Arrovo A.J., Baudet E., Rinnert E., Gutwirth J., Němec P., Charrier J., Bodiou L., Colas F., Boukerma K., Boussard C., Bureau B., Michel K., Nazabal V. Infrared-Sensor Based on Selenide Waveguide Devoted to Water Pollution. *20th International Conference on Transparent Optical Networks, ICTON 2018.* Bucharest, Romania: 2018.
30. Abdellaoui N., Starecki F., Boussard-Pledel C., Shpotyuk Y., Doualan J.L., Braud A., Baudet E., Nemec P., Cheviré F., Dussauze M., Bureau B., Camy P., Nazabal V. Tb3+ doped Ga5Ge20Sb10Se65-xTex (x = 0-37.5) chalcogenide glasses and fibers for MWIR and LWIR emissions. *Optical Materials Express.* 2018;*8:*2887-2900.
31. Baudet E., Sergent M., Němec P., Cardinaud C., Rinnert E., Michel K., Jouany L., Bureau B., Nazabal V. Experimental design approach for deposition optimization of RF sputtered chalcogenide thin films devoted to environmental optical sensors. *Scientific Reports.* 2017;*7:*3500.
32. Sheik-Bahae M., Hagan D.J., Van Stryland E.W. Dispersion and band-gap scaling of the electronic Kerr effect in solids associated with two-photon absorption. *Physical Review Letters.* 1990;*65:*96-99.

33. Dai S., Chen F., Xu Y., Xu Z., Shen X., Xu T., Wang R., Ji W. Mid-infrared optical nonlinearities of chalcogenide glasses in Ge-Sb-Se ternary system. *Optics Express.* 2015;*23:*1300-1307.
34. Quémard C., Smektala F., Couderc V., Barthélémy A., Lucas J. Chalcogenide glasses with high non linear optical properties for telecommunications. *Journal of Physics and Chemistry of Solids.* 2001;*62:*1435-1440.
35. Lenz G., Zimmermann J., Katsufuji T., Lines M.E., Hwang H.Y., Spälter S., Slusher R.E., Cheong S.W., Sanghera J.S., Aggarwal I.D. Large Kerr effect in bulk Se-based chalcogenide glasses. *Optics Letters.* 2000;*25:*254-256.
36. Smektala F., Quemard C., Couderc V., Barthélémy A. Non-linear optical properties of chalcogenide glasses measured by Z-scan. *Journal of Non-Crystalline Solids.* 2000;*274:*232-237.
37. Wang T., Gai X., Wei W., Wang R., Yang Z., Shen X., Madden S., Luther-Davies B. Systematic z-scan measurements of the third order nonlinearity of chalcogenide glasses. *Optical Materials Express.* 2014;*4:*1011-1022.
38. Tichá H., Tichý L. Semiempirical relation between Non-linear susceptibility (refractive index), Linear refractive index and Optical gap and its Application to Amorphous chalcogenides. *Journal of Optoelectronics and Advanced materials.* 2002;*4:*381-386.
39. Tanaka K. Nonlinear optics in glasses: How can we analyze? *Journal of Physics and Chemistry of Solids.* 2007;*68:*896-900.
40. Boyd R.W., Nonlinear optics, Amsterdam ; Boston Academic Press, 2008,
41. Shuker R., Gammon R.W. Raman-Scattering Selection-Rule Breaking and the Density of States in Amorphous Materials. *Physical Review Letters.* 1970;*25:*222-225.
42. Olivier M., Němec P., Boudebs G., Boidin R., Focsa C., Nazabal V. Photosensitivity of pulsed laser deposited Ge-Sb-Se thin films. *Optical Materials Express.* 2015;*5:*781-793.
43. Sugai S. Stochastic random network model in Ge and Si chalcogenide glasses. *Physical Review B.* 1987;*35:*1345-1361.
44. Wang Y., Matsuda O., Inoue K., Yamamuro O., Matsuo T., Murase K. A Raman scattering investigation of the structure of glassy and liquid GexSe1−x. *Journal of Non-Crystalline Solids.* 1998;*232–234:*702-707.
45. Nazabal V., Charpentier F., Adam J.-L., Nemec P., Lhermite H., Brandily-Anne M.-L., Charrier J., Guin J.-P., Moréac A. Sputtering and Pulsed Laser Deposition for Near- and Mid-Infrared Applications: A Comparative Study of Ge25Sb10S65 and Ge25Sb10Se65 Amorphous Thin Films. *International Journal of Applied Ceramic Technology.* 2011;*8:*990-1000.
46. Kostadinova O., Yannopoulos S.N. Raman spectroscopic study of SbxSe100−x phase-separated bulk glasses. *Journal of Non-Crystalline Solids.* 2009;*355:*2040-2044.
47. Němec P., Frumarová B., Frumar M. Structure and properties of the pure and Pr3+-doped Ge25Ga5Se70 and Ge30Ga5Se65 glasses. *Journal of Non-Crystalline Solids.* 2000;*270:*137-146.
48. Nazabal V., Němec P., Jurdyc A.M., Zhang S., Charpentier F., Lhermite H., Charrier J., Guin J.P., Moreac A., Frumar M., Adam J.L. Optical waveguide based on amorphous Er3+-doped Ga–Ge–Sb–S(Se) pulsed laser deposited thin films. *Thin Solid Films.* 2010;*518:*4941-4947.
49. Baudet E., Cardinaud C., Girard A., Rinnert E., Michel K., Bureau B., Nazabal V. Structural analysis of RF sputtered Ge-Sb-Se thin films by Raman and X-ray photoelectron spectroscopies. *Journal of Non-Crystalline Solids.* 2016;*444:*64-72.
50. Micoulaut M., Kachmar A., Bauchy M., Roux S., Massobrio C., Boero M., Structure, topology, rings, and vibrational and electronic properties of GexSe1-x glasses across the rigidity transition: A numerical study, 2013,

51. Lucovsky G., Mooradian A., Taylor W., Wright G.B., Keezer R.C. Identification of the fundamental vibrational modes of trigonal, α - monoclinic and amorphous selenium. *Solid State Communications.* 1967;*5:*113-117.
52. Ivanova Z.G., Cernoskova E., Vassilev V.S., Boycheva S.V. Thermomechanical and structural characterization of GeSe2–Sb2Se3–ZnSe glasses. *Materials Letters.* 2003;*57:*1025-1028.
53. Petit L., Carlie N., Richardson K., Guo Y., Schulte A., Campbell B., Ferreira B., Martin S. Effect of the substitution of S for Se on the structure of the glasses in the system Ge0.23Sb0.07S0.70−xSex. *Journal of Physics and Chemistry of Solids.* 2005;*66:*1788-1794.
54. Jackson K., Briley A., Grossman S., Porezag D.V., Pederson M.R. Raman-active modes of a-GeSe2 and a-GeS2: A first-principles study. *Physical Review B.* 1999;*60:*R14985-R14989.
55. Matsuda O., Inoue K., Murase K. Resonant Raman study on crystalline GeSe2 in relation to amorphous states. *Solid State Communications.* 1990;*75:*303-308.
56. Griffiths J.E., Espinosa G.P., Phillips J.C., Remeika J.P. Raman spectra and athermal laser annealing of Ge (SxSe1-x)2 glasses. *Physical Review B.* 1983;*28:*4444-4453.
57. Fukunaga T., Tanaka Y., Murase K. Glass formation and vibrational properties in the (Ge, Sn) system. *Solid State Communications.* 1982;*42:*513-516.
58. Mao A.W., Aitken B.G., Youngman R.E., Kaseman D.C., Sen S. Structure of Glasses in the Pseudobinary System Ga2Se3–GeSe2: Violation of Chemical Order and 8-N Coordination Rule. *The Journal of Physical Chemistry B.* 2013;*117:*16594-16601.
59. Akira Y., Nobuaki K., Kiyoshi T., Tamotsu O., Makoto K. Raman Study of Epitaxial Ga 2 Se 3 Films Grown by Molecular Beam Epitaxy. *Japanese Journal of Applied Physics.* 1992;*31:*L186.
60. Řičica T., Dostál L., Růžičková Z., Beneš L., Němec P., Bouška M., Macak J.M., Knotek P., Ruleová P., Jambor R. Synthesis, Structure and Application of Intramolecularly-Coordinated Gallium Chalcogenides: Suitable Single-Source precursors for GaxSey Materials. *Chemistry – A European Journal.* 2018;*24:*14470-14476.
61. Verger F., Nazabal V., Colas F., Němec P., Cardinaud C., Baudet E., Chahal R., Rinnert E., Boukerma K., Peron I., Deputier S., Guilloux-Viry M., Guin J.P., Lhermite H., Moreac A., Compère C., Bureau B. RF sputtered amorphous chalcogenide thin films for surface enhanced infrared absorption spectroscopy. *Optical Materials Express.* 2013;*3:*2112-2131.
62. Mendoza-Galván A., García-García E., Vorobiev Y.V., González-Hernández J. Structural, optical and electrical characterization of amorphous SexTe1−x thin film alloys. *Microelectronic Engineering.* 2000;*51-52:*677-687.
63. Tichý L., Tichá H. On the chemical threshold in chalcogenide glasses. *Materials Letters.* 1994;*21:*313-319.
64. Xuecai H., Guangying S., Yu L., Hongbo Y., Yonghua L. Structure and vibrational modes of Ge-S-Se glasses: Raman scattering and ab initio calculations. *Chalcogenide Letters.* 2012;*9:*465-474.
65. Lin L., Wang G., Shen X., Dai S., Xu T., Nie Q. Photo-induced structural changes in Ge-Sb-Se films. *Infrared Physics & Technology.* 2017;*81:*59-63.
66. Sati D.C., Jain H. Coexistence of photodarkening and photobleaching in Ge-Sb-Se thin films. *Journal of Non-Crystalline Solids.* 2017;*478:*23-28.
67. Kumar R.R., Barik A.R., Vinod E.M., Bapna M., Sangunni K.S., Adarsh K.V. Crossover from photodarkening to photobleaching in a-GexSe100-x thin films. *Optics Letters.* 2013;*38:*1682-1684.
68. Zhang S., Chen Y., Wang R., Shen X., Dai S. Observation of photobleaching in Ge-deficient Ge(16.8)Se(83.2) chalcogenide thin film with prolonged irradiation. *Scientific Reports.* 2017;*7:*14585-14585.

69. Barik A.R., Naik R., Adarsh K.V. Unusual observation of fast photodarkening and slow photobleaching in a-GeSe2 thin film. *Journal of Non-Crystalline Solids.* 2013;*377:*179-181.
70. Yan Q., Jain H., Ren J., Zhao D., Chen G. Effect of Photo-Oxidation on Photobleaching of GeSe2 and Ge2Se3 Films. *The Journal of Physical Chemistry C.* 2011;*115:*21390-21395.
71. Shimakawa K., Yoshida N., Ganjoo A., Kuzukawa Y., Singh J. A model for the photostructural changes in amorphous chalcogenides. *Philosophical Magazine Letters.* 1998;*77:*153-158.
72. Bergeron A., Ibrahim J., Leonelli R., Francoeur S. Oxidation dynamics of ultrathin GaSe probed through Raman spectroscopy. *Applied Physics Letters.* 2017;*110:*241901.
73. Nobuaki K., Akira Y., Kiyoshi T., Tamotsu O., Makoto K., Koki S. Photoinduced Oxidation of Epitaxial Ga 2 Se 3 Grown by Molecular Beam Epitaxy. *Japanese Journal of Applied Physics.* 1993;*32:*L887.
74. Tanaka K., Odajima A. Photodarkening in amorphous selenium. *Solid State Communications.* 1982;*43:*961-964.

Conclusion

Summary

Selenium based amorphous chalcogenides are perspective materials for applications in the field of nonlinear optics. In the frame of this thesis, optical properties, structure and photosensitivity of co-sputtered thin films of Ge-Sb-Se and Ga-Sb-Se systems were investigated. Furthermore, optical properties and the structure of sputtered thin films of Ge-Sb-Se-Te were studied. Finally, optical properties and the structure of sputtered thin films of Ge-Sb-Se-Te were studied.

Fabricated films are of good quality as found by AM-AFM and SEM techniques. Magnetron co-sputtering technique allows a deep study of various properties throughout the composition in ternary amorphous chalcogenides [1]. It is also considered to be an efficient deposition method to fabricate amorphous thin films whose composition is out of glass-forming region of the system under study.

The studies of nonlinear optical properties of co-sputtered films by means of the nonlinear refractive index and two-photon absorption coefficient estimated by Sheik-Bahae's formalism were performed. It has been shown that the balance between refractive index and optical bandgap is the vital for the possible applications of studied materials in the field of nonlinear optics at the telecommunication wavelengths. Moreover, it was found that the minimum optical bandgap for Ge-Sb-Se and Ga-Sb-Se co-sputtered films should be at least ~1.60 eV. This value of optical bandgap (E_g^{CL} determined by Cody-Lorenz oscillator model) corresponds to the linear refractive index value of about 2.80 for both systems. Moreover, at the lower values of optical bandgap, two-photon absorption takes part, limiting such materials for the applications at 1.55 μm. The maximum nonlinearity by means of n_2 at 1.55 μm with respect to 2PA is about ~1.13-1.34 × 10^{-17} m^2W^{-1} for Ge-Sb-Se and Ga-Sb-Se co-sputtered films. High values of 2PA coefficient β indicates that strong two-photon absorption may be expected in the system of Ge-Sb-Se-Te. The alteration of selenium by tellurium in such system causes high decrease in optical bandgap.

Recently, the beam self-trapping technique was used to measure the nonlinear optical properties of Ge-Sb-Se planar waveguides. The experimental results were discussed in several papers [2-5]. Throughout these, the most important findings include low-loss propagation of spatial soliton [2] and plasmon-soliton coupling [5] in chalcogenide waveguides. These observations make these materials suitable for nonlinear photonic devices such as wavelength conversion and supercontinuum generation.

Photosensitivity of chalcogenide glasses and thin films may be the limitation of these materials in mentioned applications. From the photosensitivity studies of co-sputtered films of Ge-Sb-Se and Ga-Sb-Se under the prolonged near-bandgap irradiation one can conclude that the chemical composition of the thin films plays the significant role in the changes of optical properties. In germanium and gallium-rich films irreversible photobleaching effect (PB) was observed. The magnitude of PB decreases with an increasing antimony content in these films. Furthermore, in selenium-rich co-sputtered films of Ge-Sb-Se an inverse effect (*i.e.* photodarkening)
takes part.

The fabrication and characterization of sputtered Ge-Sb-Se-Te thin films in this work is considered to give a decent background for potential study of co-sputtered films within this system.

References

1. Halenkovič T., Gutwirth J., Němec P., Baudet E., Specht M., Gueguen Y., Sangleboeuf J.-C., Nazabal V. Amorphous Ge-Sb-Se thin films fabricated by co-sputtering: Properties and photosensitivity. *Journal of the American Ceramic Society.* 2018;*101:*2877-2887.
2. Kuriakose T., Baudet E., Halenkovič T., Elsawy M.M.R., Němec P., Nazabal V., Renversez G., Chauvet M. Measurement of ultrafast optical Kerr effect of Ge–Sb–Se chalcogenide slab waveguides by the beam self-trapping technique. *Optics Communications.* 2017;*403:*352-357.
3. Kuriakose T., Halenkovic T., Elsawy M.M.R., Nemec P., Nazabal V., Renversez G., Chauvet M. Experimental demonstration of soliton-plasmon coupling in planar waveguides (Conference Presentation). *SPIE Photonics Europe*: 2018. April 22-26, 2018, Strasbourg, France, Technical Programme, p. 122.
4. Kuriakose T., Nazabal V., Renversez G., Baudet E., Němec P., Boidin R., Chauvet M. Beam self-action in planar chalcogenide waveguides. *SPIE Photonics Europe*: 2016. April 4-7, 2016, Brussels, Belgium, Proc. SPIE 9894, Nonlinear optics and its Applications IV
5. Kuriakose T., Renversez G., Nazabal V., Elsawy M., Halenkovic T., Nemec P., Chauvet M. Experimental demonstration of plasmon-soliton coupling. *ArXiv e-prints*, 2018 (unpublished).